Optical studies of polar stratospheric clouds and related phenomena

Carl-Fredrik Enell

IRF Scientific Report 278

Optical studies of polar stratospheric clouds and related phenomena

Carl-Fredrik Enell

Cover: Polar stratospheric clouds seen from the Swedish Institute of Space Physics, January 16, 1997
Photo ©Carl-Fredrik Enell 1997
All figures and photos by the author unless otherwise stated.

Thesis for the degree of Filosofie doktor, Swedish Institute of Space Physics, 2002

Optical studies of polar stratospheric clouds and related phenomena
Typeset by the author in LaTeX

IRF Scientific Report 278
ISBN 91-7305-307-4
ISSN 0284-1703

Printed at the Swedish Institute of Space Physics
P.O. Box 812
SE-981 28 Kiruna, Sweden
September 2002

Abstract

This thesis for the degree of Doctor of Philosophy deals with methods for ground-based remote sensing of polar stratospheric clouds (PSCs), as well as trace gas measurements and the possible impact of polar stratospheric clouds on those.

Detection of polar stratospheric clouds by their impact on twilight-sky light scattering—a redshift of the spectral radiance—is examined. A number of threshold conditions for automatic PSC detection have been considered and a peak of the zenith-sky redshift at a solar zenith angle close to 94° was found to be a suitable indicator of enhanced scattering at PSC altitudes. This peak is easy to filter out numerically. However, the occurrence of PSCs estimated by this method is found to be lower than that expected based on synoptic stratospheric temperatures. Redshift peak values which suggest PSC incidence are only obtained at synoptic stratospheric temperatures well below the condensation temperature of nitric acid trihydrate, whereas PSCs are known to exist even at higher synoptic temperatures due to local cooling. A plausible explanation for this underestimation is that tropospheric clouds close to the tangent point of incident solar light screen out the light rays illuminating the PSCs, obscuring observations of enhanced scattering.

Data from imaging optical instruments have also been considered and methods for image processing have been developed. An algorithm for particle size retrieval is suggested and tested for a model case where monochromatic imaging at 4 wavelengths is assumed. Furthermore, a case study for a day with wave-generated PSCs demonstrates that semi-automatic altitude determination is possible and that triangulation remains a useful method to track PSC dynamics, showing wave motions and scale sizes too small to be resolved in many models of the phenomena (20 km or less on the day of observation).

Finally, measurements of bromine monoxide column densities with a network of UV/visible spectrometers are presented. The observations generally agree well with modelled values. Exceptions occur e.g. during Arctic spring. The difficulty of parameterising the impact of stratospheric clouds, both on stratospheric chemistry and on spectroscopic remote sensing, can be part of the explanation for this.

Sammanfattning

Denna avhandling för filosofie doktorsgraden behandlar markbaserad fjärranalys av stratosfäriska moln och berör även spektroskopiska spårgasmätningar.

En stor del av arbetet rör fotometrisk detektion av stratosfärsmoln genom dessas påverkan på ljusspridningen i zenit (rödförskjutning av den spektrala radiansen) under soluppgång och solnedgång. Olika metoder för automatisk detektering av stratosfärsmoln har provats och det visar sig att identifiering av ett maximum i rödförskjutningen kring en solzenitvinkel omkring 94° är det lämpligaste av de testade villkoren. Dock visar det sig att dessa metoder underskattar förekomsten av stratosfärsmoln eftersom signifikanta värden bara erhålls för synoptiska stratosfärstemperaturer under kondensationstemperaturen för salpetersyretrinitrat, medan stratosfärsmoln har påvisats även vid högre synoptiska temperaturer som resultat av lokal avkylning. En trolig bidragande orsak är att troposfärsmoln nära tangentpunkterna för infallande solljus påverkar resultaten genom sin avskärmande effekt.

Även avbildande instrument har använts i studierna och metoder för bildbehandling har utvecklats. En enkel algoritm för bestämning av partikelstorlekar genom monokromatisk avbildning i 4 skilda våglängder har undersökts och fungerar i ett idealt modellfall. Dessutom visar en fallstudie av våggenererade stratosfärsmoln att automatisk höjdbestämning är möjlig och att triangulering fortfarande är en intressant metod för att studera PSC-dynamik. Det visar sig i en fallstudie att vågrörelser och skalstorlekar (20 km eller mindre) som de flesta av dagens atmosfärsmodeller inte klarar av att upplösa förekommer.

Slutligen presenteras mätningar av bromoxid utförda med ett nät av spektrometrar. Resultaten är huvudsakligen i god överensstämmelse med simuleringar. Skillnader finns dock, särskilt vid de arktiska stationerna under våren. Svårigheten att uppskatta stratosfärsmolnens inverkan såväl på de kemiska reaktionerna som på de spektroskopiska mätningarna kan vara en bidragande orsak.

Contents

List of Figures

Till farfar, teletekniker Karl-Eric Enell, som när jag var ungefär 4 år gammal gav mig ett bräde med batteri, strömbrytare, lampor och ringklockor— och alltjämt är intresserad av mitt jobb trots mina svårigheter att förklara vad det går ut på.

Chapter 1

Introduction

> Die Perlmutterwolken sind auch eine ganz anders auffallende und großartige Erscheinung, und jeder der diese seltenen Wolken einmal gesehen hat, wird sie immer von gewöhnlichen irisierenden Wolken unterscheiden.
>
> Carl Störmer
>
> (The mother-of-pearl clouds are also of a wholly different outstanding and magnificent appearance, and everybody who has once seen these rare clouds will always be able to distinguish them from ordinary iridescent clouds. *Author's translation.*)

The atmosphere is mainly composed of gases. However, solid or liquid substances are also important when it comes to chemistry or balance of radiation in the atmosphere. Small solid particles or liquid droplets suspended in gases are called *aerosols*. Dust, smoke and fog are common examples.

Even in the stratosphere (see chapter 2.2), there is always a background layer of aerosols present, the so-called Junge layer [Junge and Manson, 1961, Junge et al., 1961]. This layer is made up primarily of sulfur compounds, whose main sources are the oxidation of sulfur dioxide (SO_2) and carbonyl sulfide (OCS) originating in the lower atmosphere. Sulfur dioxide can also be injected directly into the stratosphere by volcanic eruptions, leading to a rapid buildup of H_2SO_4 aerosol. Examples of optical phenomena caused by such aerosol enhancements after volcanic eruptions are shown e.g. in Meinel and Meinel [1983]. It is also likely that heavy forest fires can produce stratospheric aerosols; see e.g. Siebert et al. [2000].

Polar stratospheric clouds (PSCs), on the other hand, are regions of enhanced liquid or solid aerosol concentration, forming at altitudes typically between 15 and 30 km during the Arctic and Antarctic winters due to the low stratospheric temperatures which can be reached during polar night [Hesstvedt, 1960, Toon et al., 1986, Tolbert, 1996]. PSCs have been known at least since the 19th century. Mohn [1893] tried to estimate their altitude by visual observations during twilight, but arrived at uncertain results ranging from 23 km (analysing results of other observers) to above 100 km in his own observations. Störmer [1930] was among the first to make accurate measurements of PSC altitudes, using stereo-photographic triangulation. He could establish the fact that PSCs are located in the stratosphere.

Under certain conditions PSCs may show characteristic iridescent colours (see figure 1.1, cover and appendix A); for these instances of PSCs the terms *mother-of-pearl clouds* or *nacreous clouds* are often used. PSCs are still sunlit after sunset (when tropospheric clouds fall into darkness), a further reason for their conspicuous appearance which continues to attract the interest of scientists and laymen. In appendix A a few series of photographs of PSCs are shown, in which the common wave-like structures as well as the diverse appearances shown by different PSCs under different illumination are visible.

PSCs attracted renewed scientific interest when reactions on PSC aerosols were identified as a major reason for the release of active chlorine from man-made chlorine species leading to the Antarctic

Figure 1.1: Mother-of-pearl clouds southwest of the Swedish Institute of Space Physics in Kiruna (68°N, 20°E) in the afternoon of January 16, 1997 as the last rays of sunlight reach the stratosphere (around 14 UTC).

ozone depletion [Crutzen and Arnold, 1986]. A large number of schemes for PSC formation have been proposed—see e.g. the review by Peter [1997]. The prerequisites for formation of stratospheric clouds are primarily the presence of water, H_2SO_4 and HNO_3, and sufficiently low temperatures. Energy considerations imply that the most critical parameter is the temperature [Hanson and Mauersberger, 1988].The temperature thresholds for PSC formation can be reached either on a *synoptic* scale (literally "simultaneously visible", i.e. the scale of an entire weather map / meteorological analysis) in a stable *polar vortex* (2.4) with little wave activity, as is the case in the Antarctic, or locally. In the Arctic, synoptic PSC presence is less frequent. This is due to the Arctic polar vortex being more unstable as a result of the orography of the Northern hemisphere with its many large mountain ranges (like the Himalayas, Alps and Rocky Mountains) and unevenly distributed land masses. In Kiruna, at the eastern side of the Scandinavian mountain range, which is generally the leeside due to the prevailing westerly winds, PSC presence is locally enhanced as a consequence of the cooling induced by expansion of air masses at the crests of mountain-induced waves [Dörnbrack et al., 2000]. Mother-of-pearl clouds with a distinct wave-like appearance are often observed, as the included photographs show.

The aim of this thesis is a better understanding of the detectability of PSCs in the contexts of optical measurements and climatological observations. The included papers all deal with results from two types of ground-based optical instruments, spectrometers and cameras. Three topics are covered, namely, automatic detection of PSCs with photometric methods, three-dimensional imaging of PSCs to improve the understanding of their dynamic microphysical development, and trace gas measurements and their relation with PSCs.

This introductory part of the thesis contains a summary (chapters 2)– 4) of the fundamental physical and chemical concepts which constitute the explicit or implicit assumptions in the included papers. Chapter 5 gives a detailed technical background of the analyses and finally chapter 6 summarises the results and presents some suggestions for the future.

Chapter 2

Basic physical and chemical concepts

> The wind goeth toward the south, and turneth about unto the north; it whirleth about continually, and the wind returneth again according to his circuits.
> Eccl. 1:6

2.1 Chemistry

The atmosphere consists mainly of molecular nitrogen (N_2, $\approx 78\%$) and oxygen (O_2, $\approx 21\%$). However, there are many minor constituents which, although making up less than 1% of the atmospheric volume, are of fundamental importance for the energy balance of the atmosphere. These are called *trace gases*. Well-known examples are water (vapour and clouds account for much of the atmospheric thermal balance), carbon dioxide (the enhanced greenhouse effect), and ozone (the main absorber in certain UV bands).

2.1.1 Reactions on aerosols

The discovery of Antarctic stratospheric ozone depletion showed the importance of understanding trace-gas reactions on PSC particle surfaces [Farman et al., 1985, Crutzen and Arnold, 1986, Solomon et al., 1986, McElroy et al., 1986]. In this context it is important to consider the difference between atmospheric chemical reactions in pure gas phase, *homogeneous reactions*, and reactions taking place on phase boundaries, *heterogeneous reactions*. In gas phase the interacting molecules or atoms are required to collide with a kinetic energy above the activation energy of the reaction. Due to the relatively low temperature and pressure of the stratosphere, the ozone-depleting reactions are slow in the homogeneous case. Bound to the surfaces of aerosols, on the other hand, molecules will react more readily. Heterogeneous reactions on PSCs may be orders of magnitude faster than their homogeneous analogues. Schematically, two chains of reactions are enhanced by the presence of PSCs, namely chlorine activation

$$\mathrm{Cl}_y \xrightarrow{aerosol} \mathrm{ClO}_x$$

i.e. conversion of long-lived reservoir species (Cl_y) into reactive chlorine radicals, ClO_x,

denoxification, i.e. removal of the reactive nitrogen compounds (NO_x) which would otherwise convert active chlorine into stable reservoir species

$$\mathrm{NO}_x \xrightarrow{aerosol} \mathrm{HNO}_3$$

and subsequently, denitrification (irreversible removal of nitrogen by sedimentation of HNO_3 aerosols). Denitrification by PSC sedimentation is a major reason for chemical ozone depletion in the polar regions. The review by Solomon [1999] gives a comprehensive review of the chemistry involved in ozone destruction.

The surface area, composition and phase of PSC particles thus highly affect their ozone-depleting potential. There is therefore still a need to understand more about the properties, formation and climatology of PSCs.

2.1.2 Aerosol microphysics

The growth of aerosol particles is governed by the laws of thermodynamics. Since small droplets have a large surface tension, they will not grow spontaneously so condensation nuclei must be present. The background aerosol can provide such nuclei. Once nucleation has occurred, the droplets can grow. Many mechanisms have been suggested in order to explain how this occurs in PSCs. This is the main topic of microphysical modelling and laboratory studies of aerosols. [Hesstvedt, 1962, Crutzen and Arnold, 1986, Hanson and Mauersberger, 1988, Tabazadeh et al., 1997, Carslaw et al., 1997, Tolbert, 1996, and references in these] all deal with theoretical considerations, simulations and/or controlled experiments of the growth of PSC particles under the assumption of thermodynamic equilibrium. Mechanisms such as homogeneous and heterogeneous nucleation, solid coating, melting upon cooling and many others have been discussed. The models of aerosol formation must be able to explain the differences between the observed classes of PSCs (see chapter 4.1). The classes of PSC are defined from their optical characteristics, so there is a need to understand the optical properties of a given PSC.

2.2 Basics of atmospheric dynamics

The description of the atmosphere requires a few important fundamental concepts which can be derived from the basic principles of conservation laws. The basis for the physical description of the atmosphere is naturally formed by the laws of conservation of matter, energy and momentum. In the middle atmosphere, i.e. the troposphere, stratosphere and mesosphere (for definitions of these regions, see section 2.3 below), we can further simplify the calculations by the assumption that every infinitesimal air parcel is in dynamic and thermal equilibrium with its environment. This applies because the mean free path between air molecules is short so that every air parcel can be fully described by statistical mechanics. Thus the ideal gas law

$$p = \frac{N}{V} kT$$

applies, where p is the pressure, N the number of molecules, V the volume and k Boltzmann's constant.

The macroscopic thermodynamic quantities (pressure and temperature) are well-defined under the above requirements. We can therefore treat the middle atmosphere as a continuum of infinitesimal air parcels subject to the forces of gravity, pressure gradient and Coriolis acceleration. The energy balance also includes phase transitions within the air parcels, such as condensation and evaporation of water. These processes imply a release or uptake of latent energy.

The principles of conservation of matter, momentum and energy in all forms mentioned above can be formulated into the governing equations of atmospheric dynamics. The most common formulations of these are the continuity equation, the Navier-Stokes equations of fluid flow, and, in the common case of horizontal motions of air parcels being much faster than their vertical displacement, the equation of hydrostatic equilibrium, equivalent to the Maxwell-Boltzmann distribution of kinetic energy.

In the studies of fluid dynamics it is convenient to use two classes of coordinate systems, namely the *Eulerian* and *Lagrangian* representations. In the case of the atmosphere the former means Earth-fixed coordinates whereas the latter is the centre-of-gravity frame of a given air parcel. For studies of

stratospheric clouds the large-scale temperature and pressure fields are conveniently given in Eulerian coordinates whereas the description of the microphysical development of PSC particles belongs in the Lagrangian frame of reference.

Furthermore, the radiation balance must be considered. The general problem involves integration of differential energy fluxes over all directions at each point of the atmosphere and at all wavelengths. This is expressed in the radiative transfer equation (RTE). Many numerical approaches are available for different classes of problems. In this work we will only consider single and multiple scattering of sunlight at visible wavelengths.

2.3 Stability and atmospheric regions

A small perturbation in the vertical position of an air parcel will either be amplified if its consequent change of temperature (and therefore its density) is larger than the temperature gradient of its surroundings, or damped if its temperature change is smaller. The end temperature of the parcel is given by its original temperature and the change due to (quasi-)adiabatic expansion/compression during vertical motion. Therefore the static stability of the atmosphere depends on the gradient of *potential temperature*, where the potential temperature θ is invariant under adiabatic motions of an air parcel. It is defined as the temperature an air parcel would have if adiabatically compressed to the mean sea-level pressure, i.e.

$$\theta = T \left(\frac{p}{p_0} \right)^{-\kappa}$$

where T is the temperature, p the pressure and p_0 the standard pressure at sea level (1.0×10^5 Pa). κ is related to the number of kinetic degrees of freedom of the gas molecules through $\kappa = 1 - \frac{c_\mathrm{v}}{c_\mathrm{p}}$ and equals $\frac{2}{7}$ for ideal diatomic gases. c_v and c_p are the heat capacities at constant volume and constant pressure, respectively.

The potential temperature gradient is largely determined by the radiative balance. This is the cause for the layering of the atmosphere in regions of highly different stability. The *troposphere* is a convective zone with a potential temperature gradient less than or equal to the *adiabatic lapse rate*, the temperature gradient that would result from adiabatic convection and possibly latent heat release from water condensation alone. In the *stratosphere*, where solar radiation is absorbed by ozone and other trace gases, the potential temperature gradient is positive. The stratosphere is therefore stably stratified, which gives it its name. In fact, the potential temperature is a convenient altitude coordinate for use in studies of stratospheric dynamics, since many processes are nearly adiabatic. Since adiabatic processes are defined by the heat transfer dQ being equal to zero, there is no change in entropy $S = \int \frac{dQ}{T}$ and potential temperature levels are *isentropes*. The *mesosphere* is a region of wave-driven convection. This wave activity is strongest in the summer hemisphere,causing the summer polar mesopause to be the coldest region of the entire atmosphere. The latter fact is the reason for the presence of *noctilucent clouds*, a subject beyond the scope of this thesis.

Figure 2.1 shows typical profiles of potential temperature during summer and winter, calculated from radiosondes launched at Esrange. There is a well-defined *tropopause* at 10 km during summer, a feature which is often absent during polar night due to its primarily radiation-driven characteristics.

2.4 The global-scale circulation

The presence of stratospheric clouds can be circumpolar or local, and observations of them are often performed locally. However, the background for the dynamics of the polar atmosphere is set by the global-scale atmospheric circulation. A simple picture of the atmosphere is that of a heat-machine,

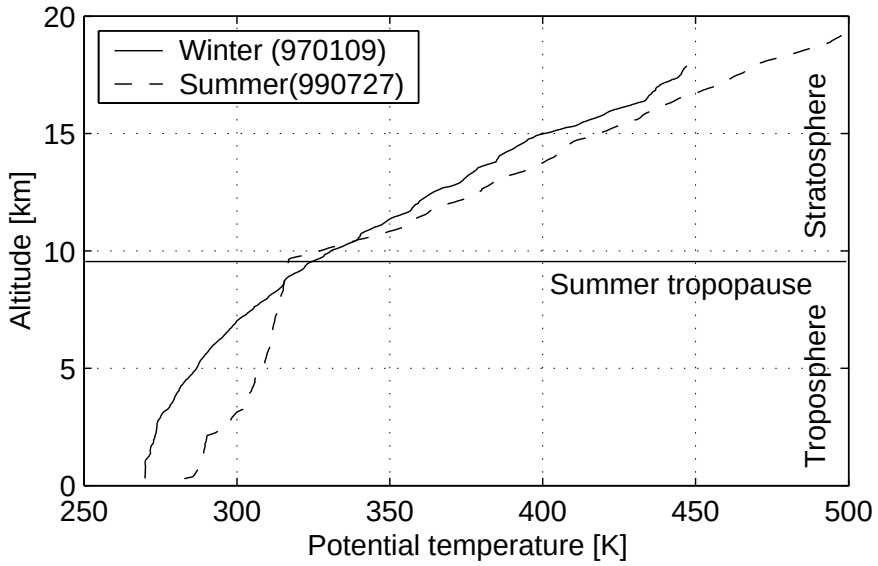

Figure 2.1: The principal structure of the troposphere and stratosphere, as determined by the temperature profile.

driven by the gradient of increasing solar irradiance from the pole towards the equator. The real picture is more complicated since the Earth is rotating. The Coriolis force gives rise to a subdivision of each hemisphere (figure 2.2). Forcing by waves at different scales is also important, as discussed in section 2.5.

The most important consequence of the Coriolis force in the polar regions is the presence of the *polar vortices*. These are characterised by a westerly (=eastward) air circulation around the winter pole throughout the middle atmosphere. The absence of radiative heating during polar winter gives rise to a circulating and sinking motion (subsidence) and a net cooling of the polar air. The vortex air thus moves on sinking isentropes during a stable winter. This is especially true for the stable southern hemisphere, where the largest ozone depletion is consequently observed due to the resulting synoptic-scale PSC presence. The vortex strength, conserved in an inertial frame of reference, is given by the absolute vorticity

$$\eta = (\nabla \times \vec{v}) \cdot \hat{z} + f$$

i.e. the vertical component of the rotation of $\vec{v}$, the wind velocity vector, plus the Coriolis parameter f. (The latter ensures that the rotation with respect to the Earth's axis is conserved on latitudinal translations). However, the absolute vorticity of an air mass will change under e.g. compression and stretching. To compare air masses the adiabatically invariant *potential vorticity*

$$\mathrm{PV} = \eta \frac{-g}{\frac{\partial p}{\partial \theta}}$$

is a far more used measure. The factor $-g \Big/ \dfrac{\partial p}{\partial \theta}$ can be thought of as the distance between isentropes[1], compensating for absolute vorticity changes on adiabatic stretching and compression.

Figure 2.3 shows calculated potential vorticity fields on the 550 K level (approximately 23 km) for two days during Arctic and Antarctic spring, respectively. The Antarctic vortex is often stable and

[1]Multiplied with density in standard units its dimension becomes [K/m]

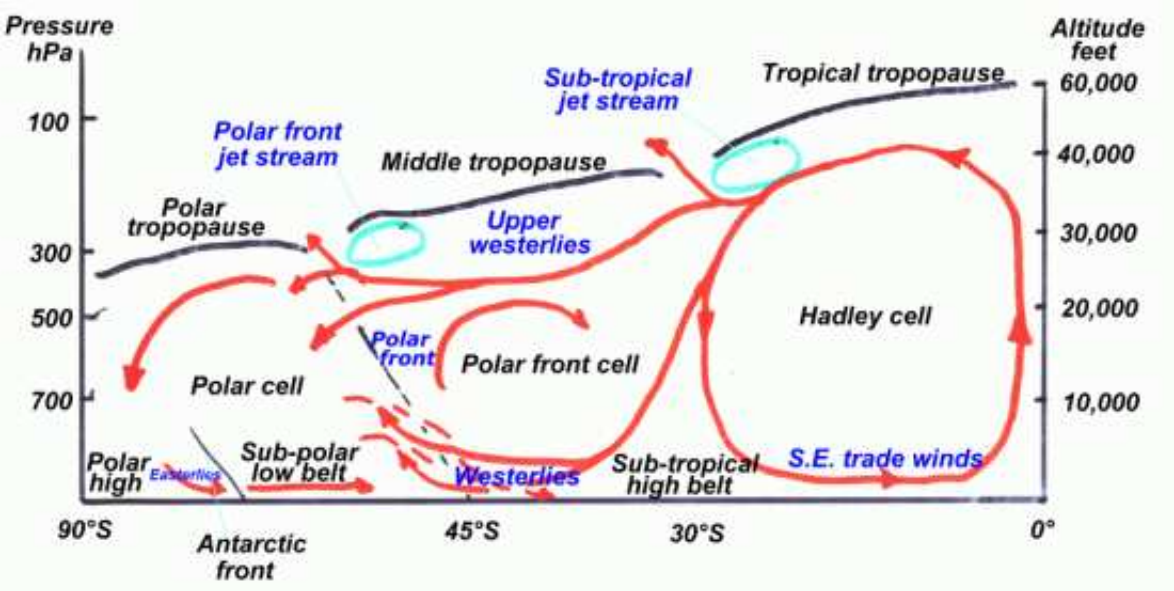

Figure 2.2: The general tropospheric circulation, cross section from pole to equator. Figure from `http://www.auf.asn.au/meteorology`, © John Brandon 2000.

nearly circular, which allows strong cooling on a synoptic scale. The Arctic vortex, however, is often distorted due to waves forced by the more complex orography (the many high mountain ranges and the uneven distribution of continents and oceans) of the northern hemisphere.

2.5 Atmospheric waves

The circulation of the middle and upper atmosphere cannot be driven by pressure/temperature gradients alone—this is not sufficient to explain the observed circulation. Energy and momentum transfer by waves turns out to be important, which is reflected by the fact that the governing equations of atmospheric motion allow wave solutions. See Salby [1996] or Holton [1992] for more comprehensive discussions of atmospheric waves. In accordance with the different asymptotic regimes of the governing equations, many corresponding classes of waves can be obtained. These correspond to different scales in nature and can be thought of as resulting from neglecting the forces irrelevant on the scale in question. Of importance for PSC presence are the *gravity waves*, which occur where gravity (and thus also the pressure gradient) provides the principal restoring force of transverse displacements of air parcels, and the global-scale *Rossby waves* (or *planetary waves*). In the latter class of waves the Coriolis force is the principal restoring force.

These waves are schematically described in figure 2.4. Note that gravity/buoyancy and vorticity, respectively, give rise to the restoring forces indicated by the arrows. The rotation of the air parcels in the Rossby wave arises because angular momentum around the Earth's axis of rotation must be conserved and gives rise to cyclones (low-pressures) and anticyclones (high-pressures).

The net global effect of waves on the atmosphere is always a transfer of momentum from the ground to the atmosphere, in such a way as to exert a drag on atmospheric motion. Locally, however, the effects may be entirely different. Most important in the context of PSCs is the additional stratospheric cooling induced by the expansion of air masses in mountain-induced gravity waves.

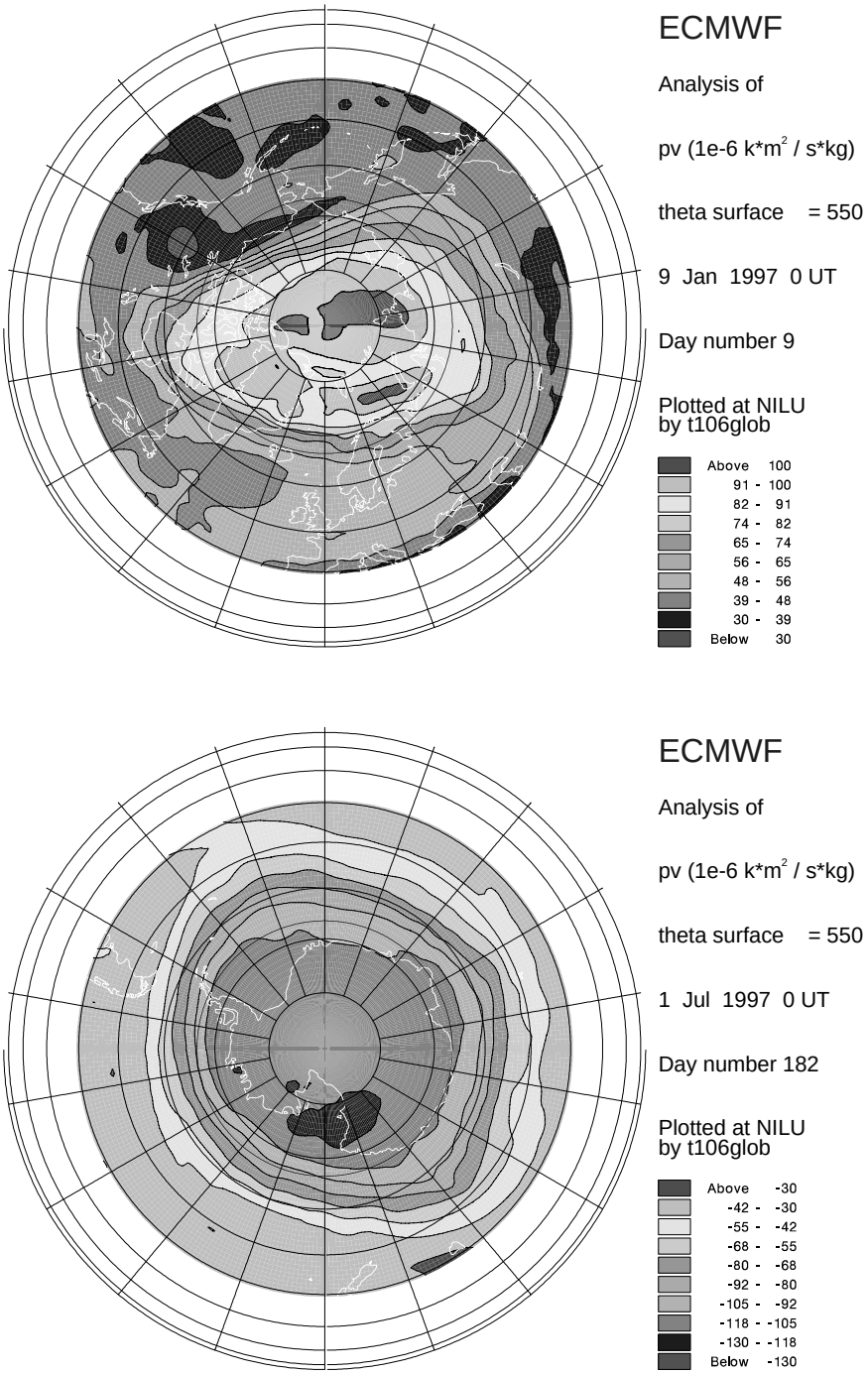

Figure 2.3: Typical Arctic and Antarctic polar vortices (Potential vorticity at the 550 K level; the westerly direction of air flow is positive in the Arctic and negative in the Antarctic). Note the stable, nearly circular shape of the Antarctic vortex, in contrast to the more distorted Arctic vortex. Plots from NILU (the Norwegian Institute of Air Research).

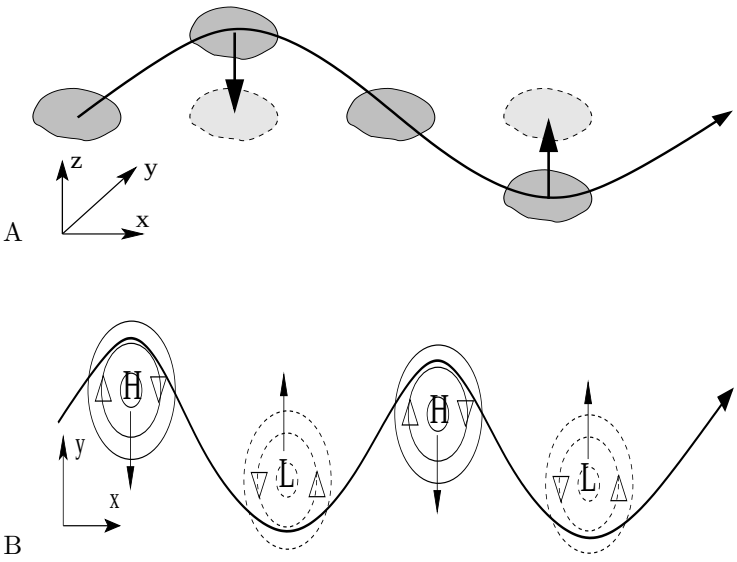

Figure 2.4: Principal sketches of two important atmospheric wave regimes. A: Gravity waves; B: Rossby waves. The restoring forces are indicated by arrows.

Chapter 3

Optical remote sensing

> For example, a manager would never say, "I used my fork to eat a potato." A manager would say, "I utilized a multitined tool to process a starch resource."
>
> Scott Adams, The Dilbert Principle

There are two principal ways of studying atmospheric phenomena, namely *remote sensing* (looking at the phenomenon from a distance) and *in-situ* measurements (at the place). The measurements used in the included papers all rely on remote sensing with optical instruments. As a background for understanding these an overview of the optical concepts involved is given here.

3.1 Data inversion

A basic characteristic of all remote and many in-situ methods is that they are *inverse*. This means that the quantity to be measured must be determined indirectly using a priori knowledge of the physical system under consideration. In many cases the process of analysis requires a forward model of the system, which is run iteratively with changed input parameters until the output matches the measurement. Figure 3.1 outlines the principle.

The variable to measure is thus one of the input parameters to the model, hence the name data inversion. The result may depend critically on the choice of model algorithms and the number and range of input parameters. A large part of the work in remote sensing therefore concerns agreements on algorithms and parameter ranges in order to make the results intercomparable.

3.2 Optical properties of the atmosphere

The measurements discussed in papers I-V all contain some aspects of radiative transfer in the visible wavelength range. We here consider the properties of the sunlit atmosphere, although absorption of moon- and starlight are of importance for spectroscopic measurements of atmospheric trace gas columns. The definitions in the following subsections follow those used in the papers. Most of the original references mentioned below can be found in Bohren [1989].

3.2.1 Scattering

Scattering is a phenomenon arising from the superposition of the waves diffracted by an object with the incident waves. Scattering occurs at obstacles of all sizes but is most evident when their sizes are comparable to the wavelength or smaller. Quantum-mechanically, it applies to all particle interactions; here we consider scattering of photons by electrons. For objects larger than the wavelength, it is often

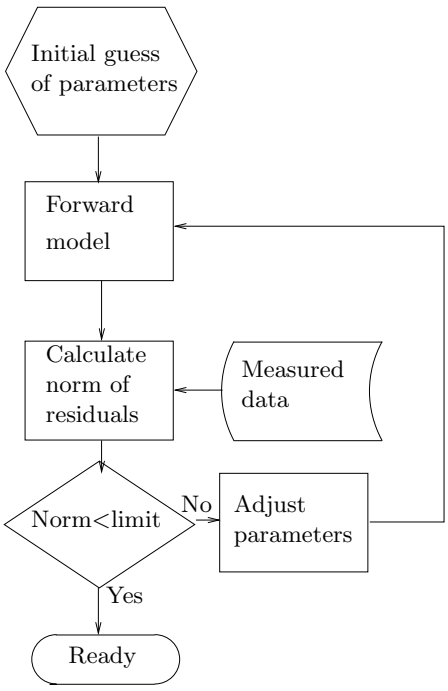

Figure 3.1: The iterative process of data inversion

possible to use the paraxial approximation, that is, to consider refraction of light rays through the object. This may be useful in studies of tropospheric clouds and rain, but will not be considered here. In the other limit, scattering objects being much smaller than the wavelength, the familiar so-called *Rayleigh* scattering [see Young, 1980, for a discussion on the confusion that exists around this concept] is obtained.

Rayleigh's solution considers the superposition of the incident plane waves with pure dipole radiation emitted by the scatterers. This results in a scattered intensity varying with wavelength λ as λ^{-4}, and the light scattered perpendicularly to the direction of incidence being fully plane-polarised. These effects are of major importance for the daytime sky, considering only scattering by air molecules, and can be observed by anybody taking photographs with a polarising filter in front of the lens. This also implies that any instruments used for quantitative spectroscopy of scattered sunlight should preferably be designed so as to either eliminate polarisation sensitivity or to make use of polarimetry.

The solution to the scattering problem most frequently applied in practice, however, is the one according to *Gustav Mie*. This solution applies to spherical objects of all sizes and the main part of the solution is a spherical expansion of the incident plane waves. Many computer codes implementing Mie's solution are available. Those are often used for estimating extinction and backscatter by atmospheric aerosols. The code by Bohren and Huffman [1983] has been applied in Papers III and IV of this thesis to estimate scattering *phase functions* of PSC particles. The term phase function here means the relative scattered radiance as a function of scattering angle disregarding polarisation, i.e.

$$P^2(\theta) = \frac{L_{\parallel}^2(\theta) + L_{\perp}^2(\theta)}{L_{\mathrm{inc}}}$$

where P is the phase function, L_{inc} the incident radiance, and $(L_{\parallel}, L_{\perp})$ the scattered radiances referring to the planes of polarisation parallel and perpendicular to the plane of scattering, defined as the plane

containing the directions of incident and scattered light.

Scattering processes may be *elastic* (energy-conserving) or *inelastic*, where some of the electromagnetic energy is converted from or into molecular rotational, vibrational or translational energy so that the scattered light is wavelength-shifted. The concepts of rotational and vibrational *Raman scattering* are especially important. Calculation of Raman scattering is often included in the retrieval of trace gas columns by UV/visible absorption spectroscopy in order to correct for the so-called *Ring effect* [Chance and Spurr, 1997]. Raman scattering is also utilised in lidar measurements, e.g. for tropospheric H_2O measurements or for detecting pure molecular backscatter to separate the latter from aerosol backscatter.

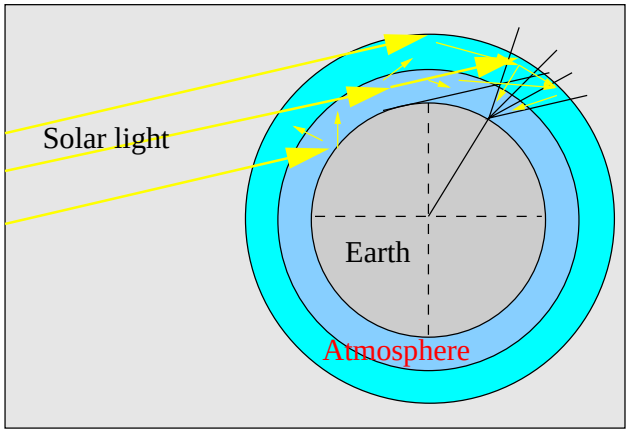

Figure 3.2: Scattering of sunlight in the atmosphere: A simple sketch of the principles. Single and multiple scattering are outlined with large and small arrows, respectively.

Figure 3.2 shows a simplified sketch of scattered sunlight observed from the ground (here during night at high latitudes). See also Stammes et al. [1989]. The arrows outline two limiting cases: single and multiple scattering.

The simplest case to treat mathematically is single scattering. Many computer models exist, such as the one by Frank [1991]. During twilight, however, the single-scattering approximation is not applicable. Multiple scattering must be taken into the account. The ratio of single-scattered to multiply scattered light has been estimated by polarimetry by Ougolnikov and Maslov [1999].

Multiple scattering is mathematically complicated to model and for many problems time-consuming Monte Carlo calculations are the only choice. For estimates of integrated radiances, etc, where accurate resolution is not important, a large number of analytical approximations exist, such as the discrete ordinates method [Stamnes et al., 1988].

3.2.2 Extinction

The concept of *extinction* refers to all attenuation of radiation, both by absorption and by scattering out of the path. It is in general necessary to take both effects into consideration. The amount of extinction in terms of the incident irradiance I_0 (see Appendix C) can be summarised in the *optical depth* τ, defined according to the law of exponential attenuation as

$$I = I_0 \exp(-\tau)$$

i.e. $\tau = \ln(I_0/I)$.

3.3 Absorption

Very important is also the variable extinction due to molecular absorption. Hulburt [1953] considered absorption by ozone during twilight, when singly scattered zenith light has traversed the stratosphere. Absorption spectroscopy is used for trace-gas measurements in the infrared, UV and visible ranges with satellite-borne, balloon-borne and ground-based instruments. Spectra of solar, lunar or stellar lights traversing the atmosphere in different geometries are all utilised. In this work we will focus on UV/visible zenith-sky spectroscopy.

3.3.1 The DOAS algorithm

Absorption spectroscopy relies on the fact that every molecule has its characteristic absorption bands due to electronic, rotational and vibrational transitions in the molecule. Thus, if the spectral distribution of light incident on an air volume is known, the amount of absorber can be determined from its a priori known spectral absorption cross section. However, in general the spectral distribution of incident light is unknown. The commonly used principle of DOAS *(Differential Optical Absorption Spectroscopy)* is a way to circumvent this problem [Platt, 1994]. The main idea is that absorption cross sections in the visible range can be separated into two independent components, one slowly and one rapidly varying with wavelength relative to the wavelength range covered by a spectrometer. In the DOAS algorithm, trace gas columns are retrieved by fitting only the rapidly varying component to the measured spectrum, while filtering out its broad-band behaviour.

The extra-atmospheric spectral radiance is L_0 and the observed transmitted spectral radiance is L_t, as shown in figure 3.3.

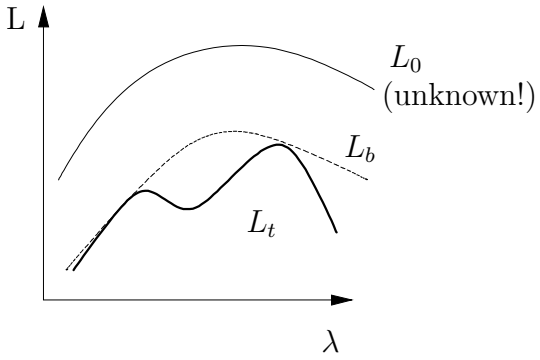

Figure 3.3: The key principle of DOAS: Separation of the observed absorption cross section into two parts, one slowly varying and one rapidly varying with respect to the wavelength interval observed.

Thus,

$$L_\mathrm{t} = \mathrm{L}_0 exp(-\tau)$$

where the optical depth τ of an absorber with column density (molecules in a column of unit cross sectional area) c is

$$\tau = c \cdot \sigma$$

(The notation $\ldots(\lambda)$ for the wavelength-dependent quantities is suppressed here.) The assumption is now that it is possible to separate the absorption cross section σ according to

$$\sigma = \sigma_\mathrm{b} + \sigma'$$

where the subscript b and the prime refer to the separable broad-band and rapid wavelength dependencies, respectively, so that

$$L_{\mathrm{t}} = L_0 \exp(-\tau) = L_0 \exp(-c\sigma_{\mathrm{b}}) \cdot \exp(-c\sigma') = L_{\mathrm{b}} \cdot \exp(-c\sigma')$$

Therefore c can be determined as

$$c = \frac{1}{\sigma'} \ln \frac{L_{\mathrm{b}}}{L_{\mathrm{t}}}$$

where L_0 no longer appears. In practice a number of differential reference spectra are logarithmically least-squares fit to the filtered measured spectrum, together with other reference spectra to correct for solar Fraunhofer lines, Ring effect[Chance and Spurr, 1997] and so on, as described in chapter 5.2.

The DOAS algorithm is in general use in both satellite-borne and ground-based applications. One advantage of applying DOAS in the ultraviolet range is the possibility to measure bromine monoxide, Br O, which is very efficient in ozone depletion although it is less abundant than chlorine species. This is the main topic of Paper V.

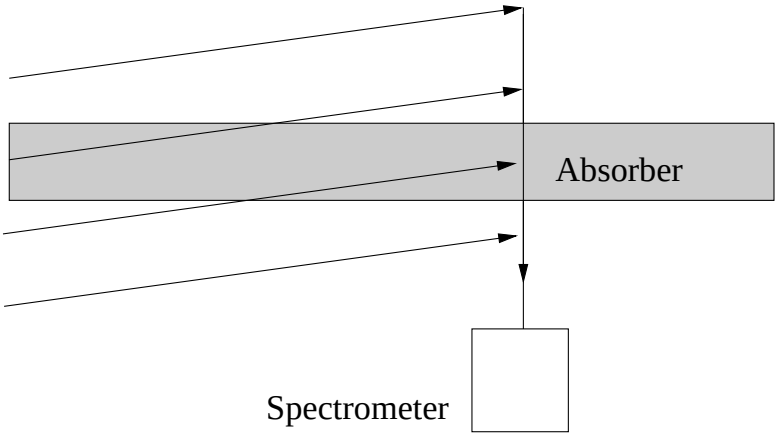

Figure 3.4: The geometry of zenith-sky spectroscopy. The absorption is an average over an ensemble of atmospheric photon paths. Reality is more complicated than this figure due to the importance of multiple scattering.

The measurements have been performed with the Heidelberg University UV/visible spectrometer in Kiruna [Wagner, 1994, Otten et al., 1998]. This is a zenith-looking instrument; thus the geometry is rather complicated. The observed absorption represents an integration over many infinitesimal photon paths as shown in figure 3.4. (Only single scattering above the instrument is shown.)

3.3.2 Spectroscopy and radiative transfer

A key issue in UV/visible zenith direction is the fact that the observed radiance represents an integral over multiple infinitesimal atmospheric light paths, both multiply scattered and single-scattered in the field of view. The resulting so-called *slant column densities* (SCDs), which are the results of a DOAS retrieval, must therefore be interpreted with the help of radiative transfer models (RTMs), which are used to calculate so-called *air mass factors* (AMFs), defined by

$$\mathrm{AMF} = \frac{\mathrm{SCD}}{\mathrm{VCD}}$$

where the *vertical column density* VCD is the physical number of gas molecules in a zenith-directed atmospheric column of unit cross section above the instrument.

The modelling of AMFs requires that the altitude profile of the absorbing gas to be measured is known—a self-contradictory situation. For gases with fairly constant profiles, however, using a standard profile does not introduce any large errors.

Most of the RTMs used so far to calculate AMFs [e.g. Frank, 1991] only take into account single scattering in the field of view of the instrument, thus reducing the problem to calculation of the absorptions along an ensemble of sun-zenith-instrument paths. This might be appropriate for interpretation of absorption measurements, but for understanding the appearance of the twilight sky (including PSCs) it is highly inaccurate.

3.4 Applicability of the single-scattering approximation

To qualitatively look at the difference between the single-scattering and multiple scattering phenomena, the atmospheric RTM MODTRAN 3 [Anderson et al., 1995] was run for scattered solar light at solar zenith angles of 85°–94°, viewed from the ground at the altitude of IRF (420 metres above sea level) in two directions, viz. the solar azimuthal direction at a zenith angle of 80°, and the zenith direction. For each case MODTRAN was run both for pure single scattering, and with the included 8-stream DISORT [Stamnes et al., 1988] estimation of multiple scattering.

Figure 3.5 shows the spectral radiances for the first case and figure 3.6 those for the second case. It is clear that it is in the blue part of the spectrum the impact of multiple scattering is largest. From pure single Rayleigh scattering one would expect a reddening of the sky as the sun sets. However, multiple scattering causes a blueshift of the spectral radiance instead, which is what is observed in practice during sunset. Hulburt [1953] explained this effect (wavelength-integrated) by ozone absorption in the single-scattering geometry. Ozone absorption is included in MODTRAN but at the chosen wavelength its impact turns out to be of little importance, the single-scattering model predicting a redshift of the sky. Measurements such as those by Ougolnikov and Maslov [1999] confirm the importance of multiple scattering after sunset.

In figure 3.7 we use the data of figures 3.5 and 3.6 to calculate the ratio of the radiances at one "red" and one "blue" wavelength, the so-called *colour index* (CI), and plot this quantity versus the solar zenith angle. The zenith colour index is a quantity used as an indicator for enhanced zenith-sky scattering by PSCs in papers I and III. The zenith-sky CI (figure 3.7 B) shows qualitatively the behaviour that is experimentally confirmed in paper III, i e a blueshift (CI decrease) after sunset. Introduction of an additional strongly single-scattering layer with low (as compared to Rayleigh scattering) wavelength-dependence at PSC altitudes will instead cause a redshift after sunset.

We also include the CI at 80° (figure 3.7 A) to confirm that the model reproduces the fact that the horizon turns deep blue after sunset, which is also to a large extent an effect of multiple scattering.

3.5 Imaging

An *image* is a two-dimensional array $I(u, v)$ of measured values of the temporally integrated irradiance over a certain area around (u, v) called a *pixel* (acronym for "picture element"). The pixels can be thought of as integrating photometers placed on the same chip and having a common lens. The image is thus a projection of integrals of radiance along lines of sight (φ, θ) to the pixel plane (u, v). See figure 3.8.

Examples of advanced imagers are the ALIS cameras (figure 3.9)—the cameras of the *Auroral Large Imaging System* [Steen and Brändström, 1993, Brändström and Steen, 1994, Brändström, 2002]. In Paper 5 two such cameras have been applied for bistatic imaging of PSCs. This camera takes images in monochromatic light by means of interference filters. These must be placed in telecentric lens systems

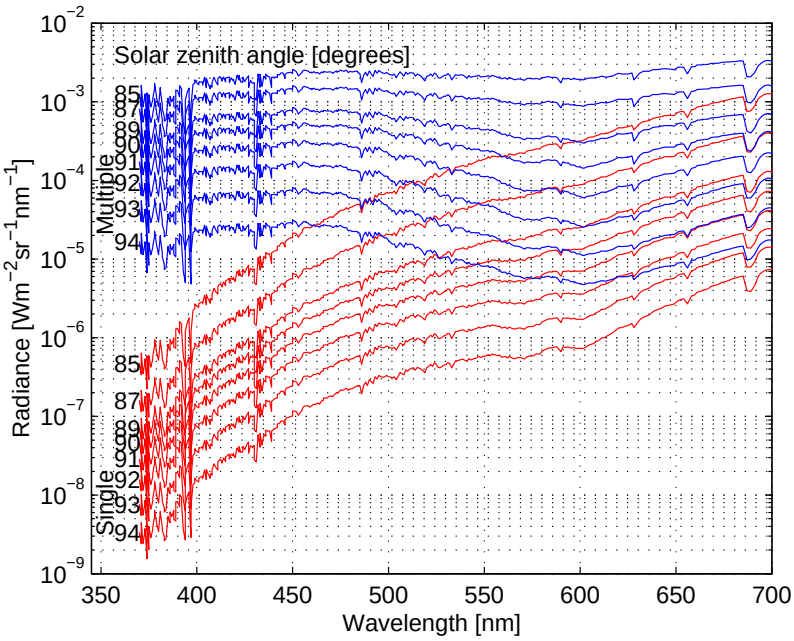

Figure 3.5: The scattered solar spectral radiance calculated with Modtran 3, viewing in the solar azimuthal direction at a zenith angle of 80°. The default subarctic winter atmosphere without clouds was used.

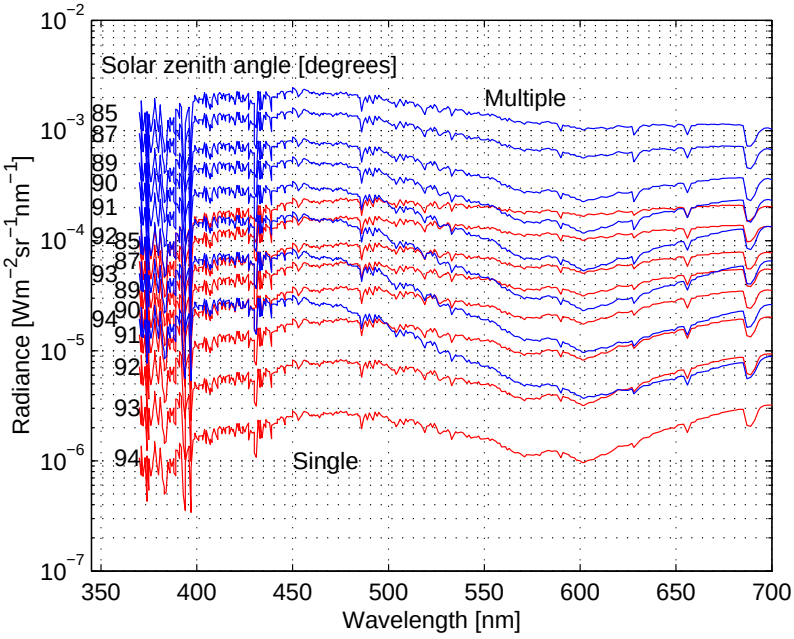

Figure 3.6: The scattered solar spectral radiance calculated with Modtran 3, viewing in the zenith direction. The default subarctic winter atmosphere without clouds was used.

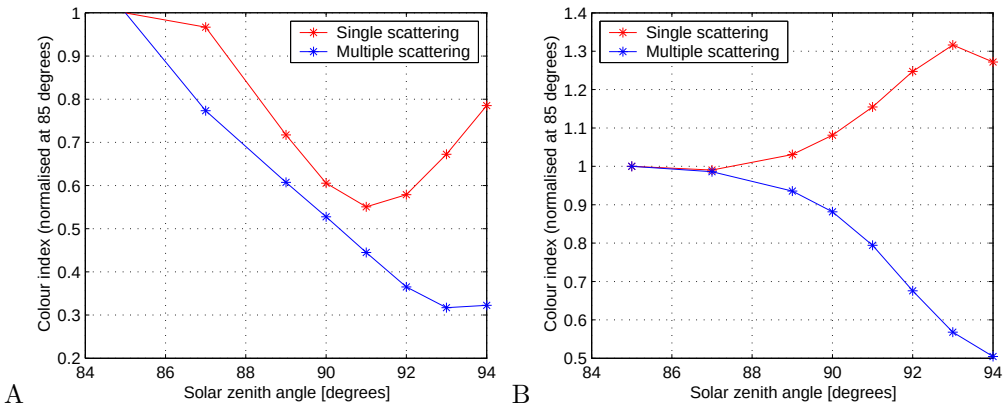

Figure 3.7: The colour indices calculated as the ratio of the radiances at 680 ± 2 nm and 385 ± 2 nm from the modelled spectral radiance of the previous figures. A: Viewing angle 80°. B: Zenith. Because of the highly different absolute values, the data have been scaled to unity at 85 degrees solar zenith angle.

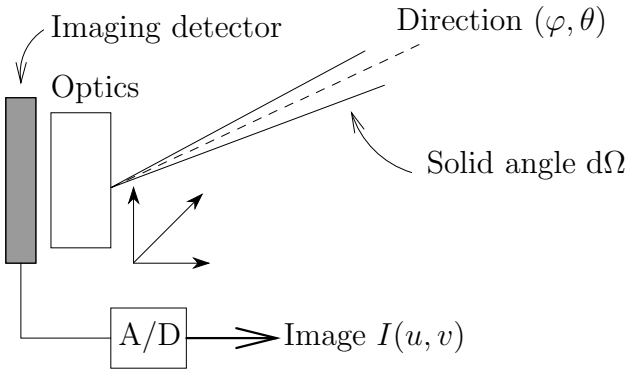

Figure 3.8: The general principle of digital imaging: $I(u, v) = f(\varphi, \theta)$. The function f includes the ideal projection, the characteristics of the optical system including the detector, and the transfer function of the electronics. (A/D=analog to digital conversion.)

(figure 3.10) since the centre wavelength of an interference filter is given by the optical path difference, which is longer for light rays entering the filter non-perpendicularly.

Most imaging detectors used today are *charge-coupled devices* (CCDs). Their principle of operation is described in Holst [1998]. CCDs are inherently linear and have low noise—thus no such corrections are applied. However, their sensitivity is wavelength-dependent and thus only relative measurements are used since absolute calibration is difficult.

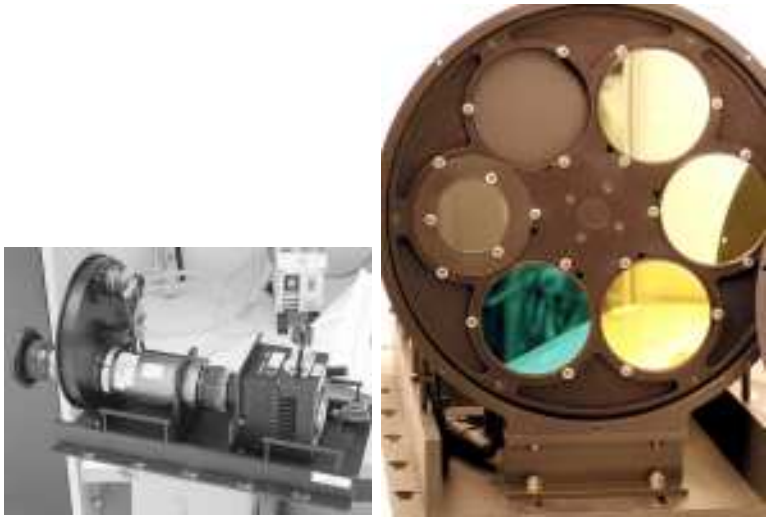

Figure 3.9: An ALIS camera. The long tube contains the telecentric lens system. This figure also shows the filter wheel dismantled. There are five filters and one open position.

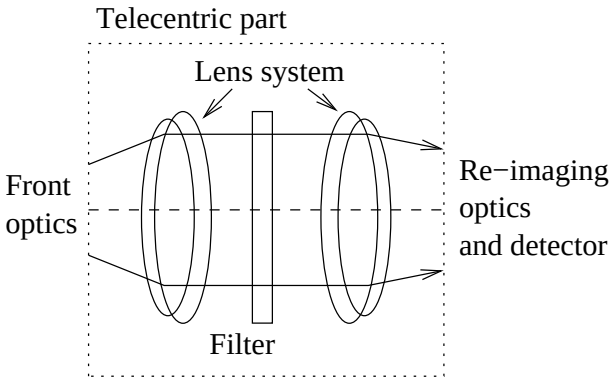

Figure 3.10: Telecentric optics: Interference filters require plane-parallel light rays since the path difference is longer for slant rays.

Chapter 4

Classification of PSCs

> Jeg vilde anse det for meget ønskeligt, om andre Meteorologer og Fysikere vilde meddele Iagttagelser og Undersøgelser, der kunde tjene til at opklare de iriserende Skyers Væsen.
>
> Henrik Mohn, Perlemorskyer, 1893
>
> (I would consider it most desirable that other meteorologists and physicists would report observations and experiments which could serve to clarify the nature of the iridescent clouds. *Author's translation.*)

A number of details in PSC formation processes are still unclear. Since PSC properties affect ozone chemistry, experimental PSC studies is still a vivid subject. The most important remote-sensing instrument is the lidar[1], which can be both ground-based and airborne. Lidar studies of PSCs [Poole et al., 1988, McCormick et al., 1990] became the basis for PSC classification. During a number of winter campaigns in the vicinity of Kiruna [Fricke et al., 1998, Reichardt et al., 1999] a lidar was used together with other remote observations by VHF wind radar, photographic imaging, and so on.

PSC incidence on a synoptic scale, i.e. enhanced stratospheric extinction, can also be mapped from satellites [McCormick et al., 1982, Cariolle et al., 1989, Meerkötter, 1995, Garcia et al., 1995].

In-situ sampling of PSC particles is mainly performed by balloon-borne instruments, although high-altitude aircraft are sometimes deployed. In-situ platforms can sample the particles directly with chemical instruments, such as mass spectrometers, take samples for laboratory analysis, or carry "locally remote sensing" instruments, e.g. *backscatter sondes* whose function resembles that of the lidar. Larsen et al. [2000] gives an instructive example of using these methods together. Balloon-borne meteorological *radiosondes* are important for obtaining background information on temperature profiles and wind speeds and thus dynamical parameters.

4.1 Classification of PSCs as observed by lidar

The quantity directly measurable by a lidar is the backscattered radiance in different polarisations. The results are commonly presented as *backscatter ratio* R and *depolarisation* δ. The backscatter ratio is defined as

$$R = \frac{I_{aerosol} + I_{Rayleigh}}{I_{Rayleigh}}$$

i.e. the ratio of the total backscatter from molecules and aerosols to that expected from molecular Rayleigh scattering only. The depolarisation δ is calculated as

$$\delta = \frac{I_{\perp}}{I_{\parallel}}$$

[1] **LI**ght **D**etection **A**nd **R**anging, the optical equivalent of a radar

where $I_{\parallel}$ is measured with an analyser aligned with the plane of polarisation of the transmitting laser whereas $I_{\perp}$ is measured in the perpendicular plane of polarisation.

Early lidar studies during PSC events [Poole et al., 1988, McCormick et al., 1990] showed that observed backscatter ratios and depolarisation fall into more or less distinct categories. Three major PSC classes were identified with respect to these findings, namely:

Ia: PSCs with low backscatter ratio and high depolarisation

Ib: PSCs with high backscatter ratio and low depolarisation

II: PSCs with high backscatter ratio and depolarisation

Further subclasses of PSCs have sometimes been suggested; these three are, however, the most commonly distinguished ones.

4.2 Classification according to occurrence and appearance

In addition to the classification due to properties, it is also common to make certain distinctions according to the presence and appearance. PSCs covering large regions, such as in the stable Antarctic polar vortex, are consequently called *synoptic* PSCs. Synoptic PSCs also occur in the Arctic but less frequently and with a large interannual variability. The fact that PSC presence in the Arctic is often related to wave cooling is reflected in the often used references to these PSCs as (lee)wave PSCs, mountain-induced PSCs, and so on, in analogy with the so-called *lenticular clouds* which can be observed in the troposphere close to mountains.

When PSC were first observed, such as the observations close to the Norwegian mountain range [Störmer, 1929, 1932] the term used to describe the clouds was *mother-of-pearl clouds*, a name still used today by the public in areas where PSCs are visible due to their colourful appearance under suitable conditions. Regarding the relation between mother-of-pearl appearance and physical conditions it has often been stated that mother-of-pearl clouds are identical with PSC II. However, today there is no consensus on this issue.

For the PSC to display the characteristic iridescent colours, the particles within a volume must be similar in size (monodisperse size distribution) and that size must be comparable to the wavelength. Observed mother-of-pearl clouds in Kiruna are often wavelike and connected with strong tropospheric wind. This issue is discussed in Paper IV. It is likely that rapid leewave-induced cooling will produce the required monodisperse size distribution. Tropospheric viewing conditions must of course be favourable, i.e. there should be no tropospheric clouds between the PSC and the observer or in the path of sunlight illuminating the PSC.

4.3 The relation to PSC microphysics

When PSCs were first being studied, it was assumed that only water was present in sufficient amounts to account for the presence of clouds in the stratosphere, and this assumption was the basis for theoretical considerations by Hesstvedt [1960, 1962]. As more knowledge about stratospheric aerosols was accumulated, it became clear that also other substances are involved, such as nitric acid [Tolbert, 1996] and sulfuric acid (see chapter 1). This is also the starting point for an explanation of the differences between PSC classes.

While it is now commonly agreed that the type Ib PSCs consist of spherical particles , i.e. liquid droplets probably composed of supercooled solutions, the nature of the depolarising PSC Ia has been more controversial. The prevailing idea is that they consist of nitric acid trihydrate (NAT) particles. PSC II form at low temperatures and must consist of large particles. They are therefore identified with ice PSCs.

Considering the thermodynamic requirements, the most important parameter governing the formation of PSCs turns out to be the temperature. The freezing temperatures of NAT and ice, T_{NAT} and T_{ice}, are customarily used as thresholds indicating the presence of PSC I and II, respectively. T_{NAT} and T_{ice} depend on the pressure and the concentrations of HNO_3 and water vapour; the values used in Paper III are given in table 4.1. Note that the altitude is given as potential temperature levels.

Level [K]	T_{NAT}[K]	T_{ice}[K]
475	194.5	188.0
550	191.6	185.0
675	187.8	181.7

Table 4.1: Freezing temperatures of NAT and ice used in Paper III.

4.4 Recent developments

Tsias et al. [1997], Voigt et al. [2000] and other authors have taken into account the possibility that *non-equilibrium* effects act to change the composition of aerosols and even may force freezing of solids (PSC Ia) above T_{NAT}. The most important possible non-equilibrium situation considered here is that of mountain wave induced temperature fluctuations.

Despite the fact that PSCs have been studied for almost one century, new surprising facts are still discovered. During the SOLVE/Theseo2000 winter campaign, another kind of in-situ platform, the NASA ER-2 high-altitude aircraft with its aerosol sampling instruments, was deployed in Kiruna. This led to the discovery of unexpectedly large NAT particles, which were nicknamed “NAT rocks” [Fahey et al., 2001]. These have a potentially very important role in stratospheric chemistry since their rapid sedimentation may cause severe denitrification by removing HNO_3.

Chapter 5

Observations

> It is the theory which decides what can be observed.
> Albert Einstein

The observations forming the basis for the included papers have all been performed with optical instruments in the vicinity of the Swedish Institute of Space Physics, located at 67.84° N, 20.41° E. Paper V also includes similar UV/visible BrO measurements throughout the northern hemisphere. This chapter complements the brief outlines of technical and computational procedures given in the papers.

5.1 Supporting models

To support the interpretations of the results obtained the atmospheric model MODTRAN has been run, as shown in chapter 3.

The measurements in paper V were supported by chemistry/transport modelling with the SLIMCAT model, developed and described by Chipperfield [1999]. For the comparison with the measured columns, the modelled BrO profiles were fed into the radiative transfer model described by [Solomon et al., 1987] to calculate differential slant column densities (see below) as measured with the zenith-sky spectrometers. This model retains the spherical geometry of the atmosphere which is crucial here, in contrast to the plane-parallel approximation used in MODTRAN.

5.2 Trace gas measurements

The key principle of the DOAS algorithm has been described in 3.3.1. In reality a few more complications arise. There are rapidly varying structures in the solar light, e.g. the *Fraunhofer lines* arising from absorptions within the sun itself. These features are partially filled in by Raman scattering in the atmosphere. Therefore the retrieval is in practice performed by the fit

$$\min \left| c_{\mathrm{f}} \log(F_i) + c_{\mathrm{r}} R_i + \sum_{j=1}^{N} \left[c_j \log(S_{ij}) \right] + P(i) - \log(M_i) \right|$$

Here,

M_i is the spectrum as measured aver instrument channels i

F_i is a spectrum little affected by absorption measured at high solar elevation, containing mainly the solar Fraunhofer structures to compensate for

R_i is an estimate of atmospheric Raman scattering, compensating for the Ring effect

S_{ij} is the reference differential absorption cross section of the j:th trace species included in the retrieval

$P(i)$ is a polynomial that filters out broad-band spectral features

and $c_\mathrm{f}, c_\mathrm{r}, c_j, j = 1 \ldots N$, are the fit coefficients to be determined.

The norm is in general the least-squares sum over a selected interval of spectrometer channels. This is the retrieval procedure implemented in the DOAS control and analysis software MFC [Gomer et al., 1995]. The sum over logarithms of reference spectra directly corresponds to adding optical densities; therefore the fit coefficients c_j directly yield the column densities (SCDs) of the included absorbing gases. The quality of the fit can be estimated from the residuals and from the coefficient c_f which should equal unity since the solar Fraunhofer absorption is constant. Error sources in the retrieval include wrong resolution and wavelength calibration of the reference spectra, inappropriate reference spectra for the absorption cross sections at stratospheric temperatures, omission of possibly important trace gases (e.g. SO_2) and aerosol absorptions, and rapidly varying spectral features due to etalon and polarisation effects in the instrument.

For gases with fairly constant atmospheric profiles, the results are presented as vertical gas columns by the earlier introduced approach VCD = SCD/AMF. For bromine oxide, however, which is rapidly undergoing photochemical cycles, the profile in itself depends on the solar zenith angle (SZA). Therefore the air mass factors cannot be calculated without a three-dimensional RTM where chemistry is taken into account in the first place. This seems like a circular problem and therefore an alternate approach is nowadays commonly used. The difference between the measured columns at two SZAs (differential slant column density, DSCD) is used, i.e

$$\mathrm{DSCD} = \mathrm{SCD}(\mathrm{SZA}_1) - \mathrm{SCD}(\mathrm{SZA}_2), \mathrm{SZA}_1 > \mathrm{SZA}_2$$

When comparing the results with the output of chemistry/transport models the DSCD is calculated by feeding the modelled columns into an RTM. This is the approach used in Paper V.

5.3 Colour index

As shown in chapter 3.4 the zenith-sky colour index, i e the ratio

$$\mathrm{CI} = \frac{I(\lambda_1)}{I(\lambda_2)}$$

where the wavelengths λ_1 and λ_2, chosen outside intervals affected by absorption, holds information on the importance of different scattering processes. Measurements have been reported e.g. by Rozenberg [1966], and Sarkissian et al. [1991, 1994] introduced its use for PSC detection by the SAOZ UV/visible spectrometers.

The CI is a relative measure and as is clear from the examples, it is its variation $\frac{d\mathrm{CI}}{d\mathrm{SZA}}$ with solar zenith angle SZA which is the quantity of interest. The CI is easy to calculate from the spectral counts S as

$$\mathrm{CI} = \frac{\left(\sum_{i=I_1}^{I_2} S_i\right)/\left(I_2 - I_1 + 1\right)}{\left(\sum_{j=J_1}^{J_2} S_j\right)/\left(J_2 - J_1 + 1\right)}.$$

Here, $[I_1, I_2]$ and $[J_1, J_2]$ are detector channel number intervals corresponding to wavelength intervals around λ_1 and λ_2.

In Paper I a simple MFC application was used for the calculation but later work has been implemented in Matlab for improved flexibility. The usage of the Matlab scripts is described in appendix B.1. Figure 5.3 outlines the algorithm. The channel number to wavelength calibration can, if desired, be fine-adjusted by identification of solar Fraunhofer lines in the spectrum. Solar zenith angles are calculated at the average time of the spectrum, i.e. the average of start and stop times of the integration. The time of these spectra are taken from the PC clock, which runs in UTC and is synchronised from NTP (Network Time Protocol)[1] servers at least once per week and should be accurate within one minute.

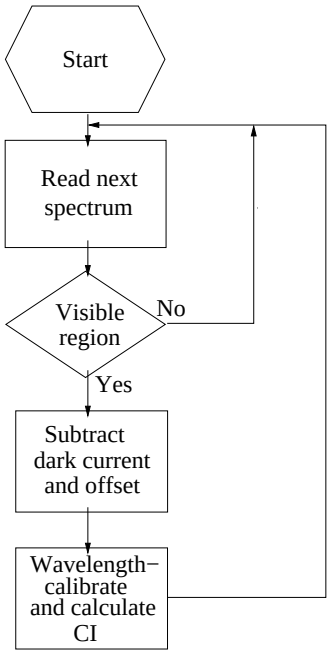

Figure 5.1: Principal flowchart of the `cibatch` algorithm used for calculation of the zenith-sky visible colour index.

As an example of how to interpret twilight CI variation, three weeks of data are shown in figures 5.2, 5.3 and 5.4.

Figure 5.2 is the normal development of CI during a week with clear weather, no PSCs and stable instrumental operation. The behaviour is qualitatively similar to the modelled idealisation in chapter 3.4. After sunset the zenith sky radiance is blue-shifted.

Figure 5.3, on the other hand, shows data from a week with obvious, visually evident PSC incidence. We note that there are strong redshifts of the zenith radiance. The modelling by Solomon et al. [1987] explains the fact that these peaks occur at a solar zenith angle around 94°; this is the limit of most of the zenith radiance originating from light scattered at altitudes higher than the PSC region at 20–30 km.

Peaks after twilight at smaller solar depressions can sometimes be observed, such as in a few cases from summertime shown in figure 5.4. These fit well together with high cirrus clouds. Peaks at higher solar zenith angles can also be observed. These are attributable to local light disturbances contributing more to the measured radiance than solar light, evident from the fact that the green mercury line (546 nm) is a prominent spectral feature.

[1] See http://www.ntp.org

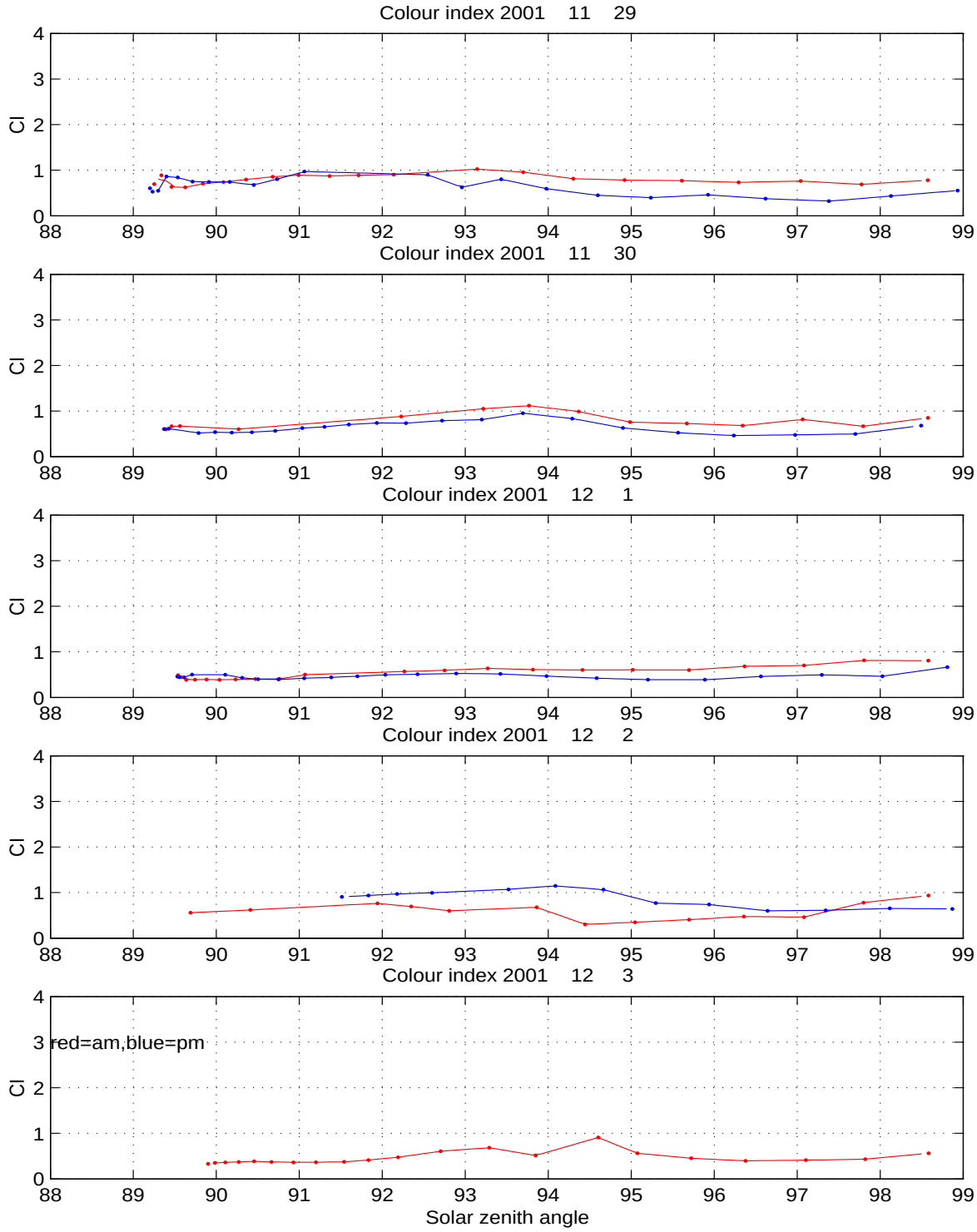

Figure 5.2: Twilight colour index development during a week without PSC presence. Note the qualitative similarity with the multiple-scattering model result shown in figure 3.7.

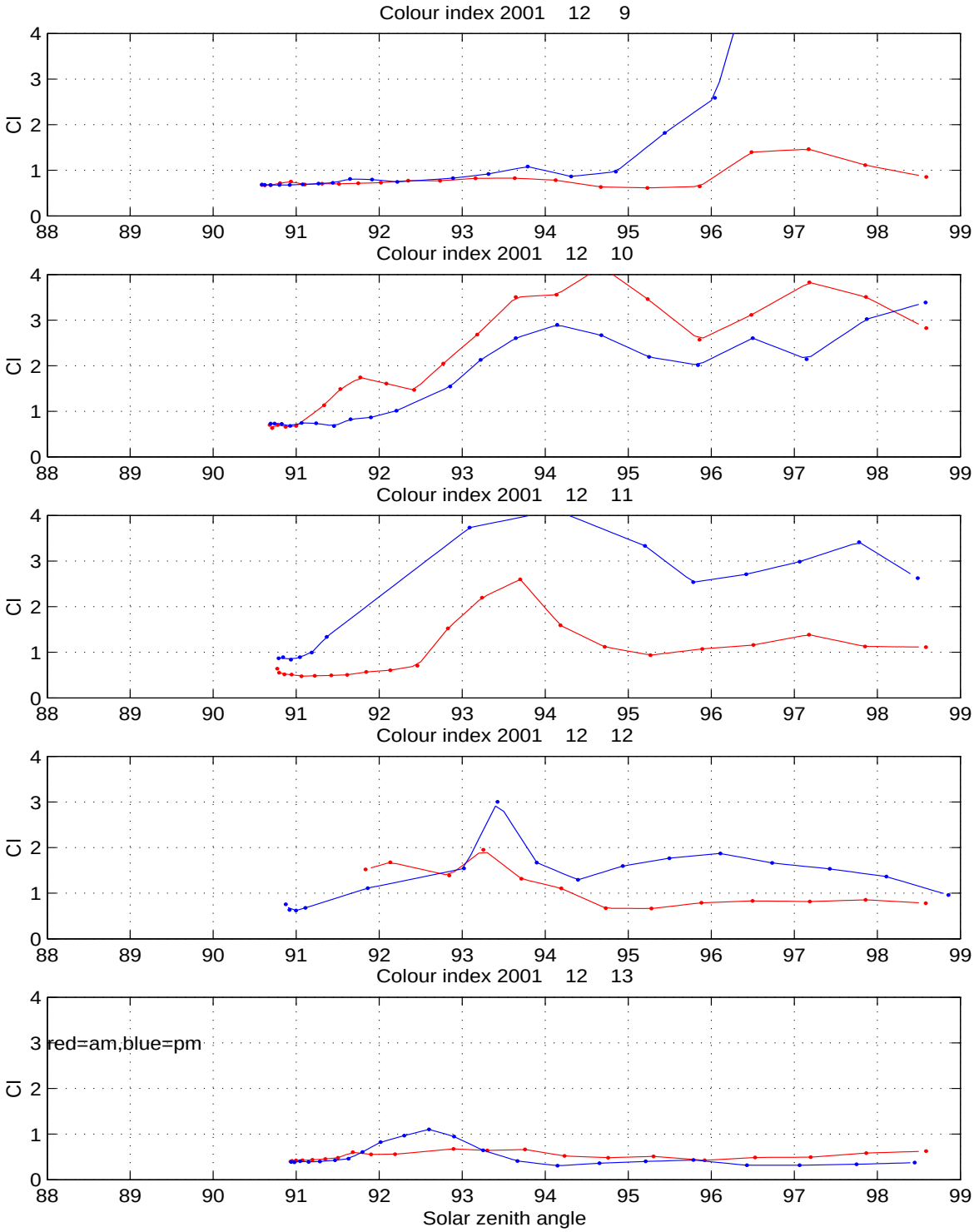

Figure 5.3: Twilight colour index development during a week with PSC presence on at least three days.

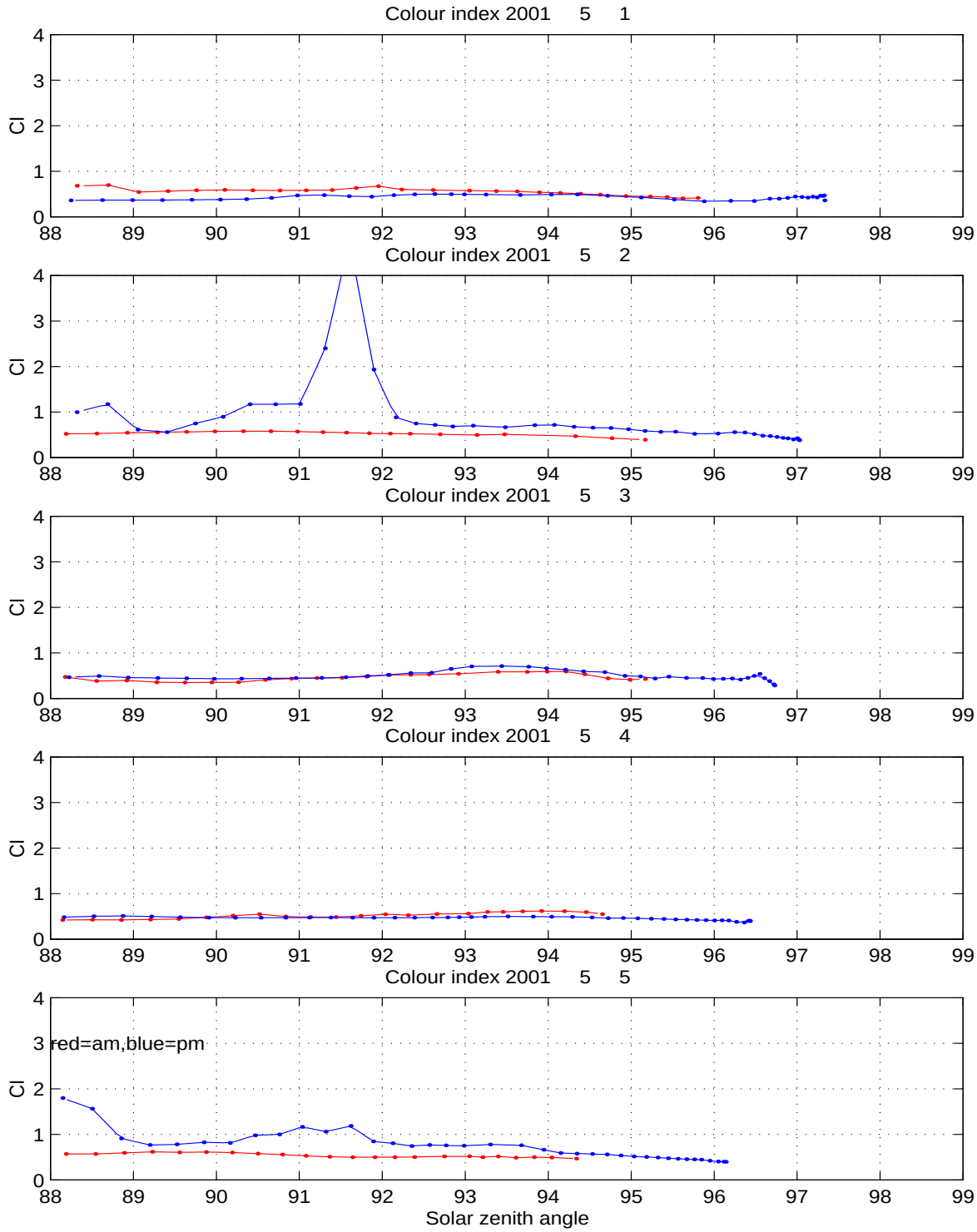

Figure 5.4: Twilight colour index development during a summer week. No PSCs should be present. However, on two occasions there are CI peaks during twilight. The solar zenith angles, close to sunrise/sunset, indicate typical signatures of high cirrus clouds.

Thus, experience shows that a colour index peak in the solar zenith angle range 94°–95°is the feature to use as an indicator for PSC presence. Comparisons of algorithms for this detection is the topic of paper III.

It can finally be noted that MODTRAN runs with its standard stratospheric (volcanic) aerosol included did not reproduce the enhanced redshifts during twilight. This is because of the one-dimensional, plane-parallel character of the model. Aerosol in the atmosphere will in general cause an enhanced blueshift unless the aerosol is localised in the scattering field of view of the instrument. A three-dimensional simulation would yield different results at different localisations of the aerosol, a result also found by [Sarkissian et al., 1991] in the single-scattering approximation. It can therefore be concluded that the method of discriminating CI peaks detects PSC occurrence in the field of view of the instrument (on the order of 1 km).

5.4 PSC imaging

There are a number of open questions regarding PSCs. One main topic is the importance of leewave-induced PSCs, relative to synoptic-scale occurrence, since this can cause discrepancies in chlorine activation and thus ozone destruction relative to what can be expected [Carslaw et al., 1998]. Also still to some extent unsettled is the interesting question regarding how representative the iridescent "mother-of-pearl" appearance is for PSCs.

These questions are difficult to address with only single-point measurements and models. Spatially separated simultaneous measurements, i.e. images, are required. The general principle of imaging was described in chapter 3.5. The key procedure in imaging studies is the mapping from the pixel plane to physical coordinates and in the case of PSCs, the estimation of scattering from the PSC volume elements (voxels). This cannot be done using the line-of-sight integrated values of a single image; rather, the same object must be imaged from two or more directions, i.e. bistatic or multistatic imaging. This work has concentrated on bistatic imaging with the two ALIS stations located according to figure 5.5 on January 9, 1997, which was a day with well-defined discrete PSC structures in the north and clear troposphere.

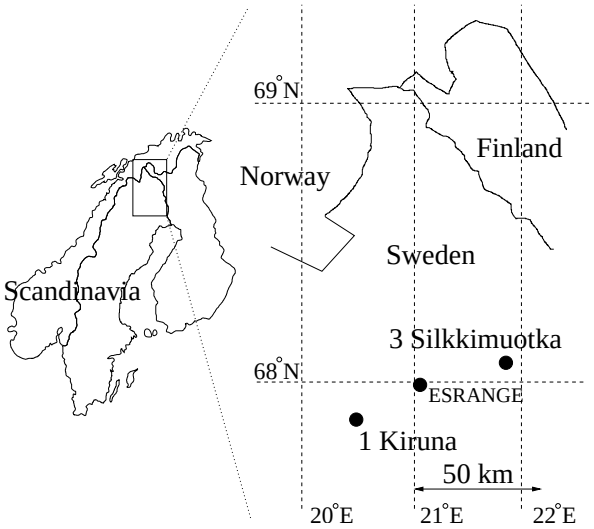

Figure 5.5: Map of the location of the ALIS cameras used in Paper IV.

Parameters	Description
f_x, f_y	Focal lengths in the two principal directions
u, v, w	The rotation angles of the camera
dx, dy	The deviation from the centre of the image of the projection of the optical axis
α	Correction for distortion (the deviation from ideal projection characteristic generally causing a barrel- or cushion-shaped image)

Table 5.1: The projection parameters used in ALIS imaging

5.4.1 Projection parameters

The mapping $I(u, v) = f(\varphi, \theta)$ is performed with an empirical optical model of the imager (lens/image detector system). In the case of ALIS the model has eight free parameters, summarised in table 5.1, which are determined by *star calibration*. The procedure has been developed and described by Gustavsson [2000].

The star calibration procedure is implemented in Matlab and operates manually or semi-automatically. An approximately projected sky map is superimposed on the image and the centre pixel coordinates of corresponding stars are to be identified in the image. A least-squares fit of the projection is run to minimise the Euclidean distances between identified stars and the sky map projections. Ideally a few hundred stars over the entire image could be identified; the order of 10 or more are required for the 8-parameter fit to work. When a good fit has been obtained the projection error ranges from sub-pixel values in the centre to no more than a few pixels at the edges of the image.

In order to see stars in the images of PSCs forming the basis for Paper IV, the background subtraction described in appendix B.6 was applied. In this way a sufficient number of stars for the fit of projection parameters could be identified for each orientation of the cameras. However, stars were not visible through the PSCs themselves. See figure 5.6.

5.4.2 Projections, triangulation and automatic altitude discrimination

The projections are used in two main senses. The first is determination of unknown altitude and the second is mapping of the PSC fields to known altitudes for photogrammetric measurements of their spatial scales. The most common approach to imaging altitude measurements is triangulation. Corresponding points are identified in pairs of images and the intersection of the lines of sight gives the physical coordinates by basic trigonometry. Figure 5.7 shows a practical example, where the two lines of sight do not intersect, indicating a pair of misidentified points. In reality triangulation means to minimise the perpendicular distance between the lines of sight and to identify the midpoint of that distance as the triangulated coordinates.

Since clouds do not have "surfaces" or "details" in a strict sense, but are still of rather well-defined spatial extent in the case of wave-generated clouds, another approach to altitude determination was also applied in paper IV. This algorithm resemble the way the human eyes define surfaces and distances in that the *altitudes of best overlapping projections* are searched. The algorithm is briefly described in the paper, including a flowchart. The most important parts of the algorithm are therefore described in pseudo-code here. In words, the algorithm calculates the correlation coefficients between $m \times n$-pixel sub-images of the projections of PSC images to successive altitudes, and the altitude of maximal correlation is chosen as the altitude of the object in sub-image (a, b). For distinct PSC structures in absence of tropospheric clouds, the best results were obtained when working with the correlation between the entire images, since only "PSC pixels" can be expected to correlate.

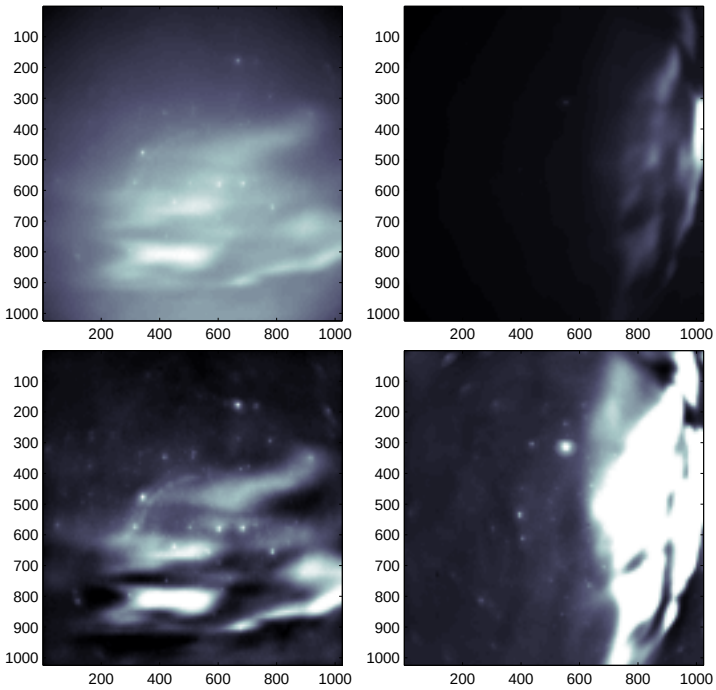

Figure 5.6: Example of data processing applied in Paper IV: ALIS images taken by Åke Steen on January 9, 1997, 15:21:30 UTC. Upper row: Raw images. Lower row: background-corrected and pixel scale limited images

```
/* Algorithm for projection overlap calculation */
WHILE images available
 image1:=imageinput(file1(i)),  image2:=imageinput(file2(i))
 find proj_parameters1,
 image1:=backgroundcorrect(image1),image2:=backgroundcorrect(image2)
 projectionaltitude=h(i)
 WHILE altitude<h(J)
  for all m,n
   projected image 1(i):=f(image1(i),proj_parameters1(i))
   projected image 2(i):=f(image2(i),proj_parameters2(i))
  /*m x n -pixel  subimages */
  subimage(1,m,n):=projectedimage1(am:a(m+1)-1,bn:b(n+1)-1)
  /* The same procedure for image 2 */
  correlation(m,n,j):=corrcoef(subimage1,subimage2)
  j:=j+1
  altitude:=h(j)
  end for
 LOOP
 H:=find max (correlation(m,n,[1,J]))
 object altitude (m,n) := h(H)
 i:=i+1
LOOP
```

Pseudo-code of the automatic altitude determination.

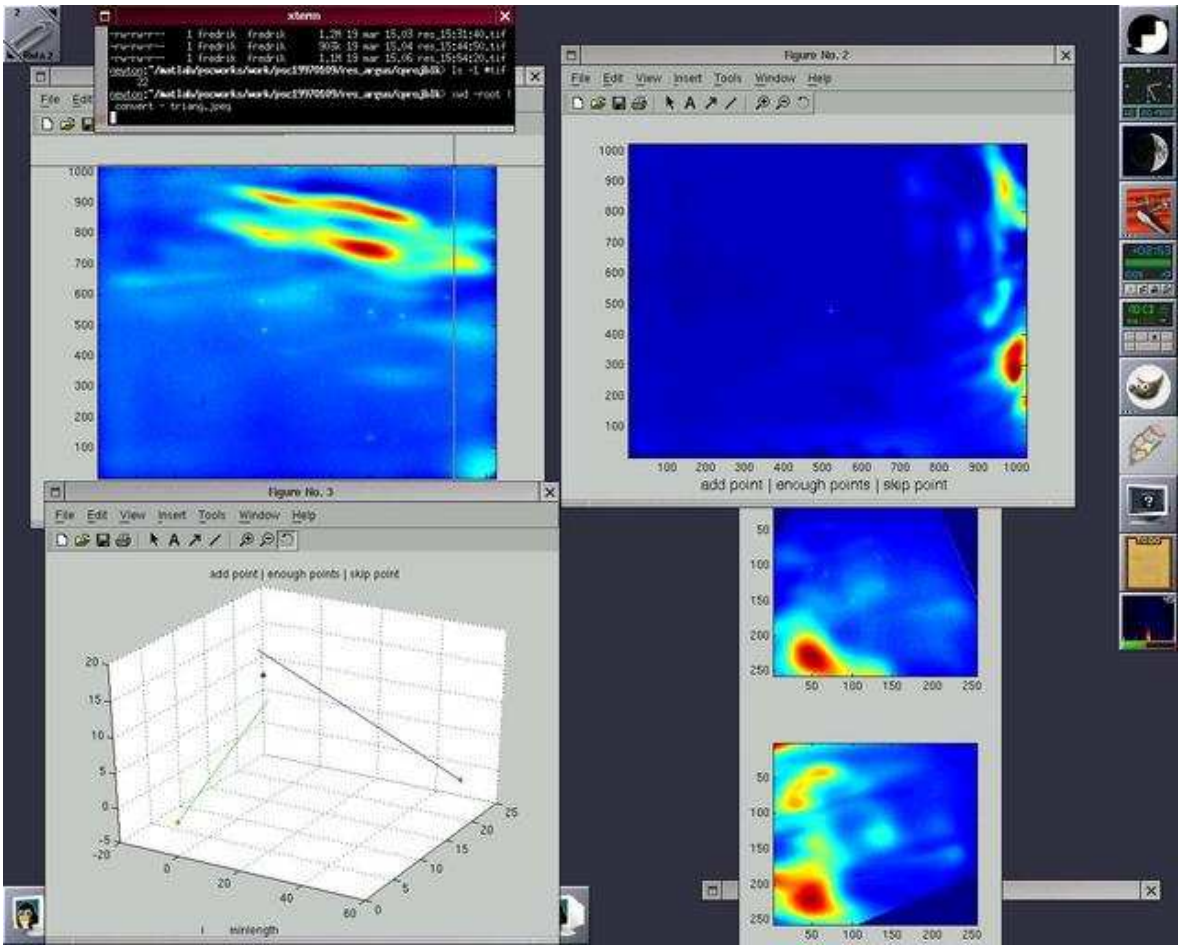

Figure 5.7: Triangulation by identification of corresponding points in progress. This example shows a clear misidentification of a pair of points: the lines of sight (lower left figure) do not intersect.

Chapter 6

Discussion

> The difference between art and science is that science is what we understand well enough to explain to a computer. Art is everything else.
> Donald Knuth

In the previous chapters the basic theory and the technical principles behind the included papers have been described. This chapter summarises and comments on the results obtained, focusing on the interpretation of the results in the context of presence of PSCs and their radiative and chemical consequences.

6.1 Applicability of different optical methods for PSC studies

Since the optical properties of particles such as aerosols depend on the geometry of scattering, both the position of observation and the properties of incident light are important. Most ground-based remote-sensing methods rely on one-point measurements from fixed locations (e.g. lidar). Thus these instruments cannot track the development of a PSC unless its location is stable over the time-span of a series of measurements with the instrument in question. It is also useful to have wind information from radiosondes. An advantage of active instruments is that they do not rely on sunlight. There is a method to overcome the problem of spatial versus temporal change, namely to fly airborne lidars along *quasi-Lagrangian* trajectories, i.e. flying with a velocity as close to the stratospheric air flow as possible, and thus track the development of particles within (almost) the same volume.

Satellite-borne instruments are independent of tropospheric and ground properties as long as they use the *limb* geometry (figure 6.1). Meerkötter [1995] used data from the GOME spectrometer on the ERS-2 satellite, using the nadir geometry in the infrared, and therefore faced the problem of varying *ground albedo* (reflectance of the Earth's surface) since effectively the radiant temperature of the atmosphere below the instrument is measured. Satellite-measured extinction has also been applied to retrieve large-volume size distributions of stratospheric aerosol, which is e.g. the purpose of the SAM data used for PSC retrieval by McCormick and Trepte [1986]. A disadvantage of satellites is that the temporal resolution depends on the orbit, so that there is no continuous coverage of a certain region.

To follow the development in general of PSCs throughout their lifetime of hours to days, two-dimensional imaging is advantageous since the positions where PSC particles can form (temperature minima at mountain wave crests) depend on the airflow (i.e. the mountain waves in the cases we consider here). Therefore PSCs may show a motion due to changes in the quasi-stationary wave pattern. By imaging these motions may be followed in their entire scale during several hours, such as in Paper IV. Imaging, however, poses large problems of interpretation. During twilight much of the

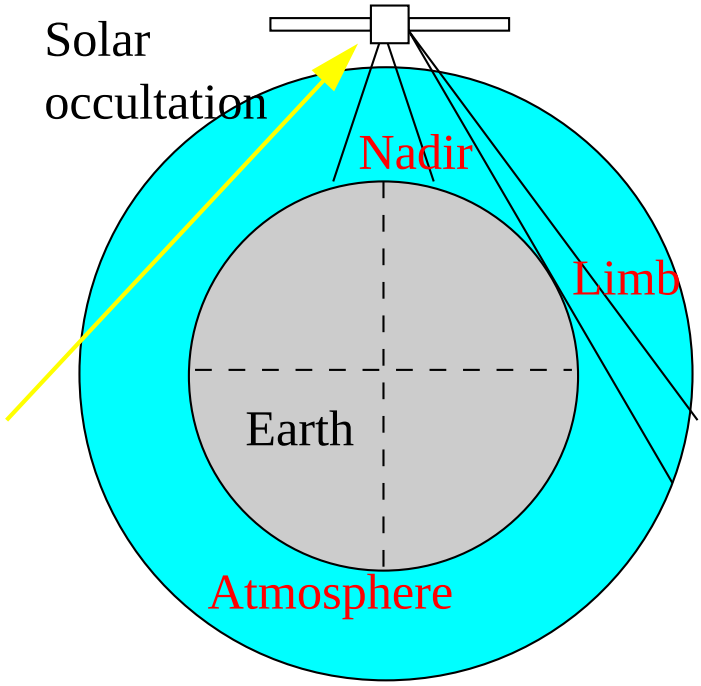

Figure 6.1: Geometry of satellite observations

sky background radiance originates from multiple scattering. Multiple scattering may also contribute to the visibility of PSCs, as is evident from the image series of paper IV. Images were obtainable even after sunset at PSC altitudes, although exposure times of a few minutes with cooled CCDs were required.

However, the single scattering geometry still has important implications for the results. As is pointed out in papers I and III, it is likely that this geometry limits PSC detectability with the zenith-sky colour index method. The discrepancy between synoptic temperatures below T_{NAT} and the much lower number of actually observed CI reddenings can be interpreted as tropospheric cloud-screening preventing detection. Figure 6.2 is a schematic overview. For the typical PSC altitudes of 18–30 km the tangent heights in the relevant interval of SZAs are at tropospheric cloud altitudes (down to 2 km). As is also shown in Paper I, the local time interval (solar azimuth range) corresponding to the solar zenith angles between 92°and 94°changes rapidly during the PSC season since it effectively starts at midwinter solstice and ends at vernal equinox. Another problem to consider is the fact (likewise pointed out in papers I and III) that the instrument has very often stopped working during Christmas holidays due to the less frequent maintenance available. Since these periods in general are coincident with the coldest periods of the year, statistically important data are missing from the time series of colour indices.

As concluded in the papers, a direct calibration of the method by intercomparing results from a network of ground-based stations with direct PSC observations by lidar or satellite is necessary. In addition, three-dimensional RTMs would be useful to study the impact of clouds at different positions in the troposphere on multiple scattering and zenith colour index during twilight.

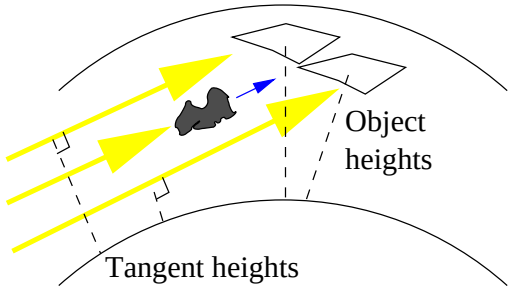

Figure 6.2: Twilight single-scattering geometry and the cloud-screening effect. See also paper IV.

6.2 Length and time scales of PSC processes

Time scales in PSC observations involve scattering of sunlight and the rotation of the Earth, synoptic wave activity determining the large-scale conditions, and the period and time of quasi-stability of airflow in mountain waves. As the results of e.g. Carslaw et al. [1998] show, this is important to study since even short-term PSC processing of air masses may have an impact on the ozone chemistry.

Appendix A shows a series of images (taken on negative film using an interval exposure timer) during similar conditions as the bistatic studies of paper IV, sunrise and sunset during PSC events in January 2000. Movements of the clouds as well as the impact of different conditions of illumination are evident.

There are wavelike structures on both large (distance between discrete clouds) and small (wavelike variations within a single cloud) scales, resembling the wavy appearance of lenticular clouds or noctilucent clouds. Figure 6.3 shows the types of wave structures which are commonly visible. The main aim of paper IV is a study of the inter-PSC wavelength by bistatic imaging in a suitable case when the tropospheric weather allowed observations. January 9, 1997 was chosen and the distance was measured to approximately 20 km. In the same case there was a quasi-periodic (period approximately 40 minutes) rising/sinking motion of the PSCs along a curved surface, which appeared both in the semi-automatic and the manual triangulation.

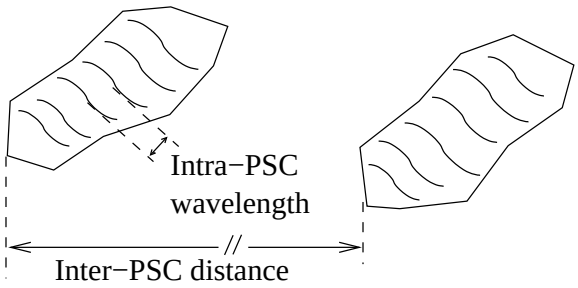

Figure 6.3: The wave structures observable in PSCs

6.3 The impact on trace gas measurements

The case of January 1997 is a good example of how dynamics, chemistry and optics are interlinked (see e.g. Bojkov and Balis [2001]). The dynamic situation created a "mini-hole" situation where the ozone

was mainly redistributed across the Arctic. This is seen in figure 6.4, where the results from Enell et al. [1997] are reprinted. A drop in measured ozone column densities occurred in mid-January. At the same time there was synoptic PSC presence, which led to strong chlorine activation and subsequent ozone destruction during the spring.

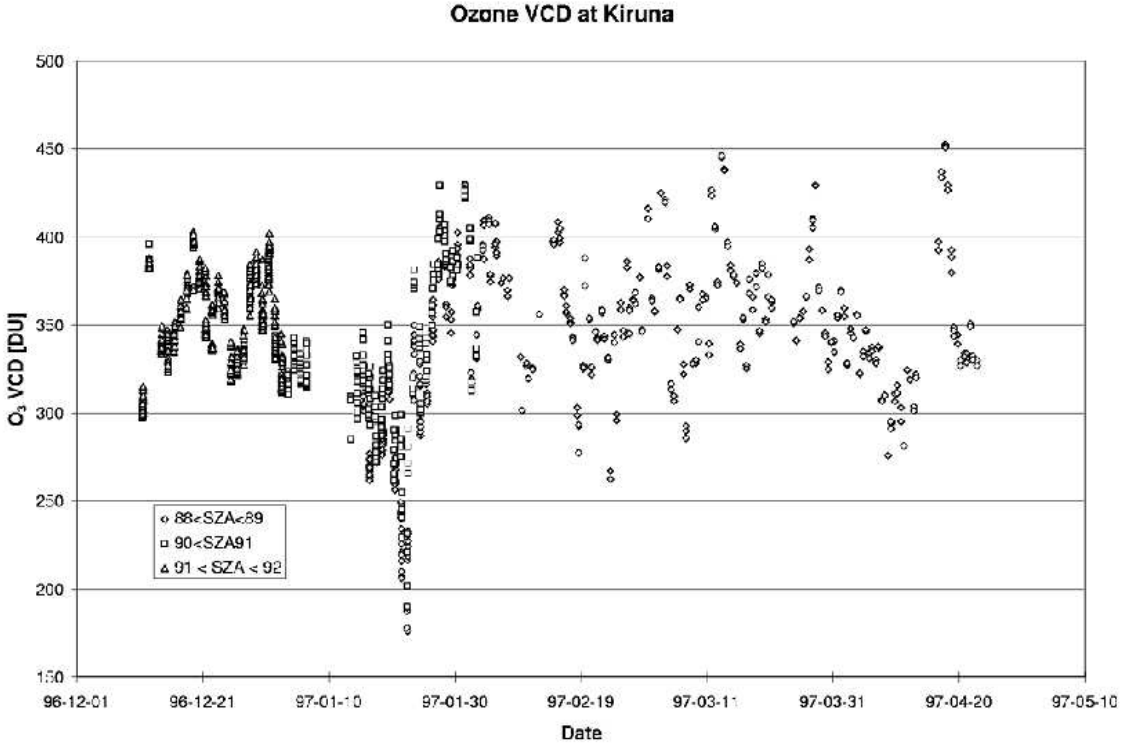

Figure 6.4: Time series of visible-range spectroscopic ozone column measurements in the winter of 1996–1997. Values at solar zenith angles of 90°and higher have been used as available (the sun is below the horizon until mid-January). Figure reprinted from Enell et al. [1997].

In this case it is also likely that the presence of PSCs caused an underestimation of stratospheric ozone since the air mass factors used were calculated for a "standard" ozone extinction profile whereas PSCs tend to screen part of the stratospheric column.

Paper V presents a comparison of measured bromine oxide (BrO) columns from several stations with results from the SLIMCAT model [Chipperfield, 1999]. The results are generally in good agreement and the discrepancies present could most easily be resolved by adjusting the reaction rates included in the model. However, the abovementioned consequences of PSCs can partly explain the discrepancies at Arctic stations. PSCs cause both additional halogen activation and denitrification (BrO model results may depend crucially on NO_x concentration), and thus modify reaction rates. The optical impact of PSCs on the measured differential slant columns may also be significant.

6.4 Conclusions

Two principal methods of optical remote-sensing have been applied, with inherently different areas of application, but taken together they can improve our understanding of PSC climatology.

A critical investigation of PSC detection with the zenith-sky colour index principle has been undertaken. There seem to be discrepancies as to when the method can detect PSC. In practice, the possibility to get a lower limit of PSC presence even in unfavourable tropospheric weather situations has turned out to be useful, and therefore real-time presentation of zenith-sky colour index should be continued wherever possible.

Imaging has been applied to study length- and time scales of the development of PSCs. As described in paper II, multimonochromatic imaging of the sky under different conditions (with geometry and interpretation similar to the zenith-sky colour index method) would also provide extended PSC detection capabilities and improve the understanding of multiple-scattering phenomena during twilight.

Concerning the issues of stratospheric chemistry, imaging studies show that microphysical parameters in PSC fields can change within the timescale required for processing of significant air masses inside the polar vortex, 30–60 minutes, due to wave activity. Since microphysical properties of PSC particles significantly affect reaction rates, this supports the idea that it is difficult to parameterise PSCs in chemistry/transport models (CTMs) of the stratosphere. The results of paper V can be interpreted as showing such discrepancies.

6.5 The future of PSC observations

An interesting issue for the future is whether it is possible to directly detect the chemical activation caused by the PSCs. Model runs indicate that release of active chlorine species may be effectively instantaneous in PSC fields [Carslaw et al., 1998]. However the effect of this activation cannot be seen until photochemical reactions have proceeded, which is a process taking place over timescales of weeks and starts only in the spring when sunlight is available.

Concerning PSC incidence statistics, satellite-borne spectrometers like SCIAMACHY on ENVISAT (which uses three different geometries of viewing) provide good opportunities for PSC mapping. Satellite measurements always involve checks of algorithm performance and therefore "ground-truth" is needed to validate the results.

Another interesting issue from a physical point of view is the possibility to use optical instruments to determine PSC particle properties and study the visibility of PSCs as related to atmospheric radiative transfer. A multispectral polarisation-sensitive imaging device would be suitable for these tasks. Today CCD cameras considerably facilitate quantitative measurements as compared with older imaging devices such as those used by Witt [1957, 1960].

As a conclusion, it is highly recommended to continue the optical studies of PSCs by comparing results from spectrophotometers at several stations in the Arctic, by applying new satellite-borne instruments, and by improving instruments and image-processing methods for multistatic PSC imaging.

Summary of included papers

Paper I: Occurrence of polar stratospheric clouds at Kiruna. Enell et al. [1999]

This paper resulted from discussions with Alain Sarkissian on the use of the zenith-sky colour index (CI) method for identification of PSCs, and interest from Kenneth Carslaw in ground-truth for PSC identification from satellite. The introduction of the paper comments on the importance of PSC statistics and continues with a definition of the colour index. Thereafter a few typical cases are studied and limitations of the CI and other methods are discussed. A threshold value for detection is identified. As a limitation of the method we comment on the rapid change of the local time intervals of twilight at high latitudes. Further limitations are addressed in Paper III.

Results for two winters are compared with PSC incidence inferred from ECMWF assimilated synoptic temperature fields. The following discussion addresses the questions of whether mountain leewaves is a significant cause of enhanced PSC occurrence.

Paper II: Multistatic imaging and optical modelling of nacreous clouds, Enell et al. [2000]

The iridescent colours of PSCs must be directly related to particle sizes[1]. Since the ALIS cameras allow multimonochromatic volume imaging, a simple algorithm for particle size retrieval is examined here. Only single-scattering by spherical particles is considered, thus disregarding all background light both from single and multiple scattering.

The algorithm works with ratios of radiances at different narrow quasi-monochromatic wavelength bands. It is numerically stable provided that data for a sufficient number of wavelengths are available (the 4–5 filter positions of the ALIS cameras seem to be sufficient).

Paper III: Detecting polar stratospheric clouds with zenith-looking photometers, Enell et al. [2002b]

This paper continues the work on PSC identification with the zenith-sky colour index. The simple calculation was reimplemented in Matlab, allowing an easy way to test different threshold conditions (applied to absolute colour index and different filtered values) for PSC detection. The resulting indicators were plotted against the temperature difference $T - T_{\mathrm{NAT}}$. A parabolic least-squares fit to the data around a solar zenith angle of 94°turned out to be a suitable way to filter out colour index reddenings caused by PSCs and avoid the impact of noise and tropospheric weather. However, values

[1]The colour pattern does not change in a rainbow-like fashion when a cloud is viewed from different direction, so refraction in large drops or particles is an unlikely explanation.

signifying PSC presence were only obtained for temperatures well below T_{NAT}. The effect of cloud screening of tangent rays is suggested as a cause for underestimation of PSC presenc.e

Paper IV: Case study of the development of polar stratospheric clouds using bistatic imaging, Enell et al. [2002a]

In this paper bistatic imaging is used for triangulation and for test of an algorithm for quasi-automatic altitude discrimination. The latter algorithm is also tested with a model case.

For the real case of January 9, 1997, both the automatic altitude determination and the triangulation show a quasi-periodic motion of the PSCs, indicating a fluctuation of the quasi-stationary wave pattern in which these PSCs formed. Discrete PSC structures were separated about 20 kilometres, indicating a wavelength scale which is not resolved in many dynamic and chemical models in use.

Paper V: Comparison of measurements and model calculations of stratospheric bromine monoxide, Sinnhuber et al. [2002]

This co-authored paper is a comparison of retrieved BrO columns from instruments around the northern hemisphere with results from the SLIMCAT model. The Kiruna UV/visible system, operated by the author of this thesis in cooperation with the University of Heidelberg, is one of the included instruments. The model is generally in good agreement with the results. Some discrepancies occur however, e.g. at the Arctic sites during spring.

From the point of view of this work it is mainly interesting that PSCs may affect the results in two senses. Firstly, a wrong estimation of PSC presence will lead to misestimation of the chemical reaction rates. Secondly, the optical properties of PSCs will lead to misinterpretation of the retrieved trace gas columns for measurements taken with PSCs above a station.

Bibliography

G. Anderson, F. Kneizys, J. Chetwynd, J. Wang, M. Hoke, L. Rothman, L. Kimball, and R. McClatchey. FASCODE/MODTRAN/LOWTRAN: Past/present/future. In *Proc. 18th Annual Review Conference on Atmospheric Transmission Models*, 1995.

C. F. Bohren. *Selected Papers on Scattering in the Atmosphere*, volume MS 7 of *SPIE Milestone Series*. SPIE Optical Engineering Press, 1989.

C. F. Bohren and D. R. Huffman. *Absorption and scattering of light by small particles*. John Wiley and Sons, Inc., New York, 1983.

R. D. Bojkov and D. S. Balis. Characteristics of episodes with extremely low ozone values in the northern middle latitudes 1957–2000. *Ann. Geophys.*, 19:797–807, 2001.

U. Brändström. PhD thesis, Swedish Institute of Space Physics, 2002. In preparation.

U. Brändström and Å. Steen. ALIS - a new ground-based facility for auroral imaging in northern Scandinavia. In *Proc. 11th Symposium on European Rocket and Balloon Programmes and related research*, pages 301–306. Eurpoean Space Agency, 1994. ESA SP-355.

D. Cariolle, S. Muller, F. Cayla, and M. McCormick. Mountain waves, polar stratospheric clouds, and the ozone depletion over Antarctica. *J. Geophys. Res.*, 94(D9):11233–11240, 1989.

K. S. Carslaw, T. Peter, and S. L. Clegg. Modeling the composition of liquid stratospheric aerosols. *Rev. Geophys.*, 35(2):125–154, 1997.

K. S. Carslaw, M. Wirth, A. Tsias, B. P. Luo, A. Dörnbrack, M. Leutbecher, H. Volkert, W. Renger, J. T. Bacmeister, E. Reimers, and T. Peter. Increased stratospheric ozone depletion due to mountain-induced atmospheric waves. *Nature*, 391(12):675–678, 1998.

K. V. Chance and R. J. D. Spurr. Ring effect studies: Rayleigh scattering, including molecular parameters for rotational Raman scattering, and the Fraunhofer spectrum. *Appl. Opt.*, 36(21): 5224–5230, 1997.

M. Chipperfield. Multiannual simulations with a three-dimensional chemical transport model. *J. Geophys. Res.*, 104:1781–1805, 1999.

P. J. Crutzen and F. Arnold. Nitric acid cloud formation in the cold Antarctic stratosphere: a major cause for the springtime "ozone hole". *Nature*, 324:651–655, 1986.

A. Dörnbrack, M. Leutbecher, J. Reichardt, A.Behrendt, K.-P.Müller, and G.Baumgarten. Relevance of mountain waves for the formation of polar stratospheric clouds over Scandinavia: Mesoscale dynamics and observations for January 1997. *J. Geophys. Res.*, 2000.

C.-F. Enell, U. Brändström, B. Gustavsson, S. Kirkwood, K. Stebel, and Å. Steen. Case study of the development of polar stratospheric clouds using bistatic imaging. *Ann. Geophys.*, 2002a. Submitted.

C.-F. Enell, B. Gustavsson, Å. Steen, U. Brändström, and P. Rydesäter. Multistatic imaging and optical modelling of nacreous clouds. *Phys. Chem. Earth*, 25(5–6):451–457, 2000.

C.-F. Enell, K. Stebel, T. Wagner, K. Pfeilsticker, and U. Platt. Detecting polar stratospheric clouds with zenith-looking photometers. *Sodankylä Geophysical Publication Series*, 2002b. Accepted.

C.-F. Enell, A. Steen, K. Pfeilsticker, T. Wagner, C. Otten, and U. Platt. UV/visible DOAS stratospheric trace gas measurements at Kiruna in the Arctic winter 1996-97. In *Proceedings of the 24th Annual European meeting on Atmospheric Studies by Optical Methods*, pages 155–160. Andøya Rocket Range, Norway, 1997.

C.-F. Enell, Å. Steen, T. Wagner, U. Frieß, and U. Platt. Occurrence of polar stratospheric clouds at Kiruna. *Ann. Geophys.*, 17:1457–1462, 1999.

D. W. Fahey, R. S. Gao, K. S. Carslaw, J. Kettleborough, P. J. Popp, M. J. Northway, J. C. Holecek, S. C. Ciciora, R. J. McLaughlin, T. L. Thompson, R. H. Winkler, D. G. Baumgardner, B. Gandrud, P. O. Wennberg, S. Dhaniyala, K. McKinney, T. Peter, R. J. Salawitch, T. P. Bui, J. W. Elkins, C. R. Webster, E. L. Atlas, H. Jost, J. C. Wilson, R. L. Herman, A. Kleinböhl, and M. von König. The detection of large HNO_3-containing particles in the winter Arctic stratosphere. *Science*, 291: 1026–1031, 2001.

J. C. Farman, B. Gardiner, and J. Shanklin. Large losses of total ozone in Antarctica reveal seasonal ClO_x/NO_x interaction. *Nature*, 315:207–210, 1985.

H. Frank. Ein Strahlungstransportmodell zur Interpretation von spektroskopischen Spurenstoffmessungen in der Erdatmosphäre. Master's thesis, Institute of Environmental Physics, Heidelberg University, Germany, 1991.

K.-H. Fricke, K. P. Müller, M. Serwazi, J. Reichardt, S. Kirkwood, Å. Steen, P. Hoffman, H. Mehrtens, A. Hauchecorne, F. Fierli, U.-P. Hoppe, and G. Hansen. Wind generated polar stratospheric clouds: The case of January 16, 1997 above Northern Scandinavia. In *Polar stratospheric ozone 1997, Proceedings of the fourth European symposium, Air pollution research report 66*, pages 127–130. European Commission, 1998.

O. Garcia, K. Pagan, P. Foschi, S. Gaines, and S. Hipskind. Detection of polar stratospheric clouds over Antarctica using AVHRR images obtained at Palmer Station during August 1992. *Polar Record*, 177(31):211–226, 1995.

T. Gomer, T. Brauers, F. Heintz, J. Stutz, and U.Platt. *MFC Version 1.98d User Manual*. Institute of Environmental Physics, Heidelberg University, Germany, 1995.

B. Gustavsson. *Three Dimensional Imaging of Aurora and Airglow*. PhD thesis, Swedish Institute of Space Physics, 2000. ISBN 91-7191-878-7.

D. Hanson and K. Mauersberger. Laboratory studies of the nitric acid trihydrate: Implications for the south polar stratosphere. *Geophys. Res. Lett.*, 15(8):855–858, 1988.

E. Hesstvedt. On the physics of mother of pearl clouds. *Geofysiske Publikasjoner*, XXI(9):1–32, 1960.

E. Hesstvedt. A two-dimensional model of mother-of-pearl clouds. *Tellus*, XIV(3):297–300, 1962.

G. C. Holst. *CCD arrays, cameras and displays*. SPIE Optical Engineering Press, Bellingham, Washington, USA, 1998.

J. R. Holton. *An introduction to dynamic meteorology*. Academic Press Inc., San Diego, 1992.

E. Hulburt. Explanation of the brigthness and color of the sky, particularly the twilight sky. *J. Opt. Soc. Am.*, 43(2):113–118, 1953.

C. E. Junge, C. W. Chagnon, and J. E. Manson. Stratospheric aerosols. *Journal of Meteorology*, 18: 81–108, 1961.

C. E. Junge and J. E. Manson. Stratospheric aerosol studies. *J. Geophys. Res.*, 66(7):2163–2182, 1961.

N. Larsen, I. Steen Mikkelsen, B. M. Knudsen, J. Schreiner, C. Voigt, K. Mauersberger, J. M. Rosen, and N. T. Kjome. Comparison of chemical and optical in situ measurements of polar stratospheric cloud particles. *J. Geophys. Res.*, 105(D1):1491–1502, 2000.

M. P. McCormick, G. S. Kent, W. H. Hunt, M. T. Osborn, L. R. Poole, and M. C. Pitts. Arctic polar stratospheric cloud observations by airborne lidar. *Geophys. Res. Lett.*, 17(4):381–383, 1990.

M. P. McCormick, H. M. Steele, P. Hamill, W. P. Chu, and T. J. Swissler. Polar stratospheric cloud sightings by SAM II. *J. Atm. Sci.*, 39:1387–1397, 1982.

M. P. McCormick and C. R. Trepte. SAM II measurements of Antarctic PSC's and aerosols. *Geophys. Res. Lett.*, 13(12):1276–1279, 1986.

M. B. McElroy, R. J. Salawitch, S. C. Wofsy, and J. A. Logan. Reductions of Antarctic ozone due to synergistic interactions of chlorine and bromine. *Nature*, 321(19):759–762, 1986.

R. Meerkötter. Detection of polar stratospheric clouds with ERS-2/GOME data. *Ann. Geophys.*, 13: 395–405, 1995.

A. Meinel and M. Meinel. *Sunsets, twilights, and evening skies*. Cambridge University Press, 1983.

H. Mohn. Perlemorskyer. In *Christiania Videnskabs-Selskabs Forhandlinger*, volume 2. A. W. Brøggers bogtrykkeri, 1893.

C. Otten, F. Ferlemann, U. Platt, and K. Pfeilsticker. Groundbased DOAS UV/visible measurements at Kiruna (Sweden) during the SESAME winters 1993/94 and 1994/95. *J. Atm. Chem.*, 30:141–162, 1998.

O. S. Ougolnikov and I. Maslov. Multi-color polarimetry of the twilight sky. The role of multiple scattering as the function of wavelength. Manuscript for Cosmic Research, private comm., 1999.

T. Peter. Microphysics and heterogeneous chemistry of polar stratospheric clouds. *Annual Review of Physical Chemistry*, 48:785–822, 1997.

U. Platt. *Air Monitoring by Spectroscopic Techniques*, chapter 2. Differential optical absorption spectroscopy. John Wiley and Sons, Inc., New York, 1994.

L. Poole, M. Osborn, and W. Hunt. Lidar observations of Arctic polar stratospheric clouds 1988: Signature of small, solid particles above the frost point. *Geophys. Res. Lett.*, 15(8):867–870, 1988.

J. Reichardt, A. Behrendt, R. Baumgart, and C. Weitkamp. Koordinierte Feldmessungen zum Einfluß von Leewellen auf Wolkenfelder in der polaren Stratosphäre. Technical Report GKSS 99/E/43, GKSS Forschungszentrum, Geesthacht, Germany, 1999.

G. V. Rozenberg. *Twilight*. Plenum Press, New York, 1966.

M. L. Salby. *Fundamentals of Atmospheric Physics*. Academic Press Inc., San Diego, 1996.

A. Sarkissian, J. Pommereau, F. Goutail, and E. Kyrö. PSC and volcanic aerosol observations during EASOE by UV-visible ground-based spectrometry. *Geophys. Res. Lett.*, 21(13):1319–1322, 1994.

A. Sarkissian, J.-P. Pommereau, and F. Goutail. Identification of polar stratospheric clouds from the ground by visible spectrometry. *Geophys. Res. Lett.*, 18(4):779–782, 1991.

J. Siebert, C. Timmis, G. Vaughan, and K. Fricke. A strange cloud in the Arctic summer stratosphere 1998 above Esrange (68°N), Sweden. *Ann. Geophys.*, 18:505–509, 2000.

B.-M. Sinnhuber, D. W. Arlander, H. Bovensmann, J. P. Burrows, M. P. Chipperfield, C.-F. Enell, U. Frieß, F. Hendrick, P. V. Johnston, R. L. Jones, K. Kreher, N. Mohamed-Tahrin, R. Müller, K. Pfeilsticker, U. Platt, J.-P. Pommereau, I. Pundt, A. Richter, A. M. South, K. K. Tørnkvist, M. van Roozendael, T. Wagner, and F. Wittrock. Comparison of measurements and model calculations of stratospheric bromine monoxide. *J. Geophys. Res.*, 2002. Accepted.

S. Solomon. Stratospheric ozone depletion: A review of concepts and history. *Rev. Geophys.*, 37(3): 275–316, 1999.

S. Solomon, R. R. Garcia, F. S. Rowland, and D. J. Wuebbles. On the depletion of Antarctic ozone. *Nature*, 321:755–758, 1986.

S. Solomon, A. L. Schmeltekopf, and R. W. Sanders. On the interpretation of zenith sky absorption measurements. *J. Geophys. Res.*, 7:8311–8319, 1987.

P. Stammes, J. de Haan, and J. Hovenier. The polarized internal radiation field of a planetary atmosphere. *Astronomy and Astrophysics*, 225:239–259, 1989.

K. Stamnes, S.-C. Tsay, W. Wiscombe, and K. Jayaweera. Numerically stable algorithm for discrete-ordinate-method radiative transfer in multiple scattering and emitting layered media. *Appl. Opt.*, 27(12):2502–2509, 1988.

Å. Steen and U. Brändström. ALIS - a multi-station ground-based imaging system at high latitudes. *STEP SIMPO Newsletter*, 3(5), 1993.

C. Störmer. Remarkable clouds at high altitudes. *Nature*, February 1929.

C. Störmer. Photogrammetrische Bestimmung der Höhe von irisierenden Wolken (Perlmutterwolken) am 30. Dezember 1926. *Geofysiske Publikasjoner*, 5(2):1–8, 1930.

C. Störmer. Höhe und Farbenverteilung der Perlmutterwolken. *Geofysiske Publikasjoner*, 9(4):1–27, 1932.

A. Tabazadeh, O. B. Toon, and E. J. Jensen. Formation and implications of ice particle nucleation in the stratosphere. *Geophys. Res. Lett.*, 24(16):2007–2010, August 15 1997.

M. A. Tolbert. Polar clouds and sulfate aerosols. *Science*, 272:1597, 1996.

O. B. Toon, P. Hamill, R. P. Turco, and J. Pinto. Condensation of HNO_3 and HCl in the winter polar stratospheres. *Geophys. Res. Lett.*, 13(12):1284–1287, 1986.

A. Tsias, A. J. Prenni, K. S. Carslaw, T. P. Onasch, B. P. Luo, M. A. Tolbert, and T. Peter. Freezing of polar stratospheric clouds in orographically induced strong warming events. *Geophys. Res. Lett.*, 24(18):2303–2306, 1997.

C. Voigt, A. Tsias, A. Dörnbrack, S. Meilinger, B. Luo, J. Schreiner, N. Larsen, K. Mauersberger, and T. Peter. Non-equilibrium compositions of liquid polar stratospheric clouds in gravity waves. *Geophys. Res. Lett.*, 27(23):3873–3876, 2000.

T. Wagner. Spektroskopische Messung stratosphärischer Spurenstoffe im arktischen Winter 1993/94: Abweichungen von der normalen Spurenstoffzusammensetzung. Master's thesis, Institute of Environmental Physics, Heidelberg University, Germany, 1994.

G. Witt. Noctilucent cloud observations. *Tellus*, 9(3):365–371, 1957.

G. Witt. A note to the paper by G. Witt, 'polarization of light from noctilucent clouds'. *J. Geophys. Res.*, 65(7):2199–2200, 1960.

A. Young. On the Rayleigh-scattering optical depth of the atmosphere. *J. Appl. Met.*, 20:328–330, 1980.

Acknowledgements

All scientific work derives from the work of others. Pioneers in the field, like Henrik Mohn and Carl Störmer, must not be forgotten. Many of the ideas used in my work are directly or indirectly inspired by their work in the early 20th century. I also wish to thank Georg Witt for his skills in experimental methods and for pointing out the importance of knowing the original sources of "old" ideas.

I also extend my thanks to all those who have helped me during the years in Kiruna—my coauthors, my supervisors Kerstin Stebel and Sheila Kirkwood, all colleagues at IRF for discussions, and my former supervisor Åke Steen for directing my interest towards stratospheric clouds. Special thanks to Björn Gustavsson for his knowledge in image processing. Much of the work has resulted from cooperation with Klaus Pfeilsticker, Thomas Wagner and Udo Frieß at the university of Heidelberg.

Financial support for my position at IRF was provided by Miljö- och Rymdforskningsinstitutet (MRI) in Kiruna during 1996–2000.

Without good friends around I could never have written this thesis. Among many others, not to be forgotten, I wish to thank Johan Arvelius, Sachiko Joko, Andreas Söderberg and Georg Sundström. Jenny Ivarsson has been involved in long scientific and philosophic e-mail discussions.

Special thanks to the friends who have always been there in both happy and sad moments, Urban Brändström and Anette Snällfot.

Till slut vill jag uttrycka min tacksamhet till mina föräldrar som alltid låtit mig gå min egen väg genom livet, så att jag kunnat följa den akademiska banan och dessutom hamna 150 mil—både en kort sträcka och en oändlighet—hemifrån.

Appendix A

PSC images

The appearance of mother-of-pearl clouds under certain typical circumstances is shown in the following image sequences. The wave structures in the mother-of-pearl clouds can be clearly seen. Sometimes the structures have a dynamic and obviously nonlinear appearance, which might be caused e.g. by breaking mountain leewaves.

The following series of photographs of PSC events, taken with a camera with automatic interval exposure, shows examples of this development. We note that certain parts of the PSCs vanish between images. This may be a real evaporation or, in certain cases, more likely an effect of tropospheric cloud screening of incident sunlight.

Figure A.1: Images of PSCs south of Kiruna taken using an automatic interval timer during the afternoon of January 27, 2000. Times are in UTC; local time is UTC + 1h.

Figure A.2: Time series of PSC images taken from the roof of the Swedish Institute of Space Physics during sunrise on January 26, 2000. The lens was zoomed out after image 4 to show a wider area of interest. Times are in UTC; local time is UTC + 1h.

Appendix B

Matlab and C routines

For the work described in Papers II,III and IV, a number of routines in Matlab and C have been implemented. These are available on request from the author. A short introduction is included here. This documentation only describes the main routines intended for final use, not the subroutines they depend on.

B.1 UV/visible spectra

read_sp.m

Syntax: `[info,spectrum]=read_sp(fname)`

Reads a UV/visible spectrum in MFC format from file *fname*, reporting the MFC header information in the struct *info* and the spectral channels in *spectrum*.

fr_cal.m

Syntax: `[wl,linesfound]=fr_cal(spectrum,sptype)`

Matches minima in *spectrum* to solar Fraunhofer lines (*linesfound* lines) and provides an array of wavelengths *wl* calculated by a polynomial fit $wl = P(C)$, where wl is the wavelength and C the spectral channel number. An approximate calibration must be provided as polynomial coefficients $p_n, n = 0, 1..N$ for the expansion $\lambda(C) = \sum_{n=0}^{N} p_n C^n$. In the current version these values are hard-coded in the Matlab file. It is possible to include values both for visible (*sptype*=1) and UV (*sptype*=2) spectra.

cibatch.m

Syntax: `OK=cibatch(sp_path,outfile,cal,L1low,L1hi,L2low,L2hi)`

Uses the above functions to calculate colour indices for all visible spectra found in subdirectories of *sp_path*. The results are written to *outfile*. For *cal*=0 the limits *L1low,L1hi,L2low,L2hi* should be given as channel numbers for the desired, "red" and "blue" regions, For *cal*=1, wavelength ranges can be given provided that the appropriate approximate calibration coefficients are inserted in `fr_cal.m`.

B.2 Mie routines

mkunpolint

Syntax: `mkunpolint <wavelength (micrometers)> <i|w> <nangles> <minradius> <rstep> <nradii> extout<y|n>`

This is a supporting C/Fortran code, providing input for the Matlab routines described below, developed using the Mie code by Bohren and Huffman [Bohren and Huffman, 1983] together with refractive indices given by routines by P.J. Flatau and S.G. Warren.

Select **i** to use the refractive index of ice or **w** for that of liquid water. *Nangles* is the number of angles between 0 and 90 degrees, *minradius* is the start radius in micrometers,*rstep* is the radius step, *nradii* is the total number of radii, and *extout*=**y** prints extinction coefficients as comments. Output is written to standard output and should be redirected into a file.

B.3 PSC particle size retrieval

Routines for particle size retrieval as applied in Paper III, assuming no Rayleigh background but only Mie scattering by PSC particles. Ratios of the colour ratios at two scattering angles for as many pairs of wavelengths as possible are used to retrieve the radii of scattering particles.

findrads.m

Syntax: `best_rad=findrads(r_inters)`

Finds the best matching radii (vector *best_rad*) given *r_inters*, a *(npixels x nratios)* matrix of the radii of intersection between a number of measured colour ratio ratios and theoretically tabulated ones (for any number of PSC pixels), either given by experiment or modelled by `mkrads.m`.

findrads3.m

Syntax: `best_rads=findrads3(r_inters)`

As `findrads.m` but gives a matrix of the three best solutions for each PSC pixel.

mkrads.m

Syntax: `[r_inters]=mkrads(v1,v2)`

Models a matrix of a number of colour ratio ratios as those would be observed at scattering angles *v1* and *v2* (degrees), assuming no sky background and single Mie scattering. The user should modify the script for proper read-in of Mie data. Adding of noise is also possible and this can likewise be modified in the file.

get_profile.m

Syntax: `section=getprofile(r0,dv,l,img,stat,optpar,pflag)`

Get pixel values along the line specified by *r0=[x0,y0,z0]*, *dv=[dx,dy,dz]* and length *l* from image *img* assuming station no *stat* and optical parameters *optpar*. Useful together with images taken at different wavelengths and from different stations to prepare colour index ratios.

B.4 PSC modelling

sunpos.m

Syntax: `[sza,saa]=sunpos(latitude,longitude,dayofyear,time)`

Calculates the zenith and azimuth angles *sza* and *saa* of the sun at a given geographical location *latitude,longitude*, day of year *dayofyear* and time *time* (seconds after midnight UTC).

scat_to_stat.m

Syntax: `v=scat_to_stat(x,y,z,sno,sza,azi)`

Returns a matrix of the scattering angles from the points given by the matrices *[x,y,z]* (coordinates in kilometres from Kiruna, as obtained by `meshgrid`) to ALIS station number *sno* for given position *(sza,azi)=(zenith angle, azimuth angle)* of the sun.

pscprep.m

Syntax: `[x,y,z,phi,R]=pscprep(month, day, hour, min, sno, x0, y0, z0, xdim, ydim, zdim, xscal, yscal, zscal, r1, a1, b1, c1)`

Prepares 3-D matrices *(phi,R)* of scatter angles and Gaussian radii given by *r1,a1,b1,c1* for a model PSC at position (lower left corner) *r0=[x0 y0 z0]* km from Kiruna and spatial extension *(xdim,ydim,zdim)* (km) seen from station sno at time (month,day,hour,min). For convenience also the matrices *(x,y,z)* are output, describing the coordinates of each point where *(phi,R)* are defined (as obtained by `meshgrid(x0:xscal:x0+xdim-xscal,...)`).

pscscatf.m

Syntax: `[scatvol]=pscscatf(data,phi,R)`

Using the lookup table *data* of Mie functions for a certain wavelength, as produced by `mkunpolint` described above (B.2), this routine provides a 3-D matrix *scatvol* of scattering phase functions for the scattering angles and particle radii given by the matrices *phi* and *R*, respectively. The result can be thought of as a voxel volume that can be projected onto images using suitable routines.

B.5 Altitude determination

pscaltdet.m

Syntax: `[corrs,maxcorr,bestalts,bproj1,bproj2,op1,op2]=`
`=pscaltdet(fn1,fn2,alts,xvec,yvec,bbls,cbls,rsize,old_op1,old_op2)`

Altitude determination using pairs of images can be performed by direct triangulation, but this is often a difficult task. Alternatively, since the optical parameters of the cameras are known from star calibration, an automatic overlap matching can be possible. The principle is to project the images in files *fn1,fn2* to altitudes *alts*, mapped over the region defined by *(xvec,yvec)* kilometres from Kiruna. The images are first rescaled to size *rsize* and background-corrected according to the procedure below with minimum search in image sub-blocks of size *bbls*. Correlations are performed over sub-blocks of size *cbls*. The function searches for the projection parameters for each image in a list and stores the corresponding projection matrices. If the parameters match *old_op1* and *old_op2* the stored projection matrices are reused. The function reports all correlations in *corrs*, their maximum values over all *alts* in *maxcorr*, the corresponding altitudes in *bestalts*, and the block-wise best projections in *bproj1,bproj2*. It is advisable to set *old_op1=op1* and *old_op2=op2* after each run to prevent the function from unnecessary repetition of projections.

B.6 Image preprocessing

pscbg.m

Syntax: `bg=pscbg(img,bsize)`

This function implements a simple approach to background correction of PSC images. The minimum pixel value in each image sub-block of size *bsize* in the image *img* is found. A smooth bicubic surface is fitted to these values, rescaled to the size of the original image *img* and subsequently output in *bg*.

Appendix C

Radiometric quantities

There are an enormous amount of similar but not always equivalent definitions of radiometric quantities and often a large variety of units for each quantity. This table summarises those used in this work, follow the SI definitions.

Quantity	Symbol	Description	SI Unit
Radiance	L	Power emitted/received per unit area from/into unit solid angle	$\mathrm{Wm^{-2}sr^{-1}}$
Irradiance	I	Integrated power per unit area	$\mathrm{Wm^{-2}}$
Radiant flux	Φ	Power per unit solid angle	$\mathrm{Wsr^{-1}}$

Table C.1: Radiometric quantities and their SI units.

Written as in this table, the quantities refer to spectrally integrated measurements. Spectral versions of the above quantities can also be defined, according to

$$dL = L(\lambda)d\lambda$$

$$dI = I(\lambda)d\lambda$$

$$d\Phi = \Phi(\lambda)d\lambda$$

The spectral quantities thus refer to measurements over a *small* wavelength interval dλ. For longer wavelength intervals they must be integrated:

$$X = \int_{\lambda_1}^{\lambda_2} X(\lambda)d\lambda$$

where X is any of the above quantities.

There are also a number of commonly used *photometric units*, applicable to measuring the above quantities weighted with the spectral response of an average human eye. These are useful in ergonomic studies but should otherwise be avoided.

Paper I

Carl-Fredrik Enell, Åke Steen, Thomas Wagner, Udo Frieß, Klaus Pfeilsticker, Ulrich Platt and K-H Fricke. **Occurrence of polar stratospheric clouds at Kiruna**. *Ann. Geophys.*, 17:1457–1462, 1999.

Ann. Geophysicae 17, 1457–1462 (1999) © EGS – Springer-Verlag 1999

Annales Geophysicae

Occurrence of polar stratospheric clouds at Kiruna

C.-F. Enell[1], **Å. Steen**[1], **T. Wagner**[2], **U. Frieß**[2], **K. Pfeilsticker**[2], **U. Platt**[2], **K.-H. Fricke**[3]

[1] Swedish Institute of Space Physics, P.O. Box 812, SE-98128 Kiruna, Sweden
[2] Institute of Environmental Physics, Heidelberg University, INF 229, D-69120 Heidelberg, Germany
[3] Institute of Physics, Bonn University, Nussallee 12, D-53115 Bonn, Germany

Received: 7 May 1999 / Revised: 2 July 1999 / Accepted: 7 July 1999

Abstract. Polar stratospheric clouds (PSCs) are often observed in the Kiruna region in northern Sweden, east of the Scandinavian mountain range, during wintertime. PSC occurrence can be detected by ground-based optical instruments. Most of these require clear tropospheric weather. By applying the zenith-sky colour index technique, which works under most weather conditions, the data availability can be extended. The observations suggest that PSC events, especially of type II (water PSCs) may indeed more common than predicted by synoptic models, which is expected because of the frequent presence of mountain-induced leewaves. However, it will be of importance to increase the density of independent observations.

Key words. Atmospheric composition and structure (aerosols and particles, cloud physics and chemistry) · Meteorology and atmospheric dynamics (mesoscale meteorology)

1 Introduction

It is well known that Polar Stratospheric Clouds (PSCs), which develop in the winter polar vortex at altitudes of typically 25 km, are of major importance in stratospheric chemistry (Solomon *et al.*, 1986). They may also be important as an indicator of climate change, but the correlation between the frequency of PSC observations and stratospheric cooling is still not well known. This is in itself a good reason for improving statistics on PSC occurrence.

Normally PSC presence is inferred from modelled synoptic temperatures, such as provided by the European Centre for Medium-Range Weather Forecasts (ECMWF). That method does not account for PSC formation by local cooling in mountain-induced waves, which can be observed in certain areas close to mountain ridges, such as the Kiruna region in northern Sweden.

It has been proposed by Carslaw *et al.* (1998) that these wave-induced PSCs may be a major cause of the discrepancies between observed and modelled ozone loss. However, their importance is still the object of much controversy. An experimental climatology of actual PSC observations is therefore desirable, which means that the density of such observations must be increased. A number of optical remote-sensing instruments suitable for that purpose are at present in operation around the Scandinavian mountain range, both active (lidars) and passive (spectrometers and cameras).

The final aim may be PSC mapping using satellite data (Garcia *et al.*, 1995; Meerkötter, 1995). This procedure will require calibration against ground-based instruments.

2 Methods

2.1 Zenith-sky colour index

The zenith-sky colour index method was proposed as a way of obtaining PSC statistics in all tropospheric weather conditions and has been described by Sarkissian *et al.* (1991). In principle the method is very simple and any spectrometer or combination of filter photometers covering a suitable interval in the visible spectral range can be used. A short outline of the technique follows. For further details the reader should consult Sarkissian *et al.* (1991) and the references therein.

Taking the integrated intensities $I(\lambda_1)$ and $I(\lambda_2)$ over two wavelength intervals around λ_1 and λ_2 a *colour index* can be defined as:

$$\mathrm{CI} = \frac{I(\lambda_1)}{I(\lambda_2)} \tag{1}$$

Correspondence to: C.-F. Enell,
e-mail: carl-fredrik.enell@irf.se

This colour index varies with the solar zenith angle (SZA), tropospheric cloud cover, varying absorptions, aerosols, etc.* In general we will write CI=CI(SZA). When PSCs or other layers of enhanced scattering, such as tropospheric clouds, are present, the SZA dependence of the colour index will change. In general reddenings (i.e. increased intensities at longer wavelengths compared to the case of pure clear-sky Rayleigh scattering) will be observed in certain SZA intervals.

Since December 1996, a zenith-looking UV/visible spectrometer system is in operation at the Swedish Institute of Space Physics (in Swedish *Institutet för Rymdfysik*, abbreviated IRF), 67.8°N, 20.4°E, 418 m above sea level. The instrument is used on a routine basis for retrieval of total column densities of the species ozone, NO_2, BrO and OClO using the Differential Optical Absorption Spectroscopy (DOAS) method (Platt, 1994).

Wavelengths (in our case, integrated over 5 out of 1024 instrument channels at the ends of the spectral intervals covered by the instruments) were selected according to Table 1. These wavelengths should preferrably be selected outside regions of large varying absorptions. It should be emphasized that these colour indices are relative quantities, since the characteristics of the filters used, spectral response of the detectors, etc, need not necessarily be known.

2.2 Detection of PSCs

For experimental validation of the method, four ideal type cases according to Table 2 were identified from records of visual meteorological observations. Colour indices (Eq. 1) were then calculated for the solar zenith angle (SZA) intervals $85° < SZA < 96°$ over the sunset periods of those days (Fig. 1).

2.2.1 The non-PSC cases. The clear-day curve shows exactly the behaviour of *CI* vs *SZA* that can be expected from our everyday experience of the appearance of the evening sky. After sunset the sky reddens slightly as expected due to Rayleigh scattering along the increasing optical path the sunlight has to traverse. After SZA ≈ 92° a blueing sets in, which at first may seem unexpected although it agrees with visual observation. This long-known phenomenon is due to ozone Chappuis absorption, as explained e.g. by Hulburt (1953), and possibly aerosol scattering. A comprehensive description of twilight sky phenomena, including colour index variation, can be found in Rozenberg (1966).

For the cloudy days the sky is reddened to an extent varying with the cloud cover during daytime. During twilight the colour index falls off towards its clear-sky values as tropospheric clouds fall into darkness.

2.2.2 The PSC cases. For the days with PSC presence the CI shows approximately the same behaviour as on non-PSC days for $SZA < 90°$. The clear-sky case shows a positive slope (slow reddening) whereas the cloudy-sky case shows a slow blueing up to a solar zenith angle of ≈92°. This SZA corresponds to an altitude of maximal scattering (Solomon *et al.,* 1987) at typical PSC altitudes. There, a significant reddening occurs (CI up to one order of magnitude larger than in the non-PSC cases).

Two effects may contribute to this reddening: enhanced scattering of sunlight reddened by Rayleigh extinction along the long atmospheric optical path at twilight, and the significantly different wavelength dependence in scattering by large particles as opposed to the $1/\lambda^4$ dependence of scattering by air molecules. This mechanism is clearly not strongly affected by clouds in the (during twilight relatively dark) troposphere between the instrument and the PSC layers.

A further understanding of the process can be gained by multiple-scattering Monte-Carlo radiative transfer modelling, which is work in progress.

2.2.3 Uncertainties. Cases other than the ideal ones described above are important to examine. For instance, the results of Fig. 2 are of special interest. They were obtained using data from days that, according to the

Table 1. Wavelengths used for calculation of the CI

	Present work	Sarkissian *et al.*
λ_1	680 nm	550 nm
λ_2	385 nm	350 nm

Table 2. Days (YYMMDD) of ideal observational conditions

	Clear sky	Cloudy sky
No PSC	980302	980324
PSC	970116	970121

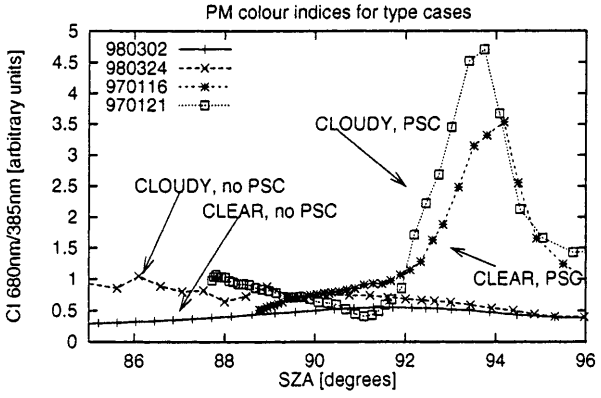

Fig. 1. Colour index development during twilight in the four type cases of Table 2

* Colour is a physiological rather than a physical quantity, but an increase of the colour index as defined here will indeed correspond to a reddening of the zenith sky.

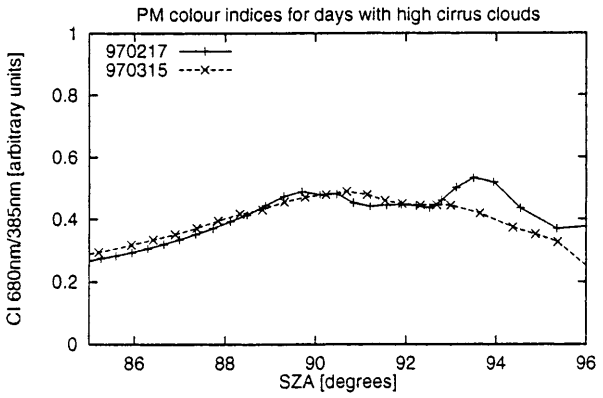

Fig. 2. Colour index development during days with high cirrus clouds

limited visual observations available, were mainly clear but with high cirrus clouds present. Between 89 and 94° SZA in this graph, some features that may be interpreted as a slight reddening occur. This is also consistent with some observations by Sarkissian *et al.* (1991). Thus, for this reason as well as for changes caused by varying ozone concentrations, small reddenings have to be considered insignificant.

2.2.4 Interpretation of the CI curves. It can be seen that the important signature of PSCs is a large positive (relative to the non-PSC cases) CI slope during twilight. This quantity is proportional to the ratio of the CI at a certain SZA (>90°) to the CI at $SZA = 90°$, a ratio that is usually called *normalized colour index*.

It can be argued that it may be important to correct the measured spectra for all known absorptions and other effects not caused by PSC scattering. This was emphasized in Sarkissian *et al.* (1991). However, our intention here is to find a simplified method suitable for use with all kinds of instrumentation, such as spectrometers, filter photometers, etc, where the column amounts of ozone and other trace species are not easily calculated.

Different features, such as impact of tropospheric clouds, distant PSCs and varying absorptions, should instead be recognized by a careful classification of CI plots. This, however, requires information on the overall meteorological and PSC situation by means of daylight all-sky imaging, visual observations, etc, which are not available at present. The development of such observations and classification methods is an aim of our future work.

2.2.5 Data availability. As was demonstrated above, it is possible to detect polar stratospheric clouds when the sun is is in a certain zenith angle interval. A reasonable assumption is to take $92° < SZA < 95°$ as a usable range. The local time of these SZA intervals – calculated for the geographical location of IRF using the graphical ephemeris software XEphem – vs date is plotted in Fig. 3. The duration of this twilight interval is on the order of 30 min. Mountain-induced PSCs develop over timescales of hours and will thus be undetectable during most of the day. Therefore the method may underestimate the occurrence of such events.

2.3 Visual observations

2.3.1 Availability of observations. Like the zenith-sky measurements, visual observations are limited by requirements on solar zenith angle and viewing angle intervals, since the distinct iridescent appearance (or deep red colour) that characterizes some stratospheric clouds (most probably ice PSCs, although PSC type I have with high certainty been observed at the site as "purple twilights") is only visible at certain scattering angles. If these conditions are not met, it is not possible to identify stratospheric clouds by monostatic observations alone, since altitude information is often required to distinguish them from high tropospheric clouds such as cirrus. However, the most severe limitation of direct visual observations is tropospheric clouds.

2.4 Lidar observations

A lidar system is operated on campaign basis at the nearby site of Esrange. The distance to the location of the UV-visible spectrometer is approximately 30 km so the two instruments are likely to observe different air masses. However, they are in the vicinity of the same gridpoint of the synoptic ECMWF model, so they can be used in order to study the importance of mesoscale deviations.

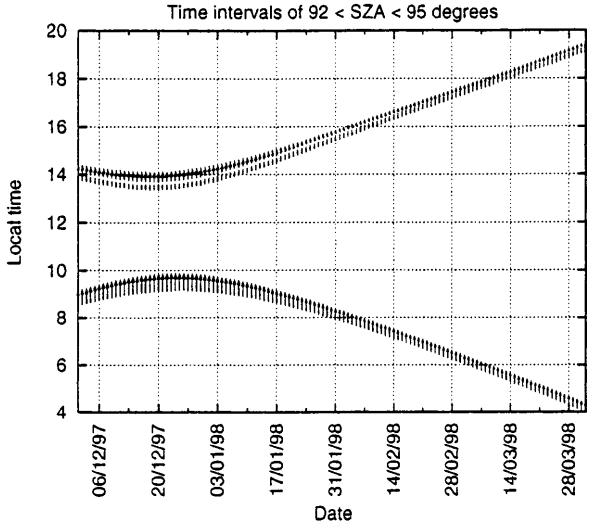

Fig. 3. Time intervals (marked by *arrows*) of 92° < SZA < 95° calculated for Kiruna (68°N, 20°E)

2.4.1 Data availability. Since the lidar is an active instrument, observations are not limited to sunrise and sunset but are most conveniently performed at nighttime. Thus we cannot expect the two instruments to measure during exactly the same events. Rather, visual, CI and lidar observations complement each other to provide a coverage of mesoscale and synoptic PSC events within the Kiruna area.

3 Experimental results

3.1 Visual observations

Records of visual PSC observations (most probably isolated PSC type II structures) were kept during the European leewave campaigns (Fricke *et al.*, 1998) in the winters of 1996–1997 and 1997–1998. During other periods visual records cannot be considered complete.

3.2 Colour indices

Colour indices according to Eq. (1) and Table 1 were evaluated for the winter seasons of 1996–1997 and 1997–1998. The ratios CI_{norm} of observed colour indices to the interpolated values at SZA = 90°, i.e.

$$\mathrm{CI}_{\mathrm{norm}} = \frac{\mathrm{CI(SZA)}}{\mathrm{CI}(90^\circ)} \tag{2}$$

were formed and averaged over the interval 93.5° < SZA < 94°, where the CI generally shows its maximum when PSCs are present, for each sunrise and sunset (Fig. 4). Figure 5 shows histograms of these values for the two winters. In Fig. 6 the days with obvious PSC presence have been removed. This suggests a PSC threshold value of $\mathrm{CI}_{\mathrm{norm}} \approx 0.8$.

3.3 Lidar observations

The lidar detects atmospheric backscatter at 532 nm in polarisations parallel and perpendicular to the emitted beam. The backscatter ratio and depolarisation depend on the size and shape of the particles. Thus the lidar is capable of distinction between PSC type I – saturated ternary solution (STS)/nitric acid tetrahydrate (NAT), and PSC type II – water ice (See Table 3).

3.4 Summary of observations

All detections of PSCs by any of the methods ($\mathrm{CI}_{\mathrm{norm}} > 0.8$, lidar or visual observation) are collected in Figs. 7 and 8. Lidar observations are divided according to polarisation – parallel only or depolarisation (signal in the cross-polarised channel). Included is also modelled synoptic incidence of PSC type I and II, respectively (see sect. 4).

The CI detections are by far more comprehensive because of the insensitivity to tropospheric clouds and

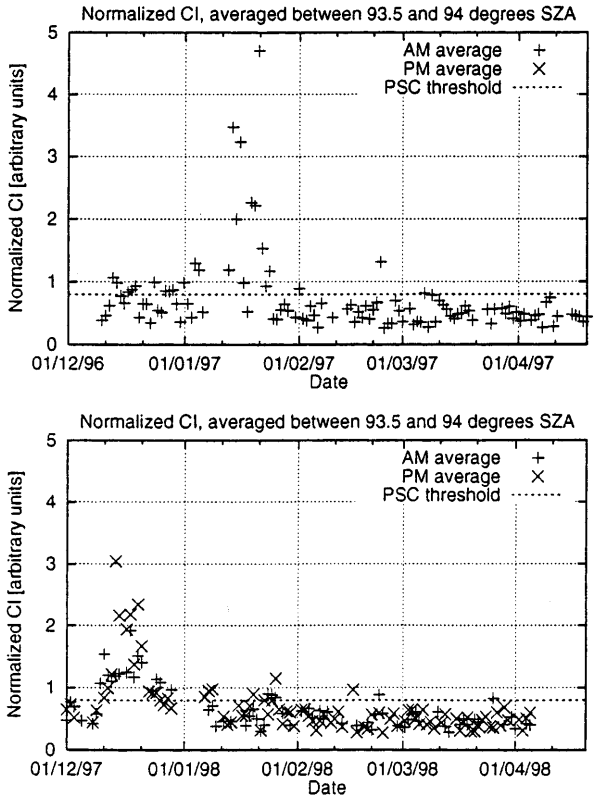

Fig. 4. Time series of colour index ratios [$\mathrm{CI}_{\mathrm{norm}} = \mathrm{CI(SZA)}/\mathrm{CI}(90^\circ)$]

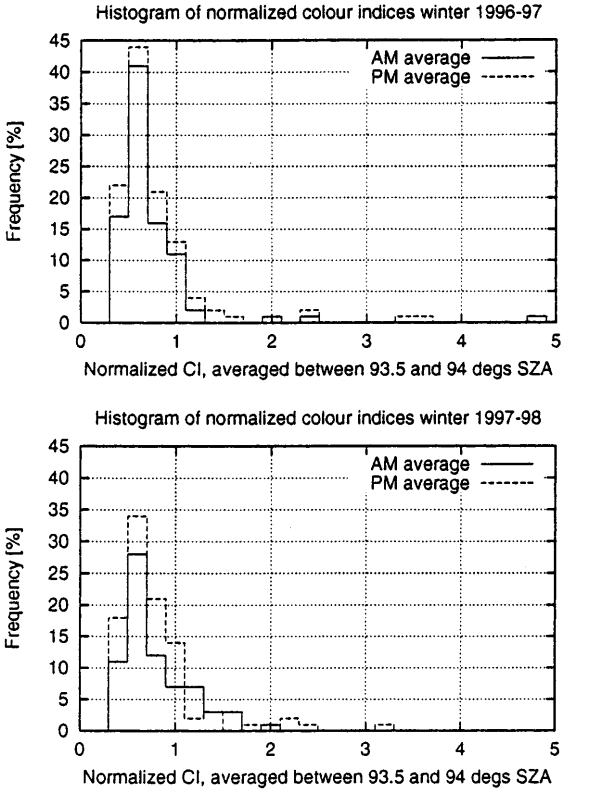

Fig. 5. Histograms of colour index ratios [$\mathrm{CI}_{\mathrm{norm}} = \mathrm{CI(SZA)}/\mathrm{CI}(90^\circ)$]

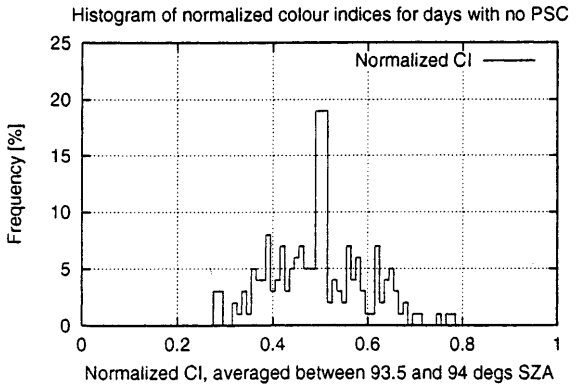

Fig. 6. Histograms of colour index ratios [$CI_{norm} = CI(SZA)/CI(90°)$]; data from days with obvious PSC observations are removed

Table 3. Interpretation of lidar data

Observation	Composition
Low backscatter ratio, parallel	STS
Low backscatter ratio, depolarisation	NAT
High backscatter ratio, depolarisation	Ice

the automation of the measurements. Missing lidar or visual observations mean either cloudy weather, no PSC detection or no observations.

From these data it can be concluded that significant CI reddenings do correspond to incidence of PSC type I or II. The largest reddenings were actually coincident with synoptic presence of PSC type II as deduced from lidar observations and calculated temperatures.

Table 4 shows the frequency of PSC presence as inferred from CI reddenings. The total numbers of twilight measurements (AM and PM) available are also included. The significantly less number of AM measurements is due to frequent power failures, network

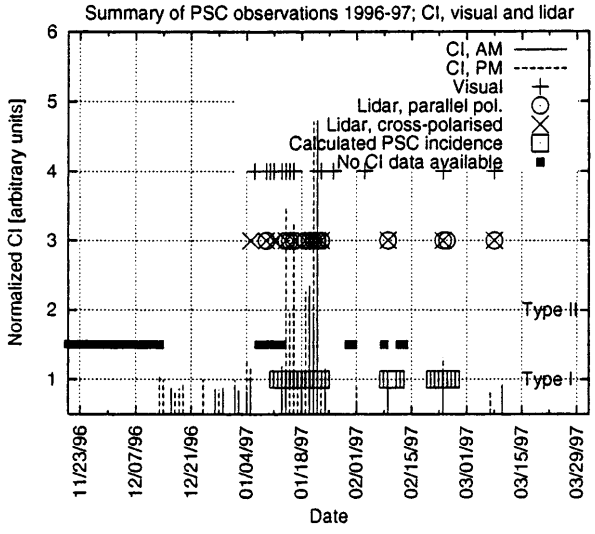

Fig. 7. Observations of PSCs in the winter of 1996–1997

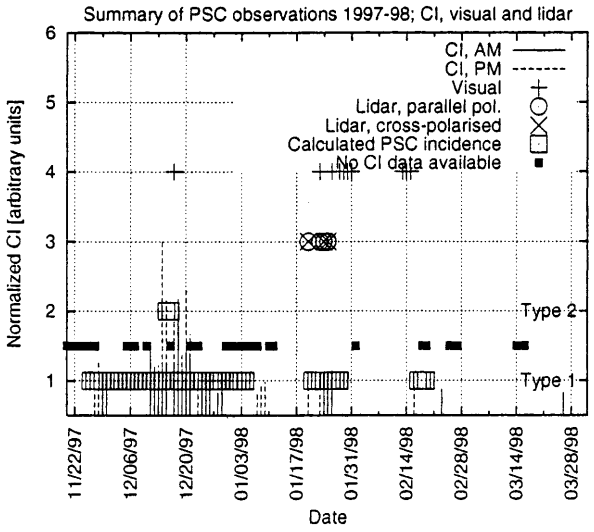

Fig. 8. Observations of PSCs in the winter of 1997–1998

shutdowns, etc., during nights. On such occasions the instrument has to be restarted manually in the morning.

4 Synoptic PSC presence

As outlined in sect. 1 the role of mesoscale PSC events (as opposed to synoptic PSC and aerosol presence) in stratospheric chemistry is still controversial. Some authors (Carslaw *et al.*, 1998) believe that such events explain the excess ozone loss that has until now not been possible to account for by chemistry/transport (CTM) models. A starting point in understanding this can be provided by comparing the above observations with synoptic models.

One-point-per-day calculations of PSC incidence on the isentropic levels 475 K, 550 K, and 675 K (as inferred from ECMWF temperatures) were retrieved using the program *isen_ts* available at NILU (Braathen *et al.*, 1998). Calculated PSC incidence on *any* of these altitudes is included in the Figs. 7 and 8.

A constant water vapour VMR of $4.6 \cdot 10^{-6}$ and a LIMS NAT profile from January 1979 are used in these calculations. However, even large changes in these parameters typically yield differences in NAT and H_2O condensation temperatures on the order of 1, K (Hanson and Mauersberger, 1988; Marti and Mauersberger 1993), whereas leewave activity easily causes temperature changes on the order of 10 K, so these assumptions introduce no major error. However, this model fails to

Table 4. Numbers of twilights with PSC incidence (out of total number of measurements) as deduced from CI reddenings for the winters of 1996–1997 and 1997–1998

	CI AM	CI PM	Total AM	Total PM
Winter 1996–1997	16	26	90	113
Winter 1997–1998	21	25	72	101
Total	37	51	162	214

Table 5. Numbers of days with modelled PSC incidence for the winters of 1996–1997 and 1997–1998

	PSC type I	PSC type II	Total days
Winter 1996–1997	20	0	132
Winter 1997–1998	45	2	135
Total	65	2	267

predict the observed synoptic PSC type II occurrences (which persisted for several days) in January 1997.

In Table 5, the total number of days with calculated PSC incidence thus obtained follows.

5 Discussion

In general there seems to be a good agreement between observed CI reddenings and calculated synoptic PSC type I occurrence. During the winter of 1996–1997 the frequency of observed CI reddenings (according to Table 4: 18% of all sunrises and 23% of all sunsets) was slightly higher than that of modelled PSC incidence (15% of all days according to Table 5). In the winter of 1997–1998 the frequency of observed PSC events was in fact lower than the frequency of calculated events but this can be explained by the fact that there are long periods of missing CI data coincident with cold periods during that winter.

What is clearly underestimated, however, by the synoptic temperature approach to PSC incidence modelling is the occurrence of PSC type II. Very large reddenings, such as the cases of January and December 1997, were coincident with visual observations of PSC type II. The model predicts mainly PSC type I on those occasions.

Except for very rare events, such as the aforementioned case of 16–19 January 1997, PSC type II are mainly observed as discrete structures developing in mountain waves. This is naturally more likely to happen if synoptic conditions allow the presence of PSC type I. It can nevertheless be concluded that both the observations (for reasons explained in sects. 2.2.3 and 2.2.5) and the modelling underestimate the occurrence of these events, but observations suggest that they are indeed more common than predicted by synoptic modelling.

6 Outlook

Future work in this field will include a comparison between stations at different locations with respect to the Scandinavian mountain range (Andøya, Norway; Kiruna, and Sodankylä, Finland) and also development of a denser network of photometers and imagers, which will improve the coverage of mesoscale PSCs. This can be expected to help resolve the question of the importance of mesoscale PSCs and will also serve as ground-truth for PSC mapping from satellites.

Acknowledgements. The authors thank their colleagues for fruitful discussions and Alain Sarkissian for comments on the method. The work was partly supported by MRI, the Environment and Space Research Institute in Kiruna. ECMWF temperature data and PSC incidence calculations were obtained from the Norwegian Institute of Air Research (NILU). Since February 1999 the colour index data are available in real time on the WWW. See http://www.irf.se/~fredrik.

Topical Editor F. Vial thanks K. Kreher and A. Sarkissian for their help in evaluating this paper.

References

Braathen, G., L. Aanesland, and B. Bojkov, NADIR News, Norwegian Institute of Air Research, 1998.

Carslaw, K. S., M. Wirth, A. Tsias, B. P. Luo, A. Dörnbrack, M. Leutbecher, H. Volkert, W. Renger, J. T. Bacmeister, E. Reimers, and T. Peter, Increased stratospheric ozone depletion due to mountain-induced atmospheric waves, *Nature*, **391,** 675–678, 1998.

Fricke, K.-H., K. P. Müller, M. Serwazi, J. Reichardt, S. Kirkwood, Å. Steen, P. Hoffman, H. Mehrtens, A. Hauchecorne, F. Fierli, U.-P. Hoppe, and G. Hansen, Wind generated polar stratospheric clouds: The case of January 16, 1997 above Northern Scandinavia, in *Polar stratospheric ozone 1997, Proceedings of the fourth European symposium 22 to 26 September 1997, Schliersee, Bavaria, Germany*, pp. 127–130, European Commission, 1998.

Garcia, O., K. Pagan, P. Foschi, S. Gaines, and S. Hipskind, Detection of polar stratospheric clouds over Antarctica using AVHRR images obtained at Palmer station during August 1992, *Polar Record.*, **177,** 211–226, 1995.

Hanson, D., and K. Mauersberger, Laboratory studies of the nitric acid trihydrate Implications for the south polar stratosphere, *Geophys. Res. Lett.*, **15,** 855–858, 1988.

Hulburt, E., Explanation of the brightness and color of the sky, particularly the twilight sky. *J. Opt. Soc. Am.*, **43,** 113–118, 1953.

Marti, J., and K. Mauersberger, A survey and new measurements of ice vapor pressure at temperatures between 170 and 250 K. *Geophys. Res. Lett.,* **20,** 363–366, 1993.

Meerkötter, R., Detection of polar stratospheric clouds with ERS-2/GOME data, *Ann. Geophys.*, **13,** 395–405, 1995.

Platt, U., Differential optical absorption spectroscopy, in *Air Monitoring by Spectroscopic Techniques, chap. 2. J Wiley*, 1994.

Rozenberg, G. V., *Twilight*, Plenum Press, New York 1966.

Sarkissian, A., J.-P. Pommereau, and F. Goutail, Identification of polar stratospheric clouds from the ground by visible spectrometry, *Geophys. Res. Lett.* **18,** 779–782, 1991.

Solomon, S., R. R. Garcia, F. S. Rowland, and D. J. Wuebbles, On the depletion of Antarctic ozone, *Nature*, **321,** 755–758, 1986.

Solomon, S., A. L. Schmeltekopf, and R. W. Sanders, On the interpretation of zenith sky absorption measurements, *J. Geophys. Res.* **7,** 8311–8319, 1987.

Paper II

Carl-Fredrik Enell, Björn Gustavsson, Åke Steen, Urban Brändström and Peter Rydesäter. **Multistatic imaging and optical modelling of nacreous clouds**. *Phys. Chem. Earth*, 25(5–6):451–457, 2000.

Pergamon

Phys. Chem. Earth, Vol. 25, No. 5–6, pp. 451–457, 2000

Multistatic imaging and optical modelling of nacreous clouds

C.-F. Enell[1], B. Gustavsson[1], A. Steen[1], U. Brändström[1], and P. Rydesäter[2]

[1]Institutet för Rymdfysik (IRF), Kiruna, Sweden
[2]Mitthögskolan, Östersund, Sweden

Received: 16 December 1999 – Accepted: 25 February 2000

Abstract. The presence of *polar stratospheric clouds* (PSC) has important implications for stratospheric chemistry. Thus it is important to understand the development of such clouds. In this report the feasibility of using multi-static imaging for studies of PSC physics is discussed. In particular, a method to solve for particle sizes using bistatic multi-wavelength observations is described. It has not yet been possible to apply the proposed method to PSC images. However, a numerical simulation for the ideal case of single scattering by spherical particles works with reasonable accuracy, even when random noise is added.

1 Introduction

During most winters, conspicuous iridescent clouds at high altitude can be observed in the polar regions. Due to their appearance they are generally called *mother-of-pearl* or *nacreous* clouds. Størmer (1930) was the first to determine the altitude of nacreous clouds by photographic triangulation. It was recognised that they are located in the stratosphere, typically at 25 kilometres. It was also concluded (Hesstvedt, 1960) that mother-of-pearl clouds consist of liquid water or ice.

Since then, several observational and theoretical studies have improved our understanding of the phenomenon. Today three subtypes (Poole and Mc Cormick, 1988; Browell et al., 1990) of *polar stratospheric cloud (PSC)*, not always visible to the eye, are defined with respect to their *lidar backscatter* properties (Tab. 1).

The reaction rates of such processes as chlorine activation and denitrification are considerably higher in the heterogeneous case (i.e. on particle surfaces) than in pure gas phase. Therefore the presence of stratospheric clouds causes increased stratospheric ozone depletion (Solomon et al., 1986).

Correspondence to: Carl-Fredrik Enell

Type	Backscatter	Depolarisation	Probable composition
I_a	Weak	Strong	$HNO_3 \cdot 3H_2O$ (**N**itric **A**cid **T**rihydrate)
I_b	Strong	Weak	**S**upercooled **T**ernary **S**olution of H_2SO_4, HNO_3, H_2O
II	Strong	Strong	H_2O

Table 1. Classification of stratospheric NAT, STS, and water clouds.

2 Development of stratospheric clouds

In the Antarctic, stratospheric clouds may exist on a synoptic scale during long times due to the low temperatures possible in the undisturbed southern polar vortex. This explains the well-known fact that substantial chemical ozone depletion is observed.

In the Arctic, however, the polar vortex is orographically distorted and consequently synoptic temperatures reach the low values required for PSC condensation less frequently. PSC formation in the Arctic is often a consequence of local cooling in mountain-induced waves. Such *mesoscale events* may also lead to considerable chlorine activation (Carslaw et al., 1998).

One possible consequence of this fact is that models of atmospheric chemistry, which infer PSC presence from synoptic temperature fields only, may be inaccurate. Thus, mesoscale processes have recently attracted much interest (see e.g. Carslaw and Amanatidis (1999)) and it is important to identify the actual presence and subsequently follow the development of PSC.

3 Properties of stratospheric clouds

3.1 Iridescence

Nacreous clouds are recognized by their iridescence, i.e. visually distinct colour pattern. The photo in Fig. 1 was taken on January 16, 1997, a day of low synoptic temperature and

strong leewave activity. Because of the relatively higher availability of records of visual sightings of nacreous clouds in comparison with other data, it is important to understand how representative such observations are of PSC occurrence in general.

Fig. 1. Stratospheric clouds above Kiruna on January 16, 1997. Photo by the author.

The principal requirement for the iridescent colour phenomena to appear is that the observation is made from a certain viewing angle. This implies that they are seen mainly during twilight. As the sun reaches higher elevations the same clouds may show a faint whitish visual appearance. Therefore the darkest winter months (December-February) is the best time for observations, not only because of the high probability of PSC presence but also since a constant twilight persists for several hours per day at the latitude of Kiruna.

There are also microphysical requirements for the PSC to appear as nacreous/mother-of-pearl clouds. There is no general agreement on the phase and shape of particles in nacreous clouds, although it is often stated that nacreous clouds are water PSC.

However, from visual observations it seems evident that the perceived colour pattern is *fixed with respect to the cloud* and does not change as consistently with the position of the observer as that of a rainbow or halo. Thus, we will henceforth assume that the idea of refraction in large ice crystals or liquid drops can be ruled out and that resonant scattering of light by particles of varying sizes is the cause of the colour pattern. In this case the particle size must not exceed a few wavelengths of visible light, i.e. a few micrometres.

Since the wavelength dependence of the scattering process must be preserved, it is also required that the cloud be sufficiently optically thin (to avoid significant multiple scattering) and that the particle size distribution be fairly monodispersive, i.e. each observed cloud volume must contain only particles in a very narrow size range. A narrow particle size distribution is likely to be obtained at the rapid cooling rates typical for strong leewave events, a result that was obtained already in the calculations by Hesstvedt (1960) for homogeneous water condensation and freezing. The same is likely to apply for droplets of a ternary $H_2SO_4 : HNO_3 : H_2O$ solution which may be a more realistic case (Tabazadeh et al., 1997).

3.2 Particle phase

It was concluded in the previous section (3.1) that two distinct types of particles are likely to be the constituents of mother-of-pearl clouds:

1. spherical droplets
2. small ($r \approx \lambda$) non-spherical particles

The latter case may result in a smoother angular variation of the intensity of scattered light than that of spherical particles (Schulz et al., 1998) and may therefore be more realistic. The following sections will deal with retrieval of particle sizes in a model case only; thus spherical particles will be assumed. This may in fact be a numerical "worst case" because of the resulting rapid angular variation of scattered intensity.

However, there is no conceptual difference in using e.g. T-matrix calculations (Mishchenko, 1991) for non-spherical particles of random or fixed orientation instead.

4 Experimental detection of PSC

Several optical remote-sensing techniques can be applied for detecting PSC presence from the ground (Enell et al., 1999) or from satellites (Poole and Pitts, 1994; Meerktter, 1995). The methods described in these references are inherently, due to scale, geometry and other properties, such that mainly qualitative information on PSC presence (PSC/no PSC) is obtained. By ground- or aircraft-based LIDAR as well as balloon-borne (in-situ) particle samplers, microphysical properties can be studied. These instruments are limited to sampling at one point or along one line at a time.

However, leewave-generated nacreous clouds show intricate structures. This is true both on the mesoscale proper (i.e. with respect to the location of the clouds) as well as on the *microscale* of a single cloud. Such details are most easily studied by imaging techniques.

5 Multistatic imaging of PSC

The imaging system ALIS (Steen and Brändström, 1993), at present consisting of six remote-controlled stations with high-performance CCD cameras, is usable for this purpose. The location (Fig. 2) close to the Scandinavian mountain range implies that mountain-wave PSC (Sect. 2) are frequently observed in the area. The locations of these stations are optimised for studies of the aurora, which is located at altitudes of 100 kilometres and above. Therefore an additional mobile station platform is available, where one of the cameras may be installed if desired.

When PSCs are present between two ALIS stations, the system thus allows imaging of the clouds in forward- and back-scattering geometry. Thus the altitude of the clouds can

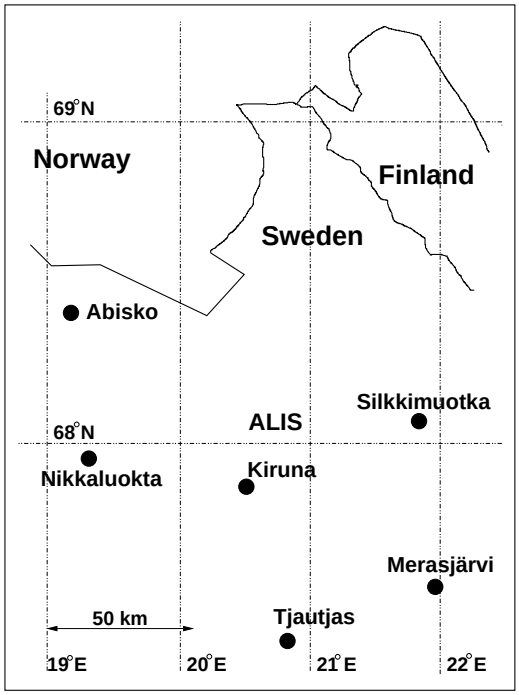

Fig. 2. The ALIS multistatic imaging system: locations of the 6 existing stations.

be determined by triangulation (Steen et al., 1998) with any time resolution down to ≈ 30 seconds as limited by the CCD readout time. The light-scattering properties of a PSC may also be used for determination of its microphysical structure, which was realised early on. An attempt was commented on by Hesstvedt (1960) although no reliable results were obtained, probably due to technical limitations.

The ALIS cameras, however, allow multispectral imaging by means of a filter wheel with up to five narrow-band interference filters and an empty position (white light). Bi- or multi-static imaging in well-defined wavelength regions can therefore be performed also for the purpose of PSC particle characterisation.

Filter position	Center wavelength [Å]	FWHM [Å]
0	5590	40
1	6310	40
2	6230*	40
3	open	–
4	8455*	40
5	4285	40

Table 2. The standard filter configuration for an ALIS camera. Filters marked with an asterisk may differ but the 4285, 5590, and 6310 Å filters (adapted for auroral emissions) are available in all cameras.

6 Methods in multistatic PSC observations

6.1 Position calibration

As already stated above, the main reason for multi-static imaging of an object is the possibility to track its position and temporal development. Conversely, the position of a known point in the imaged volume can be projected into the images, so that corresponding pixels in the images from multiple stations can be identified.

For this purpose the pointing directions and optical characteristics of the cameras must be known accurately. This is accomplished by means of star calibration in such a way that the line of sight of each pixel is known with an accuracy of 0.01°.

6.2 Calculation of light scattering properties

In the following an intensity phase function $P(x,\theta)$ will be assumed, defined such that

$$I_s(\theta,\lambda) = P(x,\theta) I_0(\lambda) \tag{1}$$

$$x = \frac{2\pi\rho}{\lambda} \tag{2}$$

Fig. 3 shows the geometry of the problem and necessary definitions. Only the ratio of the wavelength λ to the particle radius ρ is of importance, but for practical reasons we may instead write

$$P = P(\theta,\rho,\lambda) \tag{3}$$

where $I_s(\theta,\lambda)$ is the spectral intensity at a wavelength λ of light scattered at an angle θ and I_0 is the spectral intensity of the incident light. Considering the variation of refractive index with wavelength, the notation (3) is in fact formally the more correct one.

This notation also implies that polarisation effects are neglected. Since the present cameras have no polarisers, with which polarisation effects can be measured, it has to be assumed here that they are insensitive to polarisation. This should be confirmed experimentally when possible. The incident light should also be unpolarised, which is reasonable for direct sunlight. The intensity phase function can in this case be calculated as the sum of the squared amplitudes of the perpendicularly polarised scattered components.

Equations (1)–(3) suggest that a retrieval of the particle radius ρ is possible if P can be determined for known wavelengths and angles, and this will be shown in the following. The incident spectral intensity $I_0(\lambda)$ is in general unknown or at least difficult to calculate. However, since multispectral, multistatic data (geometry as in Fig. 3) is used, it is possible to work with *intensity ratios* only.

We have

$$I_s(\theta_1,\lambda_1) = I_0(\lambda_1) P(\theta_1,\rho,\lambda_1) \tag{4}$$

$$I_s(\theta_1,\lambda_2) = I_0(\lambda_2) P(\theta_1,\rho,\lambda_2) \tag{5}$$

$$I_s(\theta_2,\lambda_1) = I_0(\lambda_1) P(\theta_2,\rho,\lambda_1) \tag{6}$$

$$I_s(\theta_2,\lambda_2) = I_0(\lambda_2) P(\theta_2,\rho,\lambda_2) \tag{7}$$

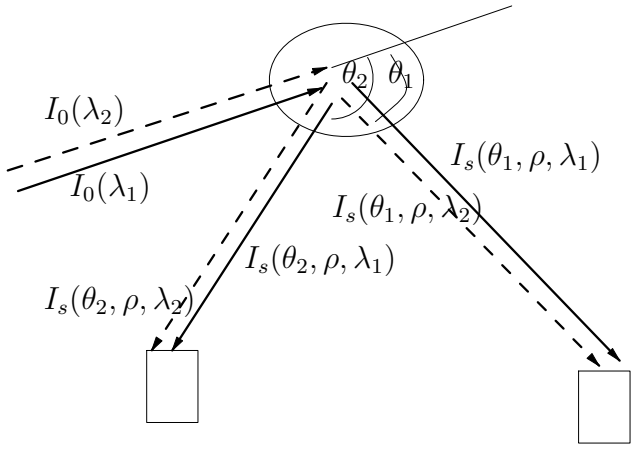

Fig. 3. The geometry of bistatic observation of scattered light.

Taking the relative ratio

$$C(\theta_1, \theta_2, \lambda_1, \lambda_2, \rho) = \frac{I_s(\theta_1, \rho, \lambda_1)/I_s(\theta_1, \rho, \lambda_2)}{I_s(\theta_2, \rho, \lambda_1)/I_s(\theta_2, \rho, \lambda_2)} \quad (8)$$

the unknown quantities I_0, as well as the $\frac{1}{r^2}$ falloff in scattered intensity obtained when imaging a point source from a distance r, cancel out. This yields

$$C(\theta_1, \theta_2, \lambda_1, \lambda_2, \rho) = \frac{P(\theta_1, \rho, \lambda_1)P(\theta_2, \rho, \lambda_2)}{P(\theta_1, \rho, \lambda_2)P(\theta_2, \rho, \lambda_1)} \quad (9)$$

which can be determined experimentally *from the images* if extinction in the atmosphere is negligible, and calculated theoretically as a function (look-up table) of ρ, θ_1 and θ_2 for fixed wavelengths (Fig. 4). The Mie code by Bohren and Huffman (1983) was used together with a calculation routine for the refractive index of liquid water[1].

6.3 Particle size retrieval method

Working with the relative ratios defined above, we propose the following algorithm for particle size retrieval.

1. Calculate the ratios between pixel values for L wavelengths (as many as technically possible) for each station.
2. Calculate the quantities C according to Eq. (8) using the pixel ratios thus obtained for two stations. This yields $N = \binom{L}{2}$ values $\tilde{C}_n, n = 1..N$ for each pixel.
3. Calculate (extract from a look-up table) the theoretical phase function ratios C_{nm} for the two scattering angles determined by the location of the two stations, the position of the observed PSC volume, and the solar zenith and azimuth angles. The subscript n, as above, refers to the wavelength combination, and $m = 1..M$ to the discrete radii ρ_m for which C is calculated.
4. Find all points $\rho_{nk}, k \leq m$ of intersection between $\tilde{C}_n$ and C_{nm}.
5. The best solution ρ_B is found by the minimisation

$$\min_{\rho_B} \sum_{n=1}^{N} \min_{k} |\rho_B - \rho_{nk}| \quad (10)$$

   i.e. the radius that most closely fits the nearest intersection points.
6. Repeat the procedure for each pixel of interest.

Figure 5 gives a graphical outline of this scheme. A known radius of 1.5 micrometers, four wavelengths, and two arbitrary scattering angles have been assumed. In the upper panel C and lines of the constant values of $\tilde{C}_n$ corresponding to this radius are shown. The lower panel shows the positions of all corresponding intersections $\rho_{nk},\ n = 1..6$. In this ideal example it is easily seen that the input radius is the one that matches the intersections most closely for all n.

7 Numerical feasibility test

The amount of useful experimental data is still limited to the case of January 16, 1997. Due to the structure of these PSCs, with large overlapping clouds, this case is not suitable for a first test of the particle size retrieval. Furthermore, the star calibration (Sect. 6.1) image for this case is of poor quality, so a sufficiently accurate positioning is impossible. For these reasons we developed the following simple numerical test scheme for the method.

1. Assume a simple monodispersive particle size distribution, e.g. a Gaussian $\rho(x_k) = \rho_{max} exp[(\frac{x_k - x_0}{b})^2]$, where x_0 and b are arbitrary parameters and x_k is the position along the cloud in a suitable direction.
2. Assume that each point can be observed from two arbitrary scattering angles θ_1 and θ_2.
3. Calculate $C(x_k) = C(\theta_1, \theta_2, \lambda_1, \lambda_2, \rho(x_k))$ for each possible independent pair of filter wavelengths λ_1 and λ_2 (Tab. 2) in the same way as in Fig. 5.
4. Add random noise to $C(x_k)$. This represents $\tilde{C}_{nk}$ for each thought pixel k.
5. Run the retrieval procedure outlined in Sect. 6.3.

This scheme was applied for the test case $\rho_{max} = 3\mu m$ and $x_k = k, k = 1..100, x_0 = 50, b = 40$ (arbitrary positions) with the following result (Fig. 6). As above, Mie calculations for the wavelengths of 4285, 5590, 6310, and 8455 Å were used. The first and second best fits (Eq. (10) were retained.

It can be seen that the main part of the retrieved results fit the input curve well, but in addition there are many spurious solutions. Thus, smoothness of the distribution of radii has to be assumed to filter out such solutions.

[1] Available at `http://atol.ucsd.edu/%7Epflatau/refrtab/`

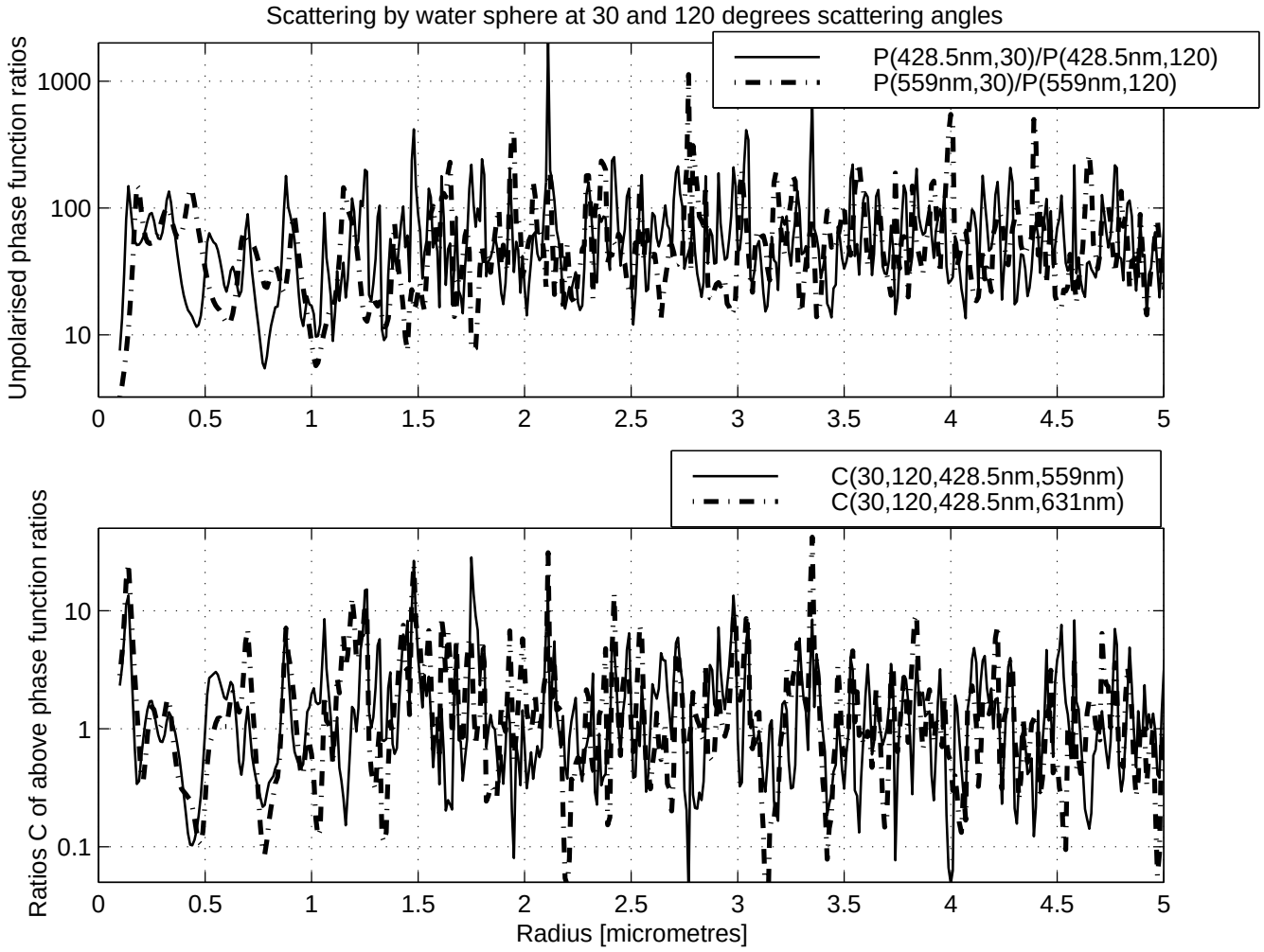

Fig. 4. Phase function ratios calculated using the Mie code by Bohren and Huffman (1983)- example for two possible pairs of ALIS filter wavelengths.

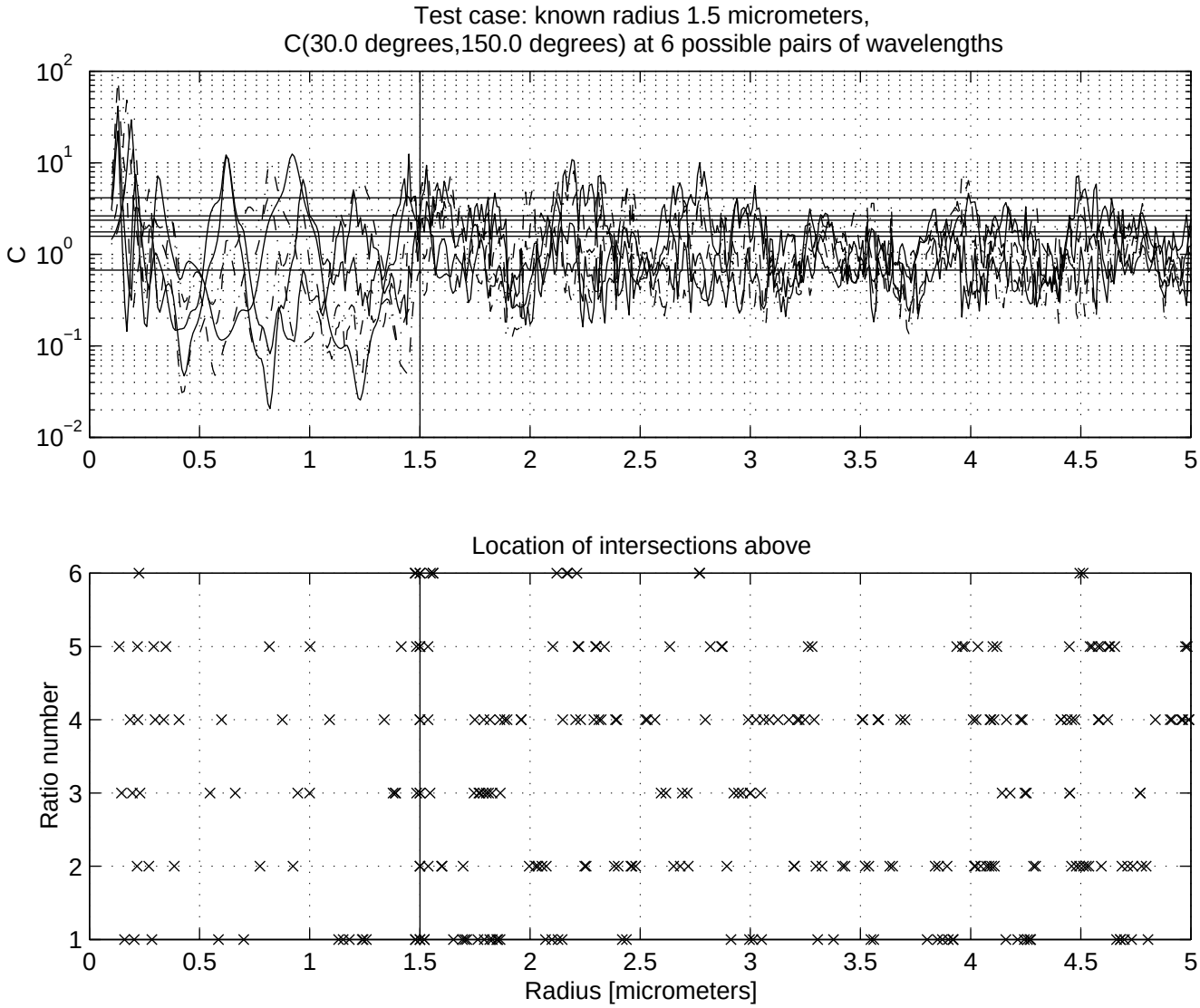

Fig. 5. The basic idea of particle size retrieval: Finding the radius of best matching intersections between experimentally determined and theoretically calculated phase function ratios. Due to the difficulty in separating the curves in the upper plot, the radial coordinates of the intersections are presented in the lower plot together with the known solution.

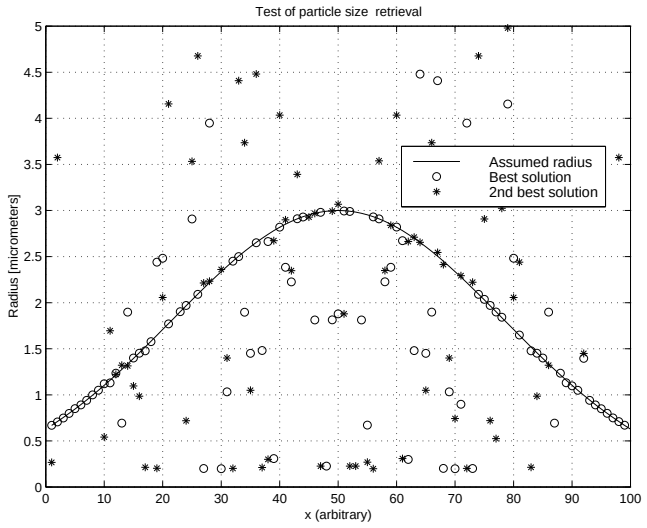

Fig. 6. Results of the test run for the case $r = 3exp[(\frac{x-50}{40})^2], x = 1..100$

8 Discussion

The results above indicate that the particle size retrieval procedure has passed a crucial first step. One major complication can be foreseen, namely that light scattered not only from the cloud particles but from the entire atmospheric column is observed. Thus the images must be corrected (background-filtered), assuming that the atmospheric background varies smoothly. The effect is minimised further by restricting the measurements to twilight only (which, as was stated above, is the prevalent condition during the subarctic winter).

It thus still remains to be proven that the method is practically applicable. It is expected that experimental validation will take place during the SOLVE/EuroSOLVE campaign in the winter of 1999–2000. If the outcome is positive, the availability of this method will be of advantage in understanding the properties of PSC. One important issue might be the distinction between the concept of mother-of-pearl and other types of PSC, i.e. understanding how representative mother-of-pearl cloud displays are for PSC incidence in general, and the results will also be of interest for modellers of atmospheric chemistry and radiative transfer.

Acknowledgements. The work of the main author is mainly financed by the Environment and Space Research Institute (Miljö- och Rymdforskningsinstitutet, MRI) in Kiruna.

References

Bohren, C. F. and Huffman, D. R., *Absorption and scattering of light by small particles*, John Wiley & Sons, Inc., 1983.

Browell, E. V., Butler, C. F., Ismail, S., Robinette, P. A., F., C. A., Higdon, N. S., Toon, O. B., Schoeberl, M. R., and Tuck, A. F., Airborne lidar observations in the wintertime arctic stratosphere: Polar stratospheric clouds, *Geophysical Research letters*, *17*, 385–388, 1990.

Carslaw, K. S. and Amanatidis, G. T., eds., *Air pollution research report 69: Mesoscale processes in the stratosphere - Proceedings of the European workshop*, European commission, DG XII, Office for official publications of the European Communities, iSBN 92-828-4629-6, 1999.

Carslaw, K. S., Wirth, M., Tsias, A., Luo, B. P., Dörnbrack, A., Leutbecher, M., Volkert, H., Renger, W., Bacmeister, J. T., Reimers, E., and Peter, T., Increased stratospheric ozone depletion due to mountain-induced atmospheric waves, *Nature*, *391*, 675–678, 1998.

Enell, C.-F., Steen, Å., Wagner, T., Friess, U., Pfeilsticker, K., Platt, U., and Fricke, K.-H., Occurrence of polar stratospheric clouds at Kiruna, *AGP*, *17*, 1457–1462, 1999.

Hesstvedt, E., On the physics of mother of pearl clouds, *GP*, *21*, 1960.

Meerktter, R., Detection of polar stratospheric clouds with ERS-2/GOME data, *AGP*, *13*, 395–405, 1995.

Mishchenko, M. I., Light scattering by randomly oriented axially symmetric particles, *JOSA A*, *8*, 871–882, 1991.

Poole, L. R. and Mc Cormick, M. P., Airborne lidar observations of Arctic polar stratospheric clouds: Indications of two distinct growth stages, *Geophysical Research letters*, *15*, 21–23, 1988.

Poole, L. R. and Pitts, M. C., Polar stratospheric cloud climatology based on Stratospheric Aerosol Measurement II observations from 1978 to 1989, *JGR*, *99*, 13 083–13 089, 1994.

Schulz, F. M., Stamnes, K., and Stamnes, J. J., Modeling the radiative transfer properties of media containing particles of moderately and highly elongated shape, *GRL*, *25*, 4481–4484, 1998.

Solomon, S., Garcia, R. R., Rowland, F. S., and Wuebbles, D. J., On the depletion of Antarctic ozone, *Nature*, *321*, 755–758, 1986.

Steen, Å. and Brändström, U., ALIS - a multi-station ground-based imaging system at high latitudes, *STEP International Newsletter*, 1993.

Steen, Å., Gustavsson, B., and Brändström, U., Temporal variation of 2-D altitude distribution of lee-wave generated polar stratospheric clouds, in *Polar stratospheric ozone 1997, Proceedings of the fourth European symposium 22 to 26 September 1997, Schliersee, Bavaria, Germany*, European Commission, 1998.

Størmer, C., Photogrammetrische Bestimmung der Höhe von irisierenden Wolken, *GP*, *5*, 1930.

Tabazadeh, A., Toon, O. B., and Jensen, E. J., Formation and implications of ice particle nucleation in the stratosphere, *GRL*, *24*, 2007–2010, 1997.

Paper III

Carl-Fredrik Enell, Kerstin Stebel, Thomas Wagner, Udo Frieß, Klaus Pfeilsticker and Ulrich Platt. **Detecting polar stratospheric clouds with zenith-looking photometers**. *Sodankylä Geophysical Publication Series*, 2002. In press.

Proc. of Atmospheric Studies by Optical Methods (2002) :1–5

Detecting polar stratospheric clouds with zenith-looking photometers

C.-F. Enell[1], **K. Stebel**[1], **T. Wagner**[2], **U. Frieß**[2], **K. Pfeilsticker**[2], **and U. Platt**[2]

[1]Swedish Institute of Space Physics, Kiruna, Sweden
[2]Institute of Environmental Physics, Heidelberg University, Germany

Received: x.x.2002 – Revised: x.x.2002 – Accepted: x.x.2002

Abstract. It has been suggested to use the zenith-sky colour index (CI) as a means of obtaining an indication of the presence of polar stratospheric clouds (PSCs). This article discusses the use of the CI method for statistical purposes. Comparing CI data from a UV/visible spectrometer system (located at Kiruna, Sweden) with assimilated synoptic-scale temperature data, we conclude that the CI method yields a lower limit of PSC presence during sunrise and sunset. It is likely that tropospheric cloud presence at the tangent point of zenith-scattered solar rays is one reason for this discrepancy.

1 Introduction

Polar stratospheric clouds (Størmer, 1930; Hesstvedt, 1960; Poole et al., 1988), commonly abbreviated PSCs, develop in the cold winter polar vortex. In the Arctic this is often a result of local cooling in mountain-induced waves (see e.g. Dörnbrack et al., 2000, and references therein). Both the large-scale temperature fields and the local wave activity have a large interannual variability. This also holds true for PSC presence because of the strong temperature dependence of the involved condensation and freezing processes (Hanson and Mauersberger, 1988). It is now generally accepted that the presence of PSCs is of major importance for stratospheric chemistry, since reactions on PSC particles release active halogen species, as was recognised by Crutzen and Arnold (1986). The removal of PSC particles by sedimentation also denitrifies the polar stratosphere, which further enhances ozone depletion. See e.g. Gao et al. (2001) for recent observations of denitrification in the Arctic.

Since the wavelength dependence of the scattering cross sections of typical aerosols is a function of the Mie (Bohren and Huffman, 1983) size parameter $x = 2\pi r/\lambda$, rather than a quantity of $O(\lambda^{-4})$ as for molecular dipole scattering, an aerosol layer above the site of measurement will cause a redshift of the zenith-sky spectral radiance during twilight (Rozenberg, 1966). This is used in the context of PSC detection by Sarkissian et al. (1991, 1994, 1998); Enell et al. (1999) and in the present work.

Correspondence to: C.-F. Enell

2 Data analysis

A UV/visible spectrometer system has been in operation in Kiruna since December 1996. The system records spectra continuously during daylight and twilight. Its primary purpose is the retrieval of column densities of BrO (Sinnhuber et al., 2002), OClO, ozone and NO_2 by means of Differential Optical Absorption Spectroscopy (DOAS) analysis (Platt, 1994) in selected wavelength windows. In DOAS only absorption cross sections varying rapidly with respect to the wavelength range are considered and the broad-band spectral distribution is disregarded. The latter, however, is determined by aerosol scattering as well as the spectral sensitivity of the instrument, etc.

The simplest measure of changes due to varying broad-band scattering phenomena is the colour index

$$CI(SZA) = \frac{I(\lambda_1, SZA)}{I(\lambda_2, SZA)}$$

where $I(\lambda_1, SZA)$ and $I(\lambda_2, SZA)$ are the integrated spectral counts at the solar zenith angle SZA in wavelength intervals at the ends of the spectral interval covered by the detector. These should preferrably be chosen outside rapidly varying absorption bands, or varying trace gas concentrations along the optical path (Hulburt, 1953) will affect the colour index. Choosing $\lambda_1 > \lambda_2$, a redshift of the spectral radiance will correspond to a colour index increase. Since the colour index is a relative quantity, no absolute calibration of the detector is needed. The required processing of the spectra is subtraction of the offset voltages and dark currents of the detector photodiodes, and wavelength calibration. Detector offset and dark current are recorded every night and subtracted from the raw data. An accurate wavelength calibration for each spectrum is obtained from the positions of

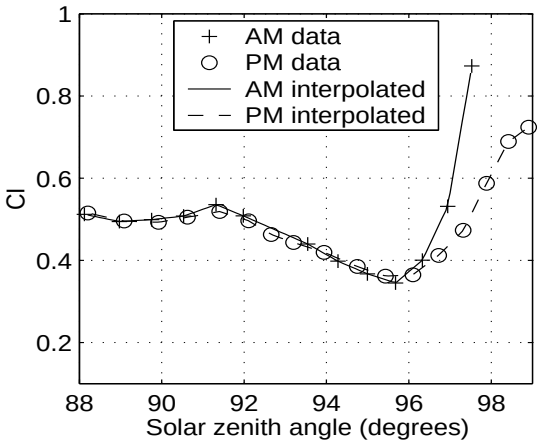

Fig. 1. CI development during sunrise (AM) and sunset (PM) on April 18, 2001, a clear day without PSCs. The AM and PM curves follow each other due to the absence of clouds.

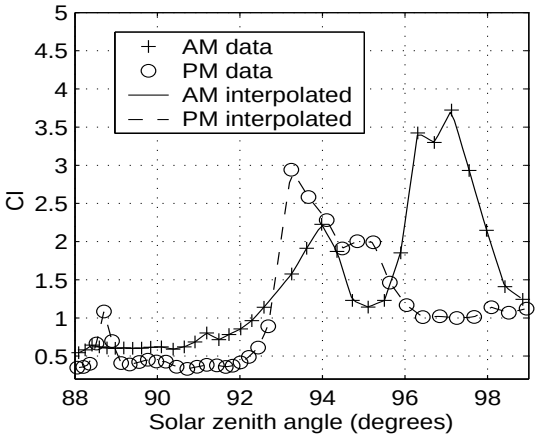

Fig. 2. CI peaks on January 25, 2000, a day with PSCs over Kiruna. The peaks around 94 degrees are due to the presence of PSCs. The peak at a SZA of 97 degrees is very likely due to local light sources; the contribution from single zenith scattering is negligible at this SZA. Note that the CI scale is 5× that of Figure 1.

the solar Fraunhofer lines (Ingelstam et al., 1988). This is a minor correction; Hg and Ne lamp spectra indicate that the spectrometer has been stable to within one channel between calibrations.

All results below have been retrieved using wavelength intervals of ± 2 nm around 680 nm (λ_1) and 385 nm (λ_2). The reason for this choice is that these wavelengths are at the ends of the interval covered by the spectrometer and outside ozone absorption bands. Nominal integration times during twilight are 5 minutes for $90° < \text{SZA} < 93°$ and 10 minutes for SZA $> 93°$. The instrument adjusts these integration times automatically to reach a detector saturation of 60–90%. The solar zenith angle SZA is calculated at the average time of spectral integration.

3 CI observations

The development of CI during sunrise (AM) and sunset (PM) on a clear day without PSCs (April 18, 2001) is shown in Figure 1. A decrease of the clear-sky CI (blueshift) after sunset, due to multiple scattering (Ougolnikov, 1999, and private communication) and possibly extinction by ozone and aerosols, can be seen in the interval $91° < \text{SZA} < 96°$. Figure 2 shows an example of the twilight CI development on January 25, 2000, when clearly visible PSCs (mother-of-pearl clouds) were observed over Kiruna. Our data series suggests that the most significant signature of PSC presence is a peak (significant redshift) close to SZA = $94°$, which is consistent with an altitude of maximal scattering probability (Solomon et al., 1987) above 20 km, i.e. typical PSC altitudes. Another feature apparent in Figure 2 is a CI increase at high solar zenith angles (above $96°$) which can sometimes be observed due to detector noise or local light sources dominating over the zenith-scattered solar light. In the raw spectra of these occasions the 546 nm green Hg line is generally a dominant feature. This is, however, no serious limitation to PSC detectability, since there is little or no single-scattering contribution to the zenith radiance from PSC altitudes (See Table 1) at these SZAs.

4 PSC detectability

4.1 PSC detection thresholds

Because of the rapidly changing solar zenith angle during twilight and the long integration times, there are typically few data points in the interval around 94 degrees. The colour index variation often also shows a large fluctuating component due to changing cloudiness (see Section 4.2), precipitation, local light sources, etc. Here we examine three different indicators of PSC-induced redshift of the zenith sky:
(A) the absolute value of the CI interpolated at SZA = $94°$,
(B) the normalised colour index (Sarkissian et al., 1991; Enell et al., 1999), i.e. the ratio of the colour index to its value at sunrise/sunset (SZA = $90°$), and (C), identification of peaks around SZA = $94°$ by a polynomial fit. The parabola

$$P(X) = CI(94°) - AX, X = (SZA - 94)^2$$

fits the data best in the least-squares sense when

$$A = \frac{CI(94°)\sum_n X_n - \sum_n CI_n X_n}{\sum_n X_n^2}$$

where the summations are over the available data points during twilight.

These three CI measures have been calculated for data from January–March and November–December of 1997,1998 and 1999 and January–March 2000. (As in Enell et al. (1999), it must be remarked that there are data gaps during the coldest winter weeks, coincident with the Christmas holidays when instrument maintenance is sparse.) In Figure 3 the results are compared with the assimilated synoptic temperatures obtained from the European Centre for Medium-Range Weather

Forecasts (ECMWF). The different CI measures are plotted versus the coldest temperature with respect to the condensation temperature of nitric acid trihydrate (T_{NAT}) occurring on the levels 400K, 475K, 550K and 675K above Kiruna in the $2.5° \times 2.5°$ ECMWF grid. T_{NAT} was calculated for each level according to Hanson and Mauersberger (1988), with 4.6 ppm H_2O and a HNO_3 profile from the Limb IR Monitor of the Stratosphere (LIMS).

The largest number of significant CI reddenings are obtained at low synoptic temperatures. The highest values are from January 1997, when a visible layer of mother-of-pearl clouds persisted for several days. A high value at T-$T_{NAT} \approx 8$ is present in the absolute and normalised colour index series but absent in the polynomial fit. This point was found to be the result of the entrance lenses accidentally being covered after a system restart. A basic requirement on all detection methods is the capability to filter out such outlier values. The peak coefficient A can be thought of as a filtered index calculated from all available data points in the twilight SZA interval. Due to this filtering, A is large only for $T < T_{NAT}$. We therefore consider the peak fit to provide the best threshold condition out of these methods. Sarkissian et al. (1991) argued that normalisation of the CI to unity at SZA = $90°$ would correct for effects unrelated to stratospheric scattering. A comparison (Fig. 4) between the three indices for the entire available dataset (winter months from December 1996 until March 2002) shows that the opposite effect can occur. Division by a value (CI at SZA = $90°$) which has a large contribution from direct tropospheric scattering, or even has to be extrapolated during the polar winter when the sun is below the horizon, introduces unnecessary noise. The absolute value of the CI shows less scatter than the normalised CI, which is sometimes even negative due to the extrapolation error.

A striking result is that a large number of low CI values are obtained at all synoptic temperatures. PSC observations at temperatures above synoptic T_{NAT} could be expected since local temperatures are affected by mountain wave induced cooling. This even includes non-equilibrium effects, causing unexpected presence of liquid or solid PSCs (Voigt et al., 2000; Tsias et al., 1997). The result may indicate that detectable PSCs develop only as a consequence of supercooling below T_{NAT}. The possibility that the abscissae of Figure 3 should be shifted up to 5K due to systematic biases in the meteorological model is also non-negligible (Manney et al., 2001). Calibration against other observations and further radiative transfer modelling is required to determine the sensitivity. However, because of the observational geometry, the interpretation that the PSC presence is underestimated is also plausible.

4.2 Geometrical and meteorological constraints

As demonstrated e.g. by Ougolnikov (1999), a major contribution to the brightness of the twilight sky emanates from multiple scattering. However, enhanced scattering by PSCs will occur as single-volume scattering within the field of view

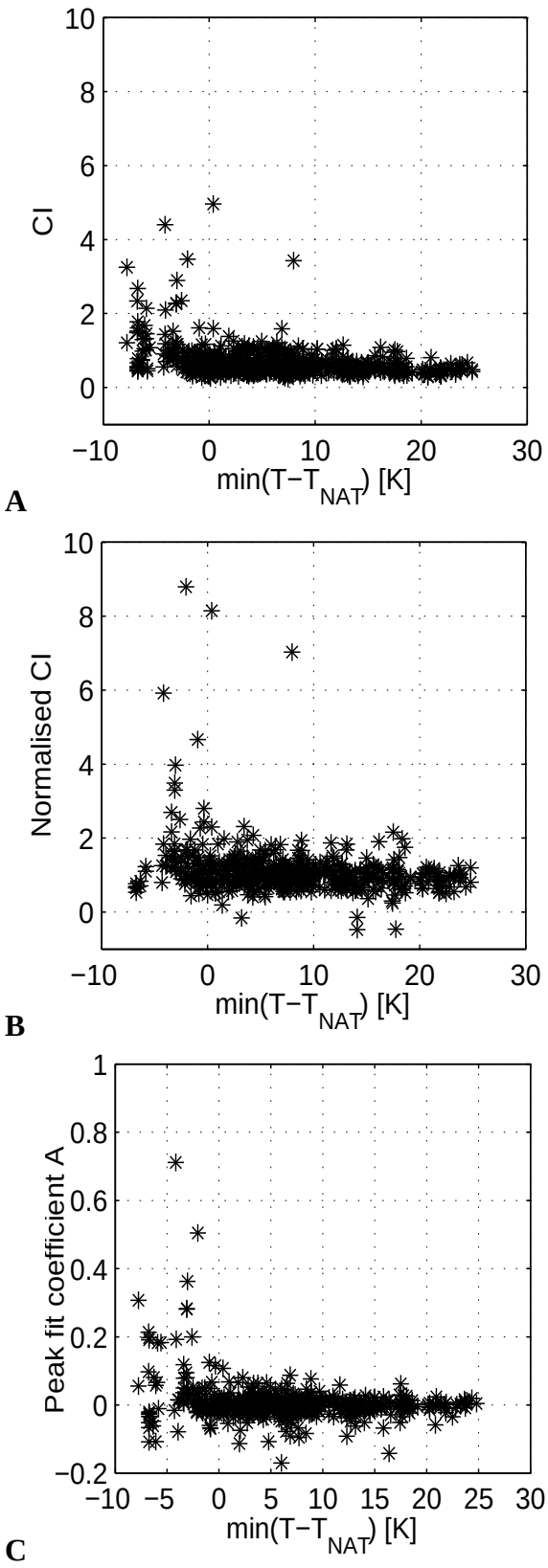

Fig. 3. Scatter plots of colour indices vs. the minimum of T-T_{NAT} on any of the ECMWF levels 400K, 475K, 550K and 675K. A: Absolute value of CI at SZA = $94°$. B:Normalised CI. Unphysical values close to zero have been removed. Negative values are kept to show the influence of interpolation errors. C: Polynomial coeffi cient A.

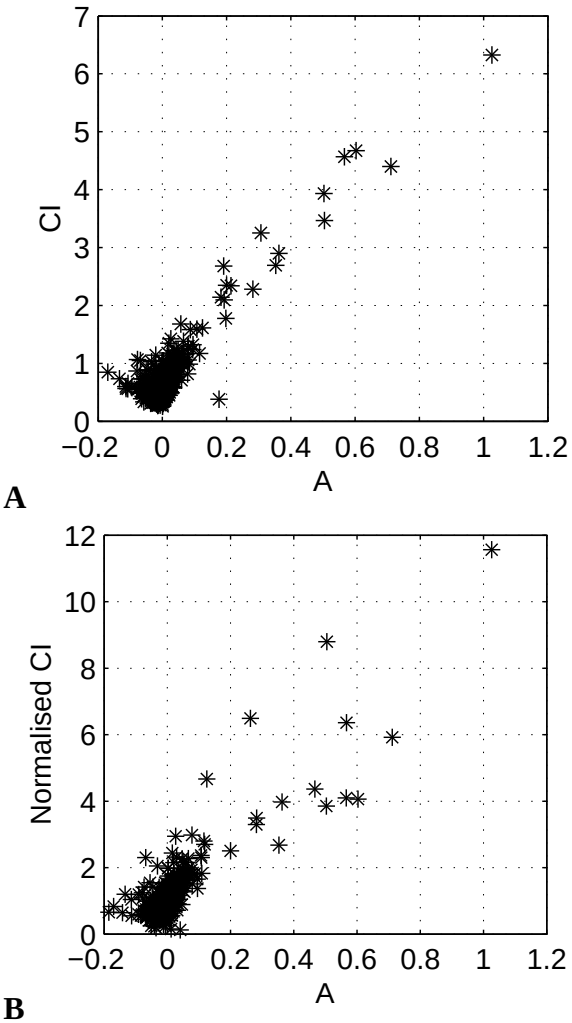

A

B

Fig. 4. Two CI measures vs. A, the peak fit coefficient. **A**: the absolute value at SZA = 94°. **B**: Normalised CI. These plots include the entire time series from December 1996 until March 2002.

of the instrument. Therefore, the single-scattering geometry shown in Figure 5 is important. The tangent height H_T of solar rays reaching the PSC (Table 1) is an important parameter to consider (Meinel and Meinel, 1983). As stated above, the sun is below the horizon even at typical PSC heights for solar zenith angles exceeding 95 degrees.

H_o	$H_{to}(92°)$	$H_{to}(93°)$	$H_{to}(94°)$	$H_{to}(95°)$
18	14.1	9.2	2.4	–
20	16.1	11.2	4.4	–
22	18.1	13.2	6.4	–
24	20.1	15.2	8.4	–
26	22.1	17.2	10.4	1.6
28	24.1	19.2	12.4	3.6

Table 1. Tangent heights [km] corresponding to PSC heights between 18 and 30 km at solar zenith angles between 92 and 95 degrees. A spherical Earth with a radius of 6378 km has been assumed and atmospheric refraction has been ignored.

The radiosonde average winter tropopause height at Kiruna is 9.5 ± 1.8 kilometres. Thus a varying cloud cover can exist

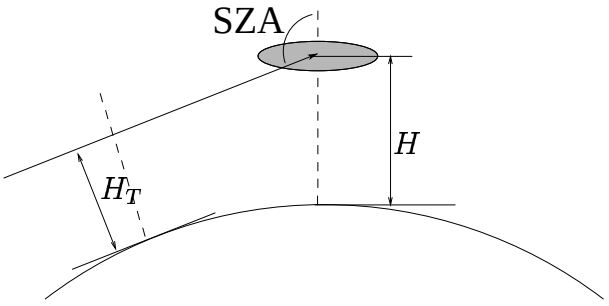

Fig. 5. The geometry of zenith scattering in the single-scattering approximation. SZA is the solar zenith angle, H the mean altitude of an object (PSC layer etc), and H_T the corresponding tangent height.

everywhere below that altitude, which implies that the contribution to zenith-scattering by all PSCs at altitudes below approximately 27 kilometres will be modified by tropospheric clouds in the vicinity of the tangent point (the difference between sunsets with clear and cloudy weather at the tangent point is also visually apparent). The effect of PSCs can therefore be screened out, depending on the character of tropospheric cloudiness. Normalisation of the CI clearly does not compensate for this effect, since single PSC scattering at SZA = 90° is not influenced by the troposphere.

Moreover, during the PSC season the solar azimuth at the relevant zenith angles varies from close to the south in midwinter to the east/west in March, which may even cause a seasonal variation in PSC detectability since the tropospheric climate (and hence cloud cover) is highly locally varying in the proximity of the Scandinavian mountain range.

5 Summary

It has been demonstrated that the zenith-sky colour index (CI) can be used as a means for passive optical detection of stratospheric clouds. Three different definitions of PSC indication CI thresholds have been examined. A least-squares fit of polynomials to CI peaks during twilight provides a useful threshold condition. Large values of the PSC index are obtained at temperatures below T_{NAT}. We suggest, however, that as a quantitative means of obtaining PSC statistics it very likely yields a lower limit. The importance of this underestimation remains to be quantified experimentally, e.g. by correlation with co-located lidar, photographic, visual and satellite observations, and theoretically by radiative transfer modelling.

The present principal application of the method still applies, namely the qualitative indication of PSC presence in cases when local tropospheric conditions prevent direct PSC observations. This has proven to be of practical use, not least when planning balloon launches of in-situ PSC experiments.

Acknowledgements. We want to thank Dr. K-H Fricke for pointing out the presence of curves with peaks at high solar zenith angles, which turned out to be the result of local light pollution.

References

Bohren, C. F. and Huffman, D. R., *Absorption and scattering of light by small particles*, John Wiley and Sons, Inc., 1983.

Crutzen, P. J. and Arnold, F., Nitric acid cloud formation in the cold Antarctic stratosphere: a major cause for the springtime "ozone hole", *Nature, 324*, 651–655, 1986.

Dörnbrack, A., Leutbecher, M., Reichardt, J., A.Behrendt, K.-P.Müller, and G.Baumgarten, Relevance of mountain waves for the formation of polar stratospheric clouds over Scandinavia: Mesoscale dynamics and observations for January 1997, *J. Geophys. Res.*, 2000.

Enell, C.-F., Steen, Å., Wagner, T., Frieß, U., and Platt, U., Occurrence of polar stratospheric clouds at Kiruna, *Ann. Geophys., 17*, 1457–1462, 1999.

Gao, R., Richard, E., Popp, P., Toon, G., Hurst, D., Newman, P., Holecek, J., Northway, M. W., Fahey, D., Danilin, M., Sen, B., Aikin, K., Romashkin, P., Schauffler, S., Greenblatt, J., McElroy, C., Lait, L., Bui, T., and Baumgardner, D., Observational evidence for the role of denitrification in Arctic stratospheric ozone loss, *Geophys. Res. Lett., 28*, 2879–2882, 2001.

Hanson, D. and Mauersberger, K., Laboratory studies of the nitric acid trihydrate: Implications for the south polar stratosphere, *Geophys. Res. Lett., 15*, 855–858, 1988.

Hesstvedt, E., On the physics of mother of pearl clouds, *Geofysiske Publikasjoner, 21*, 1960.

Hulburt, E., Explanation of the brigthness and color of the sky, particularly the twilight sky, *J. Opt. Soc. Am., 43*, 113–118, 1953.

Ingelstam, E., Rönngren, R., and Sjöberg, S., *TEFYMA, Handbok för teknisk fysik, fysik och matematik*, Sjöbergs Bokförlag AB, 1988.

Manney, G. L., Sabutis, J. L., Pawson, S., Santee, M. L., Naujokat, B., Swinbank, R., Melvyn E, G., and Ebisuzaki, W., Lower stratospheric temperature differences between meteorological analyses in two Arctic winters and their impact on polar processing studies, *J. Geophys. Res.*, 2001.

Meinel, A. and Meinel, M., *Sunsets, twilights, and evening skies*, Cambridge University Press, 1983.

Ougolnikov, O. S., Twilight sky photometry and polarimetry: The problem of multiple scattering at the twilight time, *Cosm. Res. (translated from Russian), 37*, 159–166, 1999.

Platt, U., Differential optical absorption spectroscopy, *Air Monitoring by Spectroscopic Techniques, chapter 2. John Wiley & Sons, Inc.*, 1994.

Poole, L., Osborn, M., and Hunt, W., Lidar observations of Arctic polar stratospheric clouds 1988: Signature of small, solid particles above the frost point, *Geophys. Res. Lett., 15*, 867–870, 1988.

Rozenberg, G. V., *Twilight*, Plenum Press, 1966.

Sarkissian, A., Pommereau, J.-P., and Goutail, F., Identification of polar stratospheric clouds from the ground by visible spectrometry, *Geophys. Res. Lett., 18*, 779–782, 1991.

Sarkissian, A., Pommereau, J., Goutail, F., and Kyrö, E., PSC and volcanic aerosol observations during EASOE by UV-visible ground-based spectrometry, *Geophys. Res. Lett., 21*, 1319–1322, 1994.

Sarkissian, A., Fierli, F., Goutail, F., Pommereau, J.-P., Kyrö, E., and Rummukainen, M., Frequency of occurrence of PSC above Northern Scandinavia from 1990 to 1997 from SAOZ zenith sky colour index, in *Polar stratospheric ozone 1997, Proceedings of the fourth European symposium*, edited by N. Harris, I. Kilbane-Dawe, and G. Amanatidis, vol. Air pollution research report 66, European Commission, 1998.

Sinnhuber, B.-M., Arlander, D. W., Bovensmann, H., Burrows, J. P., Chipperfield, M. P., Enell, C.-F., Frieß, U., Hendrick, F., Johnston, P. V., Jones, R. L., Kreher, K., Mohamed-Tahrin, N., Müller, R., Pfeilsticker, K., Platt, U., Pommereau, J.-P., Pundt, I., Richter, A., South, A. M., Tørnkvist, K. K., van Roozendael, M., Wagner, T., and Wittrock, F., The global distribution of stratospheric bromine monoxide: Intercomparison of measured and modeled slant column densities, *J. Geophys. Res.*, accepted, 2002.

Solomon, S., Schmeltekopf, A. L., and Sanders, R. W., On the interpretation of zenith sky absorption measurements, *J. Geophys. Res., 7*, 8311–8319, 1987.

Størmer, C., Photogrammetrische Bestimmung der Höhe von irisierenden Wolken (Perlmutterwolken) am 30. Dezember 1926, *Geofysiske Publikasjoner, 5*, 1930.

Tsias, A., Prenni, A. J., Carslaw, K. S., Onasch, T. P., Luo, B. P., Tolbert, M. A., and Peter, T., Freezing of polar stratospheric clouds in orographically induced strong warming events, *Geophys. Res. Lett., 24*, 2303–2306, 1997.

Voigt, C., Tsias, A., Dörnbrack, A., Meilinger, S., Luo, B., Schreiner, J., Larsen, N., Mauersberger, K., and Peter, T., Non-equilibrium compositions of liquid polar stratospheric clouds in gravity waves, *Geophys. Res. Lett., 27*, 3873–3876, 2000.

Paper IV

Carl-Fredrik Enell, Urban Brändström, Björn Gustavsson, Sheila Kirkwood, Kerstin Stebel and Åke Steen. **Case study of the development of polar stratospheric clouds using bistatic imaging**. *Ann. Geophys.*, 2002. Submitted.

Submitted to Annales Geophysicae, 2002

Annales Geophysicae (2002) 0000: 0001–9

LOGO

Case study of the development of polar stratospheric clouds using bistatic imaging

Carl-Fredrik Enell[1], **Urban Brändström**[1], **Björn Gustavsson**[2], **Sheila Kirkwood**[1], **Kerstin Stebel**[1,4], **and Aake Steen**[3]

[1]Swedish Institute of Space Physics, Kiruna, Sweden
[2]National Institute of Polar Research, Tokyo, Japan
[3]RemSpace Group, Linköping, Sweden
[4]Now at the Norwegian Institute of Air Research, Tromsø, Norway

Received: ??? – Accepted: ???

Abstract. The formation of polar stratospheric clouds (PSCs) is closely related to temperature, which is affected by stratospheric wave activity on different scales. We here present a case study of the development of visible PSCs undertaken by means of ground-based cameras. It is shown that appearance of stratospheric clouds may be detected semi-automatically and that short-term dynamics such as altitude variations can be tracked. The PSC field showed distinct features separated by approximately 20 km, which implies wave-induced temperature variations on that scale. The wave-induced characteristics are further emphasized by the fact that the PSCs moved within a sloping spatial surface.

1 Introduction

Polar stratospheric clouds (PSCs) play a very important role in atmospheric chemistry. The formation of PSCs involves condensation of water, H_2SO_4 and HNO_3, and freezing of nitric acid trihydrate (NAT) and water (Peter, 1997). Low stratospheric temperatures are required; the NAT condensation temperature T_{NAT} (Table 1) is an often used threshold value (Hanson and Mauersberger, 1988). In the orographically disturbed Arctic polar vortex the synoptic-scale temperature is often higher and PSC formation takes place where local cooling by mountain-induced waves occurs (Dörnbrack et al., 2000, and references therein). This is often the case when the vortex edge is located over the Scandinavian mountain ridge, close to our site of observation in Kiruna (67° N, 20° E), and the prevailing tropospheric wind direction is from the northwest. PSCs observed here may therefore show characteristic dynamic features on a scale which is not resolved in the synoptic-scale meteorological or chemistry/transport models generally used for assimilation of atmospheric data (including estimation of PSC area). Processes at this scale are inherently non-asymptotic (none of the force terms in the dynamic equations are fully negligible, as implied by the definition of mesoscale) and thus difficult to parameterise. We here apply three-dimensional mapping in a case study to track the development of a PSC field at time and length scales which are not easily covered with other methods.

Correspondence to: C.-F. Enell, Swedish Institute of Space Physics

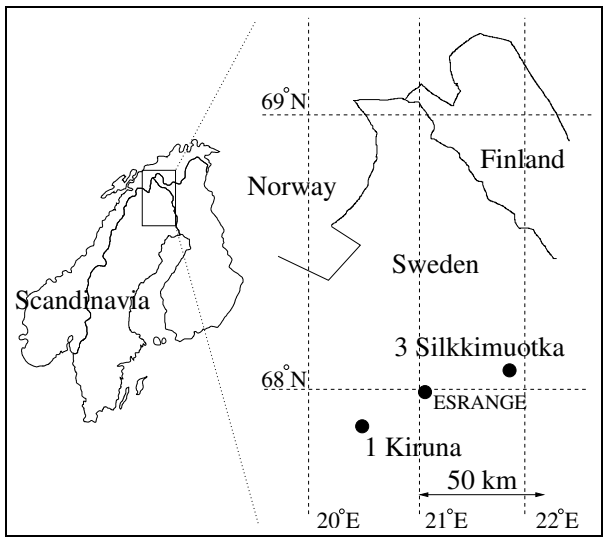

Fig. 1. Map of northernmost Sweden, showing the locations of ALIS station 1 (Kiruna, 67°50′27″N, 20°24′40″E), ALIS station 3 (Silkkimuotka, 68°1′47″N, 21°41′13″E), and ESRANGE.

2 Methods

2.1 Imaging

For the purpose of imaging ALIS, the Auroral Large Imaging System (Brändström and Steen, 1994), has been applied. ALIS consists of six remote-controlled stations with CCD imagers. The two stations applied here are shown in Figure 1. The baseline distances between the stations are adapted for auroral tomography, i.e. imaging of volumes above 100

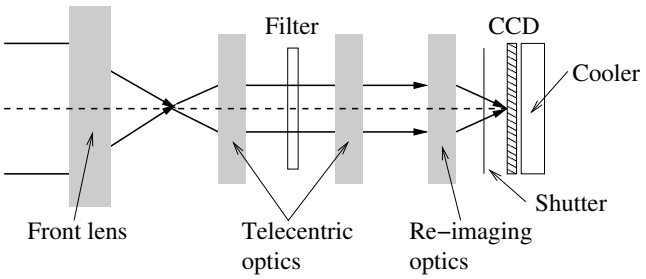

Fig. 2. Optical block diagram of an ALIS camera.

km. However, under suitable conditions PSCs located between stations can also be imaged (Steen et al., 1998).

Each imager (Figure 2) has a front lens with a field of view of 54°x54° and a telecentric lens system with one open (white-light) position and 5 different narrow-band interference filters (FWHM $\approx$ 40 Å). In this study, the white-light and 5590 Å positions have been used. The image detector is a cooled CCD with 1024x1024 imaging pixels divided into four 512x512-pixel quadrants for fast readout.

2.1.1 Image processing

A few corrections must be applied to each image. The differences between sensitivity and CCD bias levels in the four quadrants are compensated by using the values of covered so-called overscan pixels on the CCD. Thereafter, flat-field correction is applied. This is a compensation for the image radiance falloff towards the corners of the images caused by the decrease of effective front-lens area and projected pixel and object areas as the angle between the pixel and the optical axis increases. We finally subtract a background (approximation of non-PSC scattering) obtained by fitting a smooth surface to the minimum pixel values over fixed x $\times$ y image sub-blocks. As will be seen in Figure 20 below, this procedure renders the PSCs visible against a dark background.

2.2 Triangulation

The projection $(\varphi, \theta) = f(u, v)$, where (φ, θ) is the line-of-sight direction from a station and (u, v) is the corresponding pixel in its image, can be accurately determined by virtue of star calibration (Gustavsson, 2000). Every pixel center can therefore be mapped to a unique line of sight. Using bistatic imaging, the intersection of lines-of-sight from pixels corresponding to the same physical feature in pairs of images will in principle determine the geographic coordinates of the feature. In practice there will always be an error in the identification of corresponding pixels, so the lines of sight will not intersect. The task is instead to minimise the closest line-of-sight separation as shown in Figure 3.

2.3 Spatial correlation for approximate altitude mapping

This task of triangulating (stratospheric and other) clouds and studying their scattering properties is not trivial. Triangulation implies identification of corresponding details in pairs of images so that the least distance dr (Figure 3) for each pair of pixels is minimised. For clouds, which have no well-defined surfaces, this may be a difficult task depending on the viewing geometry and the conditions of illumination. It is therefore sometimes desirable to avoid manual feature identification. This led to the adoption of a principle of defining "cloud surfaces" as features showing high spatial correlation when viewed from separate directions. The underlying assumption is that cloud pixels in the separate images are highly spatially correlated whereas the background is noisy.

Figure 4 shows the principle behind the algorithm. The

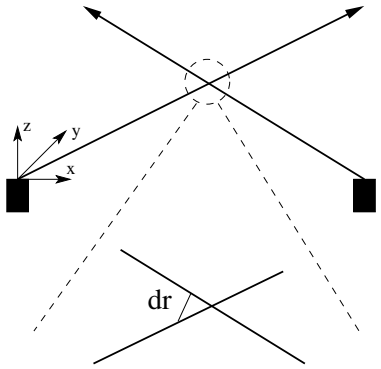

Fig. 3. The geometry of triangulation

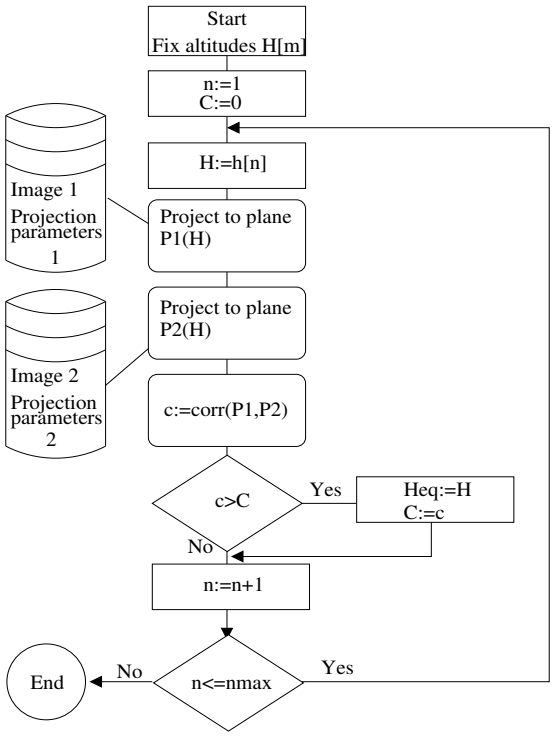

Fig. 4. Flowchart of a the algorithm for automatic determination of the equivalent altitude of best matching, H_{eq}. The designations Image 1 and Image 2 can refer to either full images or sub-blocks/regions of interest.

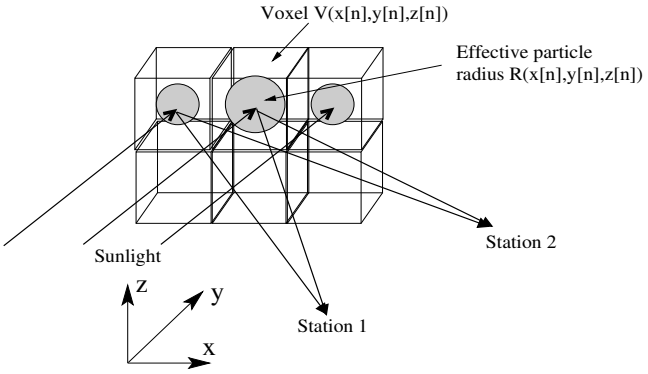

Fig. 5. Principle of the model type case for altitude matching

full images or regions of interest are projected to the line-of-sight directions and scaled to physical coordinates on a series of (arbitrary) planes of fixed altitude. For each plane the correlation of the projected pixels is calculated and the altitude plane of maximal pixel correlation is chosen as the equivalent PSC altitude.

3 Modelled test case

The performance of the automatic algorithm was tested with a model case outlined in Figure 5. For volume elements (voxels) of constant particle radius, assumed to be located at fixed positions with respect to stations 1 and 3, the single-scattering phase functions for the scattering angles defined by the incident sunlight and the directions towards the stations were calculated with the Bohren and Huffman (1983) Mie code. For simplicity a monodisperse Gaussian radius distribution of the form

$$r = r_0 \exp\left[\left(\frac{x - x_c}{s_x}\right)^2 + \left(\frac{y - y_c}{s_y}\right)^2 + \left(\frac{z - z_c}{s_z}\right)^2\right]$$

was applied, with coefficients appropriately chosen to produce radii in the two orders of magnitude between 0.1 and 10 μm over the model volume.

The resulting single-scattering radiances at a fixed solar zenith angle and azimuth (values typical of the January 9 case below were used), summed over a number of wavelengths around 5590 Å for three similar model volumes centered around different altitudes and superimposed on a smoothly varying background, have been projected to the image planes of station 1 (Figure 6A) and station 3 (Figure 6B). The resulting images resemble images of real mother-of-pearl clouds, at least in the backscatter geometry of station 1. In the forward direction (station 3), however, ringing-like structures appear (typical of the Mie solution) that are not visible in reality. This indicates that multiple scattering is important but that the single-scattering approximation may be valid at least for some regions of PSCs under certain wieving geometries, e.g. the outer layers of otherwise optically thick PSCs such

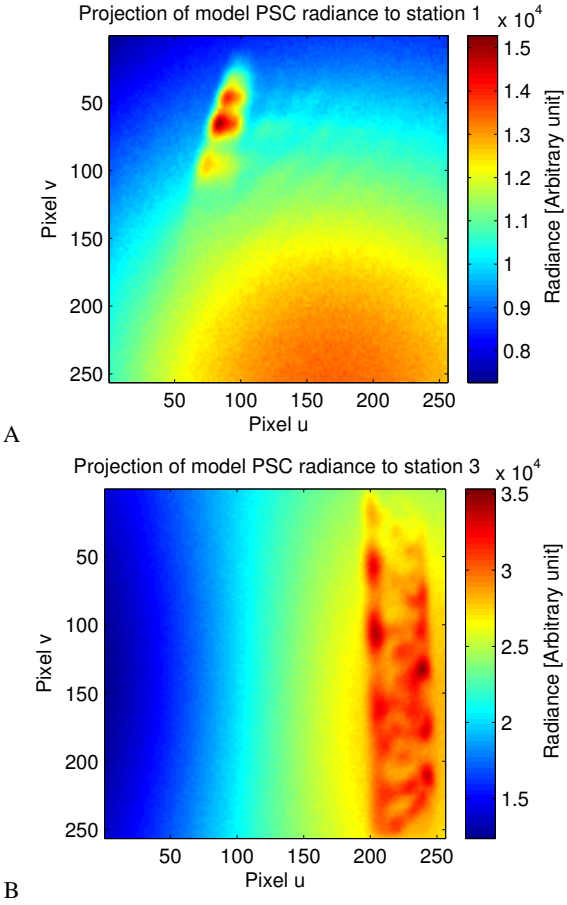

Fig. 6. Modelled images at stations 1 (A) and 3 (B) by scattering off the model volumes at 5590±40 Å, assuming sunset in the south/southwest.

as the laminar "sandwich clouds" discussed by Biele et al. (2001) and Shibata et al. (1999).

The projections were divided into sub-blocks and for each projection altitude the correlation coefficient was calculated for each pair of blocks. The correlations varied rapidly with altitude, but at the (here a priori known) altitude of the "model PSCs" the curves corresponding to adjacent blocks follow each other well around their maxima. This is seen as a peak at 20 km in Figure 7. As will be seen below, for our case of real PSC images the correlation has in fact a single maximum over the projection altitudes.

4 Observations - The case of January 9, 1997

Compared with previous years, an extreme number of visually observable PSC events occurred in January 1997. The polar vortex was strong and stable, leading to synoptic PSC presence over large areas in the Arctic. Tropospheric winds were persistently strong and westerly, leading to additional mountain-wave perturbations. January 9, 1997 was chosen as a test case since there were well-defined discrete PSC structures north of Kiruna and the troposphere was clear.

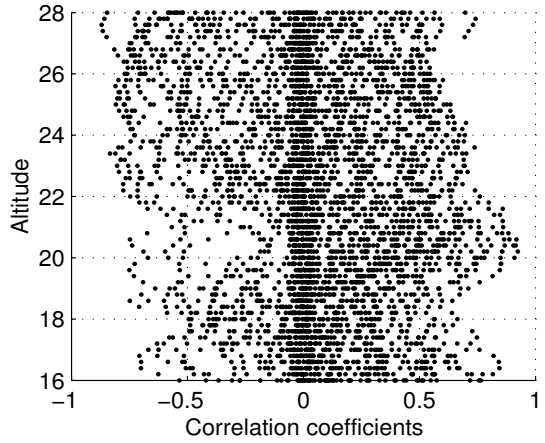

Fig. 7. Correlation coefficients for 8x8 image subblocks at 61 projected altitudes (16-28 km), showing the presence of an object at 20 km in the modelled pair of test images.

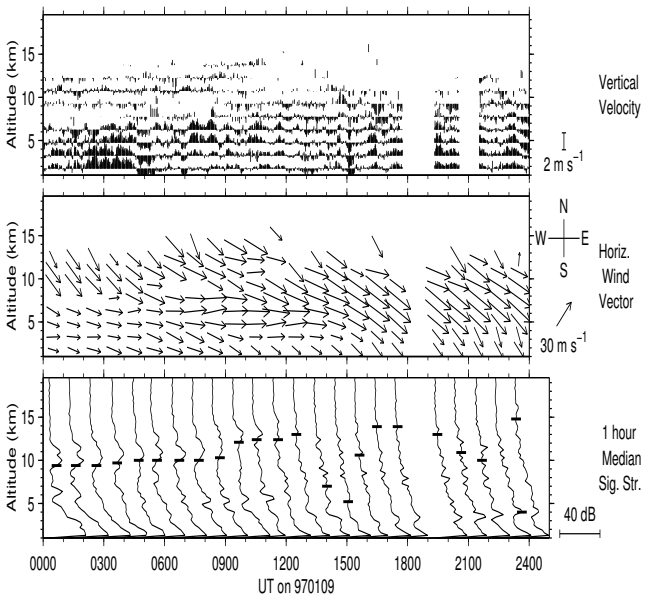

Fig. 8. ESRAD MST radar signal and winds on January 9, 1997

The ESRAD MST radar (Figure 8) showed a fluctuating vertical wind velocity, which is a signature of leewave activity, throughout the troposphere at the time of observation. Whether the waves propagated into the stratosphere is not evident (David Hooper, personal communication), but the presence of wavelike PSC structures can be interpreted as leewaves propagating into the stratosphere at least locally. The temperature profile of a radiosonde launched at Esrange the same day (Figure 9) confirms this. Although the balloon burst already at 18km, clear temperature fluctuations which may indicate wave activity and/or proximity to the vortex edge region appear.

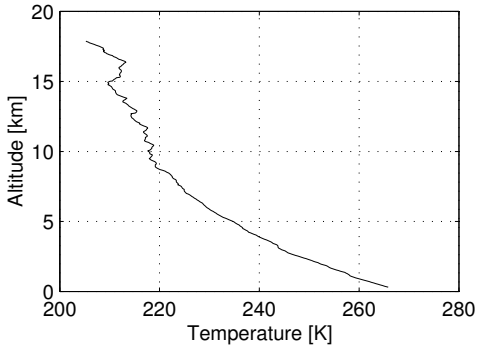

Fig. 9. Temperature profile from a radiosonde launched at Esrange on January 9, 1997.

4.1 History of the observed air masses

Synoptic-scale backtrajectories (Figure 10 A) indicated that the air mass arriving above Kiruna on this date had been repeatedly warmed and cooled to temperatures close to T_{NAT} for the 10 preceding days. The assumed values of T_{NAT} (according to Hanson and Mauersberger, 1988) are given in Table 1 together with typical polar stratosphere altitudes of the isentropic levels. The potential vorticity values (Figure 10 B) are indicative of the air mass being close to the vortex edge, as confirmed by the synoptic-scale plot of potential vorticity (Figure 11).

Especially interesting is the fact that the air mass experienced a cooling followed by a slight warming during the last few days before January 9, 1997. Although there were no synoptic PSCs, the air was preconditioned for the observed PSC formation in leewaves, whose rapid temperature fluctuations can drive the composition out of chemical equilibrium (Tsias et al., 1997).

Level	**Appr. altitude** [km]	$\mathbf{T_{NAT}}$ [K]
475 K	20	194.5
550 K	23	191.6
675 K	26	187.8

Table 1. T_{NAT} for the three isentropic levels under consideration.

4.2 The bistatic image series

A series of more than 20 image pairs was taken after sunset, between 14 and 16 UTC. Station 1 imaged in white light whereas station 3 used the 5590 Å filter to reduce the high sunset radiance. The exposure times used varied between 10ms and 60s depending on time after sunset and filtering.

The solar depression varied from 8 to 16 degrees during this time interval. The PSCs were therefore illuminated by scattered light only since the daylight terminator was in fact well south of Scandinavia. January 9, 1997 also happened to be a day of new moon, so additional lunar illumination can be ruled out. A smooth intensity variation is therefore ob-

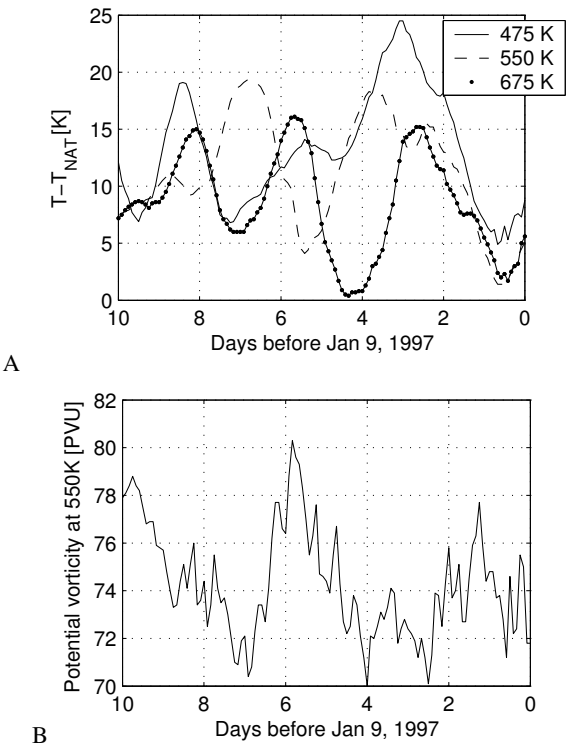

Fig. 10. Temperatures and potential vorticity along ECMWF back-trajectories from Kiruna for January 9, 1997

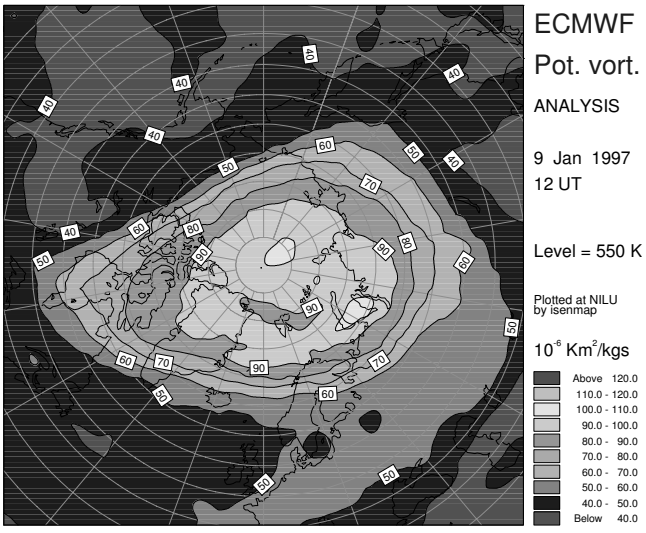

Fig. 11. ECMWF synoptic-scale analysis of potential vorticity at the 550 K level on January 9, 1997.

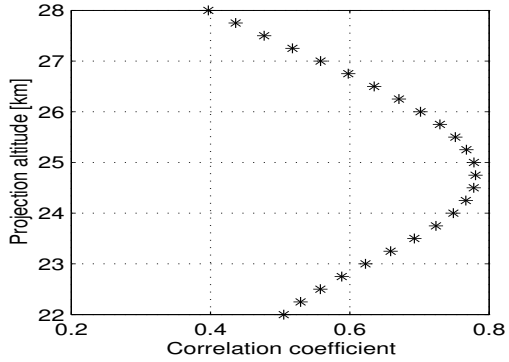

Fig. 12. Typical correlation coefficient between pixels of image pairs projected to consecutive altitudes.

served, in contrast to the iridescence observed on direct solar illumination. The central PSCs were also sufficiently optically thick to prevent star observations during the projection calibration. This also contributes to a well-defined observable structure.

4.3 Automatic determination of equivalent altitude

Correlation between the projections from stations 1 and 3 produced smooth curves (Figure 12 is a typical result) in this case. The altitude of maximum correlation is therefore easily determined. On this day it varied around 25 kilometres, which is consistent with lidar observations (Reichardt et al., 1999) starting 15:15 UTC at Esrange, located south of the observed PSCs between the stations as shown in Figure 1. The same procedure was repeated with the projections divided into sub-blocks. In Figure 13, the projections have been divided into 4×4 subimages. This gives the possibility to sort out only subimages that actually contain PSC pixels. The sub-projections can also be allowed to have their maximal correlations at different altitudes, since PSCs are generally not flat.

A problem of the blockwise projections is apparent, namely that the overlap is not smooth if the blocks are too large. We therefore chose to use the equivalent altitudes of the full projections, since there were no tropospheric clouds in the images. The time variation of the mean PSC altitudes thus obtained was examined with the Lomb periodogram (Press et al., 1992). In Figure 14 the result has been plotted (with the angular frequency ω converted to period T by $T = \frac{2\pi}{\omega}$) over a range of periods. The main period present is approximately 40 minutes. This may be due to a real period in the PSC altitude, connected with gravity wave activity, or due to other effects (such as the aspect sensitivity caused by the fact that the PSC surfaces are sloping whereas these projections are plane).

4.4 Tracking features by manual triangulation

To clarify the issue of altitude variation we proceed by manual tracking of single details in the PSCs, as well as the 3-D

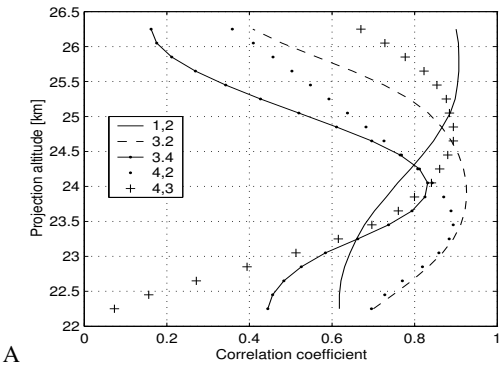

A

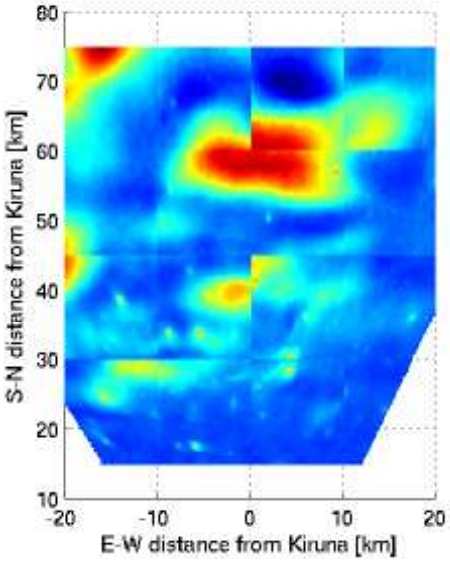

B

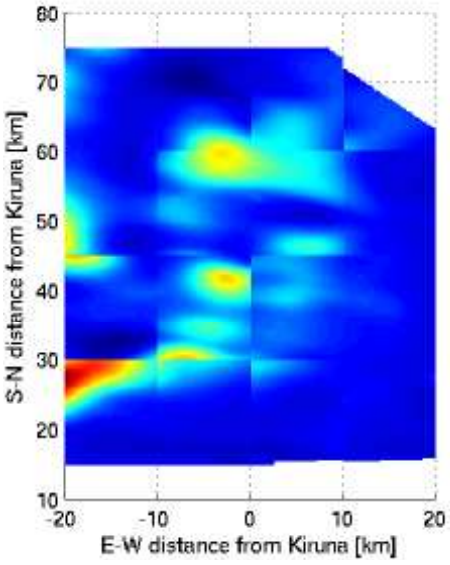

C

Fig. 13. Example of algorithm performance. A: The correlation vs. altitude for the PSC regions (subimage row,column) of the images taken 15:21:30 UTC, and the corresponding projections from station 1 (B) and station 3 (C). The colour scale shows pixel values in arbitrary units.

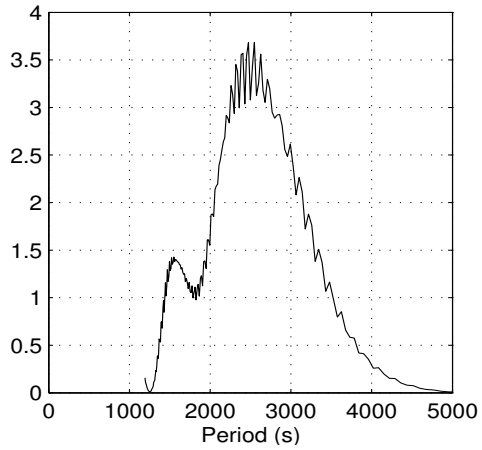

Fig. 14. Periodogram of the altitudes of maximal full-projection correlations for the image series of January 9, 1997. The abscissae are an interval of angular frequencies converted to periods.

surfaces spanned by those points, by visual identification of distinct features in the images. Figure 20, columns 1 and 2, shows a subset of these image pairs where correctly exposed images with distinct PSC features for triangulation have been selected. The points identified for triangulation are marked with corresponding numbers within each pair of images. The resulting PSC altitudes are also visualised. Column 3 shows projections of the images from station 1 (Kiruna) with superimposed contours of equal altitude. From column 3 it is evident that the altitude contours must not be interpreted as outlines of the PSCs but as surfaces containing spatially separated PSCs.

In Figure 15, we concentrate on identified points in well-defined visual contour lines within the PSCs. Points within the same contour line are connected with lines. Although these points do not correspond to the same contours for all images, the result confirms the grouping of visible PSCs into discrete structures separated 10-20 km. Similarly, Figure 16 (same data as Figure 15, viewed in the X-Z plane, i.e. a west-east altitude transect) shows the persistent slope of the PSC field from 25 down to 20 km in the west-east direction.

The temporal order of the lines in Figures 15– 16 is not shown. For this reason, one feature present in as many well-exposed image pairs as possible has been singled out. The spatial locations of this single line during the time sequence is shown in Figure 17, whereas Figure18 shows the time variation of the mean altitude. Lines some kilometers apart from the main grouping appear, which possibly should be removed as misidentified outliers. However, the remaining results fall within the PSC field seen above, spatially sloping from an altitude above 25 km down to 20 km. It therefore seems that the altitude variation of the PSCs takes place on an isentrope distorted by mountain-wave activity. The time variation of the mean altitude is apparently quasi-periodic as before. The Lomb periodogram of these altitudes vs. time has been calculated in the same way as in Figure 14 and is shown in Fig-

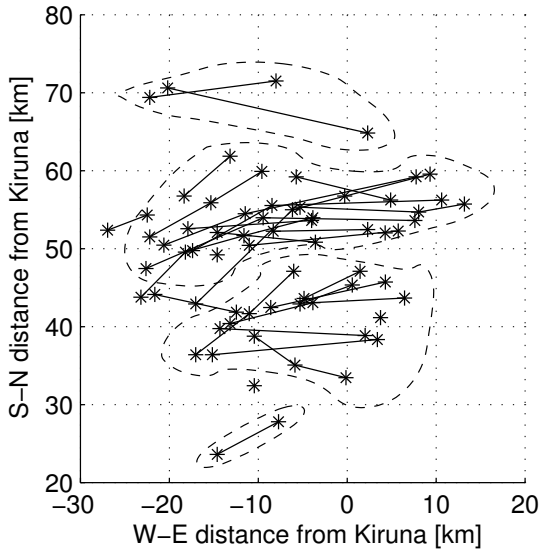

Fig. 15. Identifiable contour lines from all image pairs (as many as possible per pair). The points show triangulated positions with points in the same visual contour feature joined by lines. These PSC "edges", and hence the PSCs, show a grouping in structures separated 10-20 km.

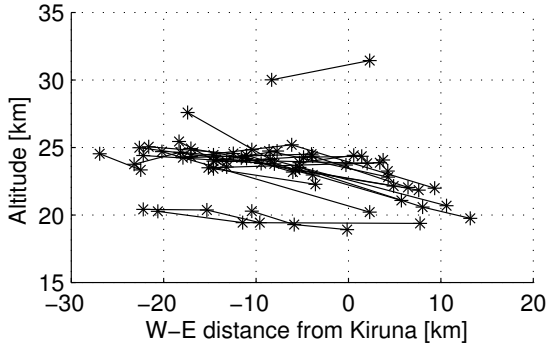

Fig. 16. The same contour lines as in the previous figure, but viewed in the W-E/altitude plane, showing the slope of the PSC field.

ure 19. Again the period of close to 40 minutes appears, as in the automatic matching retrieval. The image series used covers only slightly more than an hour. However, the use of unevenly spaced data samples reduces the degeneracy so that substantially less aliasing of short-term variations occurs (Press et al., 1992). We therefore believe that this period can indeed be present in the altitude variation.

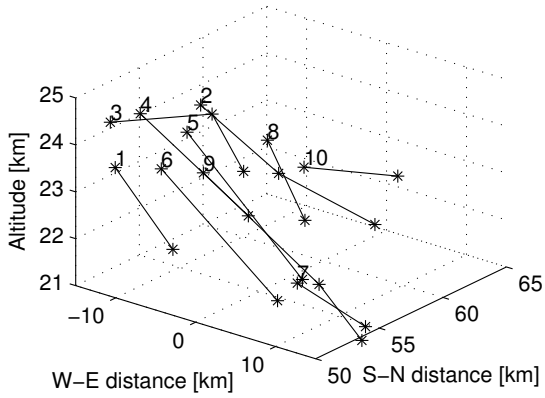

Fig. 17. Time development of a single visually identified feature in the PSC field observed on January 9, 1997. A minimum of two points in the contour have been identified in each image pair where possible. As above, distances are in km relative to the Kiruna station. The numbering refers to the same times of day as the abscissae of Figure 18, in ascending order.

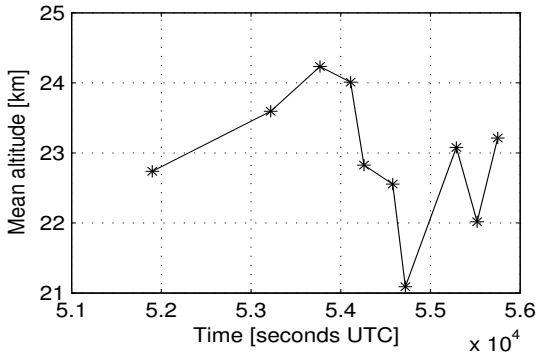

Fig. 18. The mean altitude vs. time of day of the lines in Figure 17.

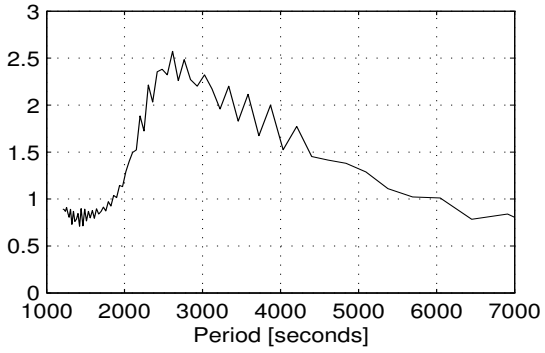

Fig. 19. Lomb periodogram of the temporal variation of the mean altitudes of the lines in Figure 17.

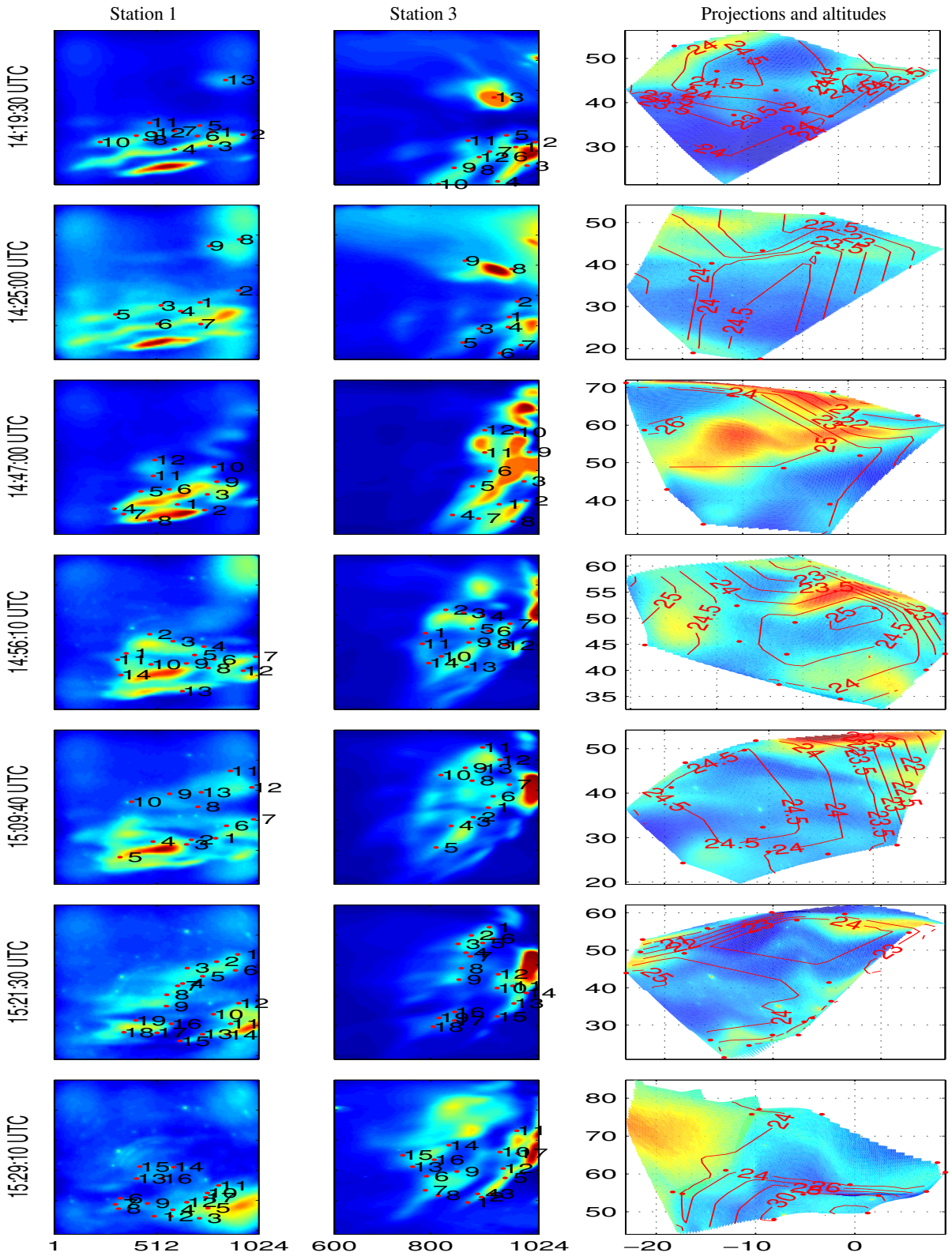

Fig. 20. Columns 1 and 2: Time series of images with identified PSC points (colourbars show the pixel values in 10^4 A/D counts after background subtraction). Rows 1-1024 and columns according to the abscissae are shown. Column 3: Contour surfaces of altitudes [km] spanned by these points, superimposed on projections of the images from station 1. The axes show W-E and N-S distances in kilometres from Kiruna.

5 Conclusions

We have observed PSCs during twilight on January 9, 1997. Discrete mother-of-pearl-like structures, also conspicuously visible during daytime, moved within a stationary sloping surface. This can be interpreted as fluctuations in a quasi-stationary wave pattern, since the PSCs can be assumed to form at the wave-induced temperature minima. Since the sun was below the horizon the visual effects of a changing solar zenith angle should not lead to misidentification of structures. The site of observation was at the edge of the polar vortex and the air masses also originated from the vortex edge. This altogether provides some evidence that the observed PSCs were indeed leewave-induced. This is also in agreement with Hesstvedt (1962); Tsias et al. (1997) and other works, which draw the conclusion that a monodisperse particle size distribution is required for the iridescent colours observed earlier on the same day in the PSC field to appear, and that this is likely to be obtained under the conditions prevailing on January 9, 1997.

Given that visible PSC structures correspond to temperature minima, we can furthermore confirm that wave-induced temperature variations on a scale of 10-20 kilometres occur. As pointed out by Carslaw et al. (1998) this can cause a discrepancy between observations and modelled values in studies of atmospheric chemistry. Until recently it has been a time-consuming task to model such scales. At present, however, a comparison with temperature fields produced by mesoscale models is a viable task.

On January 9, 1997 only white-light and monochromatic imaging were used on the two stations respectively. For future work it would be desirable to repeat these observations with polarisation-sensitive devices in order to characterise the scattered light with the full set of Stokes parameters at different wavelengths (Georg Witt, personal communication). Only this can yield information on particle shapes and the nature of the multiply scattered light illuminating the PSCs.

The possibility to image PSCs under different conditions of illumination, such as direct or scattered sunlight, moonlight, and even extinction of starlight, also deserves further experimental investigation.

Acknowledgements. Calculations of back-trajectories from ECMWF data, available at the Norwegian Institute of Air Research (NILU), have been provided by Bjørn Knudsen, Danish Meteorological Institute. The observations in January 1997 were performed in the frame of the European leewave project, using coordinated lidar, radar, and other observations in northern Scandinavia.

The work has been partly financed by the Environment and Space Research Institute in Kiruna (MRI).

The main author is also thankful to Peter Rydesäter for many discussions on image processing.

References

Biele, J., Tsias, A., Luo, B., Carslaw, K., Neuber, R., Beyerle, G., and Peter, T., Nonequilibrium coexistence of solid and liquid particles in Arctic stratospheric clouds, *J. Geophys. Res.*, *106*, 22 991–23 007, 2001.

Bohren, C. F. and Huffman, D. R., *Absorption and scattering of light by small particles*, John Wiley and Sons, Inc., 1983.

Brändström, U. and Steen, Å., ALIS - a new ground-based facility for auroral imaging in northern Scandinavia, in *Proceedings of ESA Symposium on European Rocke and Balloon Programmes*, ESA SP-355, Eurpoean Space Agency, 1994.

Carslaw, K. S., Wirth, M., Tsias, A., Luo, B. P., Dörnbrack, A., Leutbecher, M., Volkert, H., Renger, W., Bacmeister, J. T., Reimers, E., and Peter, T., Increased stratospheric ozone depletion due to mountain-induced atmospheric waves, *Nature*, *391*, 675–678, 1998.

Dörnbrack, A., Leutbecher, M., Reichardt, J., A.Behrendt, K.-P.Müller, and G.Baumgarten, Relevance of mountain waves for the formation of polar stratospheric clouds over Scandinavia: Mesoscale dynamics and observations for January 1997, *J. Geophys. Res.*, 2000.

Gustavsson, B., *Three Dimensional Imaging of Aurora and Airglow*, Ph.D. thesis, Swedish Institute of Space Physics, iSBN 91-7191-878-7, 2000.

Hanson, D. and Mauersberger, K., Laboratory studies of the nitric acid trihydrate: Implications for the south polar stratosphere, *Geophys. Res. Lett.*, *15*, 855–858, 1988.

Hesstvedt, E., A two-dimensional model of mother-of-pearl clouds, *Tellus*, *XIV*, 1962.

Peter, T., Microphysics and heterogeneous chemistry of polar stratospheric clouds, *Annual Review of Physical Chemistry*, *48*, 785–822, 1997.

Press, W. H., Teukolsky, S. A., Vetterling, W. T., and Flannery, B. P., *Numerical Recipes in C*, Cambridge University Press, second edn., 1992.

Reichardt, J., Behrendt, A., Baumgart, R., and Weitkamp, C., Koordinierte Feldmessungen zum Einfluß von Leewellen auf Wolkenfelder in der polaren Stratosphäre, Tech. rep., GKSS Forschungszentrum, Geesthacht, Germany, 1999.

Shibata, T., Shiraishi, K., Adachi, H., Iwasaka, Y., and Fujiwara, M., On the lidar-observed sandwich structure of polar stratospheric clouds (PSCs) 1. Iimplications for the mixing state of the PSC particles, *J. Geophys. Res.*, *104*, 21 603–21 611, 1999.

Steen, Å., Gustavsson, B., and Brändström, U., Temporal variation of 2-D altitude distribution of lee-wave generated polar stratospheric clouds, in *Polar stratospheric ozone 1997, Proceedings of the fourth European symposium 22 to 26 September 1997, Schliersee, Bavaria, Germany*, vol. Air pollution research report 69, European Commission, 1998.

Tsias, A., Prenni, A. J., Carslaw, K. S., Onasch, T. P., Luo, B. P., Tolbert, M. A., and Peter, T., Freezing of polar stratospheric clouds in orographically induced strong warming events, *Geophys. Res. Lett.*, *24*, 2303–2306, 1997.

Paper V

Björn-Martin Sinnhuber, D. W. Arlander, Heinrich Bovensmann, John P. Burrows, Martyn P. Chipperfield, Carl-Fredrik Enell, Udo Frieß, Francois Hendrick, Paul V. Johnston, R. L. Jones, Karin Kreher, Norhaslinda Mohamed-Tahrin, R. Müller, Klaus Pfeilsticker, Ulrich Platt, Jean-Pierre Pommereau, Irene Pundt, Andreas Richter, Alex M. South, Kjersti K. Tørnkvist, Michel van Roozendael, Thomas Wagner and Folkard Wittrock. **Comparison of measurements and model calculations of stratospheric bromine monoxide**. *J. Geophys. Res.*, 107(D19):11:1–18, 2002.

Comparison of measurements and model calculations of stratospheric bromine monoxide

B.-M. Sinnhuber,[1,10] D. W. Arlander,[2] H. Bovensmann,[3] J. P. Burrows,[3] M. P. Chipperfield,[1] C.-F. Enell,[4] U. Frieß,[5] F. Hendrick,[6] P. V. Johnston,[7] R. L. Jones,[8] K. Kreher,[7] N. Mohamed-Tahrin,[8] R. Müller,[3] K. Pfeilsticker,[5] U. Platt,[5] J.-P. Pommereau,[9] I. Pundt,[5,9] A. Richter,[3] A. M. South,[8] K. K. Tørnkvist,[2] M. Van Roozendael,[6] T. Wagner,[5] and F. Wittrock[3]

Received 11 June 2001; revised 25 February 2002; accepted 9 May 2002; published 12 October 2002.

[1] Ground-based zenith sky UV–visible measurements of stratospheric bromine monoxide (BrO) slant column densities are compared with simulations from the SLIMCAT three-dimensional chemical transport model. The observations have been obtained from a network of 11 sites, covering high and midlatitudes of both hemispheres. This data set gives for the first time a near-global picture of the distribution of stratospheric BrO from ground-based observations and is used to test our current understanding of stratospheric bromine chemistry. In order to allow a direct comparison between observations and model calculations, a radiative transfer model has been coupled to the chemical model to calculate simulated slant column densities. The model reproduces the observations in general very well. The absolute amount of the BrO slant columns is consistent with a total stratospheric bromine loading of 20 ± 4 ppt for the period 1998–2000, in agreement with previous estimates. The seasonal and latitudinal variations of BrO are well reproduced by the model. In particular, the good agreement between the observed and modeled diurnal variation provides strong evidence that the BrO-related bromine chemistry is correctly modeled. A discrepancy between observed and modeled BrO at high latitudes during events of chlorine activation can be resolved by increasing the rate constant for the reaction $BrO + ClO \rightarrow BrCl + O_2$ to the upper limit of current recommendations. However, other possible causes of the discrepancy at high latitudes cannot be ruled out. *INDEX TERMS:* 0340 Atmospheric Composition and Structure: Middle atmosphere—composition and chemistry; 0394 Atmospheric Composition and Structure: Instruments and techniques

Citation: Sinnhuber, B.-M., et al., Comparison of measurements and model calculations of stratospheric bromine monoxide, *J. Geophys. Res.*, *107*(D19), 4398, doi:10.1029/2001JD000940, 2002.

1. Introduction

[2] Bromine compounds are believed to play an important role in the destruction of stratospheric ozone, both at high and midlatitudes [e.g., *World Meteorological Organization* (*WMO*), 1999 and references therein; *Daniel et al.*, 1999]. Model calculations show that bromine reactions may contribute more than 50% to the seasonal Arctic ozone depletion [*Chipperfield and Pyle*, 1998]. Also in the midlatitude lower stratosphere, catalytic bromine reactions account for a large fraction of the halogen induced ozone loss [*Wennberg et al.*, 1994].

[3] The origin of atmospheric bromine is both natural and anthropogenic. However, due to the emission of anthropogenic compounds there has been a large increase of the atmospheric bromine loading from about 10 parts per 10^{12} by volume (ppt) in the 1970s to about 20 ppt in 2000 [*Fraser et al.*, 1999; *Sturges et al.*, 2001]. The major sources of stratospheric bromine are methyl bromide (CH_3Br), halons, especially Halon-1211 ($CBrClF_2$), Halon-1301 ($CBrF_3$) and Halon-2402 ($CBrF_2CBrF_2$), as well as bromochloromethane (CH_2BrCl) and dibromomethane (CH_2Br_2) [*Fraser et al*, 1999; *WMO*, 1999, chapter 1], with methyl bromide being the most abundant bromine source gas, accounting for about 50% of the current atmospheric sources. In addition it has recently been proposed [e.g.,

[1]School of the Environment, University of Leeds, UK.
[2]Norwegian Institute for Air Research, Kjeller, Norway.
[3]Institute of Environmental Physics, University of Bremen, Germany.
[4]Swedish Institute of Space Physics, Kiruna, Sweden.
[5]Institute of Environmental Physics, University of Heidelberg, Germany.
[6]Belgian Institute for Space Aeronomy, Brussels, Belgium.
[7]National Institute of Water and Atmospheric Research, Lauder, New Zealand.
[8]Centre for Atmospheric Science, University of Cambridge, UK.
[9]Service d'Aéronomie, Verrières-le-Buisson, France.
[10]Now at Institute of Environmental Physics, University of Bremen, Germany.

0148-0227/02/2001JD000940$09.00

Ko et al., 1997; *Dvortsov et al.*, 1999; *Schauffler et al.*, 1999; *Pfeilsticker et al.*, 2000; *Sturges et al.*, 2000] that there could be a significant contribution of short-lived organic (e.g., bromoform, $CHBr_3$) and inorganic tropospheric sources to the total bromine loading of the stratosphere. This would then lead to a higher total bromine loading of the stratosphere than deduced from measurements of the organic source gases alone.

[4] Despite its importance for stratospheric ozone chemistry, there are few measurements of inorganic bromine compounds in the stratosphere. Except for BrO, there exist no measurements of the major inorganic bromine species; in particular $BrONO_2$ and BrCl have never been observed in the stratosphere. For HOBr there exist only measurements of upper limits [*Johnson et al.*, 1995].

[5] Stratospheric BrO has been measured by ground-based zenith sky UV–visible spectroscopy [*Carroll et al.*, 1989; *Arpag et al.*, 1994; *Fish et al.*, 1995; *Aliwell et al.*, 1997; *Eisinger et al.*, 1997; *Kreher et al.*, 1997; *Otten et al.*, 1998; *Frieß et al.*, 1999; *Richter et al.*, 1999], balloon-borne UV–visible spectroscopy [e.g., *Harder et al.*, 1998; *Pundt et al.*, 1999b; *Fitzenberger et al.*, 2000; *Harder et al.*, 2000] and in-situ resonance fluorescence spectroscopy both from aircraft [e.g., *Brune et al.*, 1988, 1989; *Toohey et al.*, 1990; *Avallone et al.*, 1995] and balloon [*McKinney et al.*, 1997].

[6] The recent balloon borne UV–visible measurements of BrO [e.g., *Harder et al.*, 1998; *Pundt et al.*, 1999b; *Harder et al.*, 2000] showed relatively good agreement with model calculations. This is in contrast to in-situ BrO observations from the ER-2 aircraft [*Avallone et al.*, 1995], which indicated a BrO/Br_y ratio in the lower stratosphere of about 40%, compared to about 60% calculated by photochemical models.

[7] *Renard et al.* [1998] showed evidence from balloon-borne spectroscopic measurements that OBrO could be present in significant amounts in the stratosphere and could even be a major nighttime bromine reservoir. However, the formation of significant amounts of OBrO in the stratosphere cannot be explained with our current understanding of the atmospheric bromine chemistry [*Chipperfield et al.*, 1998]. Moreover, *Erle et al.* [2000] reported measurements of upper limits of OBrO which argue against OBrO being a significant nighttime bromine reservoir.

[8] Here we compare ground-based UV–visible measurements of BrO from a network of observing stations with calculations from the SLIMCAT global 3D chemical transport model (CTM) [*Chipperfield*, 1999]. The measurements have been performed from a network of sites ranging from the Arctic, over northern and southern hemisphere midlatitudes to Antarctica, most of them part of the Network for the Detection of Stratospheric Change (NDSC). We focus on a period of two and a half years from January 1998 until June 2000, allowing us to investigate the seasonal, and to some extent the inter-annual, variation of BrO. Previous studies [e.g., *Fish et al.*, 1995, 1997; *Frieß et al.*, 1999] have been limited to short periods and individual locations.

[9] The interpretation of the zenith sky UV–visible measurements is complicated, as the primary quantity measured is the BrO slant column density (SCD) along the slant path traversed by the scattered sunlight. This is even further complicated by the fact that BrO can vary strongly with solar zenith angle (SZA) along the slant path. To allow a direct comparison between observed and modeled BrO, we simulate the measurement geometry by coupling a radiative transfer model to the chemical model to calculate simulated BrO slant column densities.

[10] In section 2 we briefly review our current understanding of stratospheric bromine chemistry. Sections 3 and 4 then describe the measurements and the model, respectively. The comparison between measurements and model is presented in section 5. In section 6 we present some sensitivity studies to investigate the impact of different processes on the modeled slant column densities. A discussion of the results and our conclusions are given in sections 7 and 8.

2. Stratospheric Bromine Chemistry

[11] Unlike chlorine, a large fraction of the lower stratospheric inorganic bromine during daytime is present in reactive form as BrO. The following reactions

$$BrO + NO_2 + M \rightarrow BrONO_2 + M, \quad (1)$$

$$BrO + HO_2 \rightarrow HOBr + O_2, \quad (2)$$

and

$$BrO + ClO \rightarrow BrCl + O_2 \quad (3a)$$

$$\rightarrow Br + ClOO \quad (3b)$$

$$\rightarrow Br + OClO \quad (3c)$$

convert BrO into the main bromine reservoirs bromine nitrate ($BrONO_2$), HOBr and BrCl. During daytime BrO is quickly released from the reservoir species by photolysis or by the reaction of HOBr with $O(^3P)$. Recent laboratory measurements by *Soller et al.* [2001] indicate that the reaction $BrONO_2 + O(^3P)$ could be an important source of BrO (see section 6.4). Bromine nitrate is believed to be the major bromine reservoir species, accounting for roughly half of the inorganic bromine in the lower stratosphere, except for periods of high chlorine activation. Despite its important role in stratospheric bromine chemistry, bromine nitrate has never been measured in the stratosphere.

[12] Bromine nitrate can be converted heterogeneously by hydrolysis on sulfate aerosols into HOBr [*Hanson and Ravishankara*, 1995; *Hanson et al.*, 1996]:

$$BrONO_2 + H_2O(aq) \rightarrow HOBr + HNO_3. \quad (4)$$

As a result of the hydrolysis of $BrONO_2$, we expect HOBr to be a major bromine reservoir before sunrise in the lower stratosphere. The hydrolysis of $BrONO_2$ is also of general importance, as it influences the HO_x and NO_x abundances, which has significant direct and indirect effects on the lower stratospheric ozone depletion [*Hanson et al.*, 1996; *Lary et al.*, 1996]. *Lary et al.* [1996] showed that reaction (4) is consistent with the rapid increase of HO_x at sunrise due to the photolysis of HOBr, as observed by *Salawitch et al.* [1994]. Observational evidence for the importance of reaction (4) on cold stratospheric aerosols for halogen activation has been presented by *Erle et al.* [1998]. *Slusser*

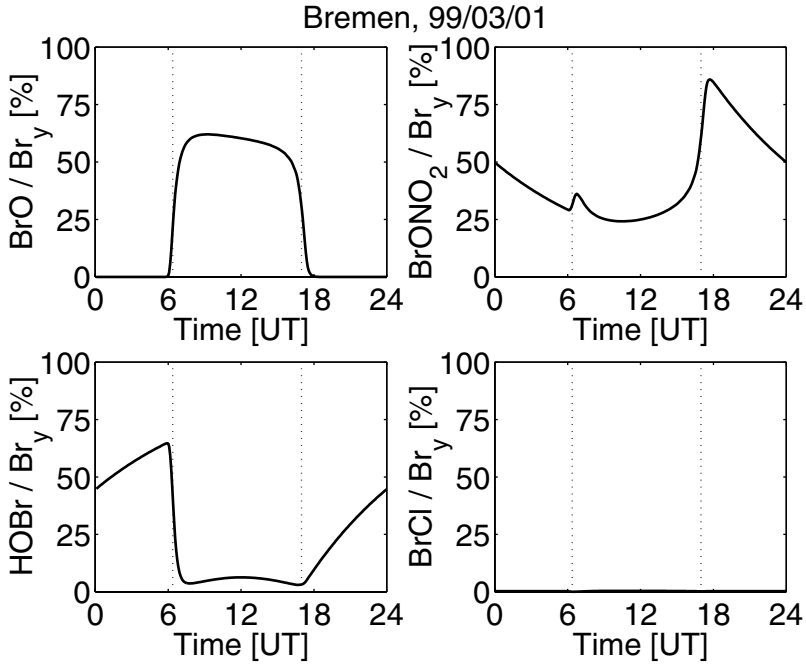

Figure 1. Diurnal cycle of the relative contribution of the most abundant bromine species BrO, $BrONO_2$, HBr and BrCl in the lower stratosphere (480 K isentropic level, 58 hPa), calculated by the photochemical model described in the text. This example for Bremen (53°N) for 1 March 1999 shows the typical bromine partitioning at midlatitudes.

et al. [1997] presented observational evidence that reaction (4) had a significant impact in reducing stratospheric NO_x in the presence of Pinatubo aerosols.

[13] At higher altitudes between about 25–35 km, HOBr becomes less important. Here inorganic bromine is predominantly partitioned between BrO and $BrONO_2$.

[14] As an example, Figure 1 shows the modeled diurnal cycle of bromine partitioning in the lower stratosphere, calculated by the model described in section 4 below. This example for Bremen (53°N) for 1 March 1999 shows the typical behavior at midlatitudes in the lower stratosphere: BrO is about 60% of the available inorganic bromine during daytime, with bromine nitrate the most important bromine reservoir. Bromine nitrate is heterogeneously converted into HOBr during nighttime (reaction 4), which is then the major bromine reservoir at sunrise.

[15] In contrast, Figure 2 shows the situation for high chlorine activation for Harestua (60°N) for 29 January 2000. The concentrations of $BrONO_2$ and HOBr are very low and the inorganic bromine is almost exclusively partitioned between BrO and BrCl.

3. Measurements

[16] The measurements reported in this study were obtained by zenith sky UV–visible spectroscopy, performed at 11 stations. The measurement sites range from northern high latitudes (Ny-Ålesund, Andøya, Kiruna), over northern midlatitudes (Harestua, Bremen, Cambridge, Observatoire de Haute-Provence, OHP, Huelva), southern midlatitudes (Lauder) to southern high latitudes (Neumayer, Arrival Heights), see Table 1.

[17] This work relies on a network of UV–visible spectrometers set up to observe the zenith scattered sunlight in the spectral region between 346 and 359 nm, where BrO can be measured by the method of differential optical absorption spectroscopy (DOAS) [e.g., *Platt*, 1994]. The instruments share the same general design, based on the use of thermally stabilized grating spectrometers equipped with low-noise cooled array detectors, optimized for the detection of weak atmospheric absorbers in the UV–visible region. All spectrometers are largely oversampled with resolutions in the range from 0.6 to 0.9 nm, which provide a good compromise between resolution and light throughput resulting in optimal sensitivity to the vibrational absorption structures of BrO.

[18] At all sites the DOAS analysis for BrO is performed according to the precise guidelines developed and extensively described by *Aliwell et al.* [2002], based on the results of the BrO intercomparison campaign held at Observatoire de Haute Provence in June 1996. These guidelines include recommendations on the wavelength range to be used (346–359 nm) as well as the number and nature of absorption cross-sections to be included in the DOAS analysis. Note that all groups involved in the present study also took part in this former exercise, which resulted in the cross-validation of the different analysis software tools used at the various institutes and, in general, significantly contributed to the improvement of the consistency of the BrO data set used in the present work. The precision of the BrO observations reported here is about 15% (1σ), as derived from the spectral fits. The absolute accuracy is limited by the uncertainty in the temperature-dependent BrO absorption cross-sections as well as by more subtle spectral

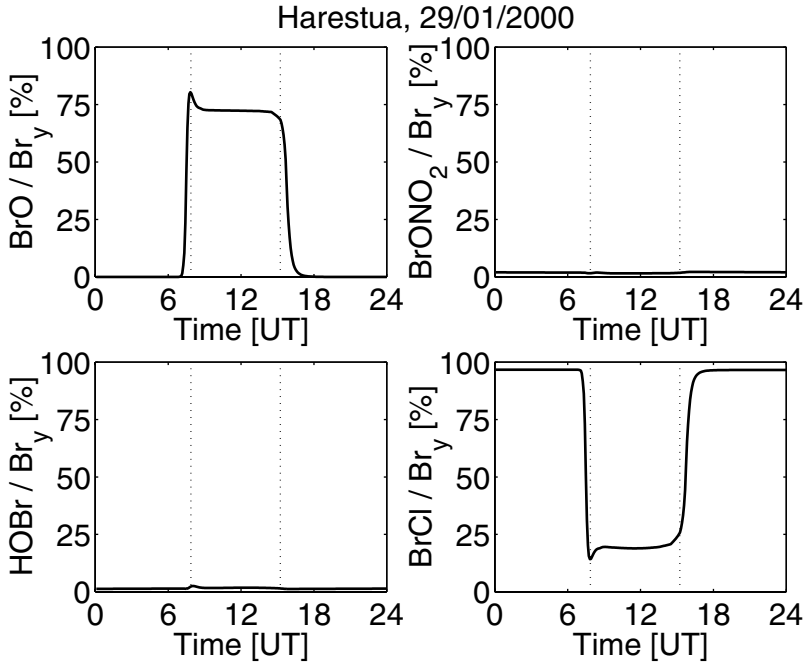

Figure 2. As Figure 1 but for Harestua (60°N) for 29 January 2000 (480 K isentropic level, 40 hPa). This example shows the bromine partitioning for a situation of high chlorine activation.

interference effects known to produce offsets in the data retrieval depending on the analysis settings adopted [*Aliwell et al.*, 2002]. The uncertainty of the BrO cross-sections is about ±10% at 223 K, but could be larger at cold temperatures [e.g., *Harder et al.*, 2000]. As a result of the temperature dependence of the BrO cross-sections, it is likely that the retrievals overestimate the true BrO slant columns by up to 20% at low polar temperatures. We thus estimate the overall accuracy of the measurements to be better than 23% for all cases except cold polar conditions, and better than 30% for cold polar conditions (1σ).

[19] This study compares observations and model simulations of the difference in BrO slant column between 90° and 80° SZA. Differential slant columns are the natural product of the zenith sky DOAS observations and have generally been reported as such in previous studies on BrO because of the significant uncertainties that would affect the conversion to vertical column amounts without accounting properly for the strong diurnal change of BrO [*Fish et al.*, 1995]. The choice of the 90–80° SZA range was done primarily to optimize the signal-to-noise ratio of the differential BrO absorption. However, this choice also presents the advantage of maximizing the sensitivity of the observation to the stratospheric part of the BrO profile, due to the strong geometrical enhancement of the optical path in the stratosphere at twilight [e.g., *Solomon et al.*, 1987] and the comparatively small variation of the tropospheric air mass factor.

[20] We focus here on a period of two and a half years from January 1998 to June 2000. This period was chosen to have maximum overlap between the BrO time series from

Table 1. Geographic Locations of the BrO Measurement Sites

Station	Latitude	Longitude	Institution	Reference
		Arctic		
Ny-Ålesund, Spitsbergen	79°N	12°E	U. Bremen	*Eisinger et al.* [1997]
Andøya, Norway	69°N	16°E	NILU	*Tørnkvist et al.* [2002]
Kiruna, Sweden	68°N	21°E	U. Heidelberg/IRF Kiruna	*Otten et al.* [1998]
		Northern Midlatitude		
Harestua, Norway	60°N	10°E	IASB-BIRA	*Van Roozendael et al.* [1999a]
Bremen, Germany	53°N	9°E	U. Bremen	*Eisinger et al.* [1997]
Cambridge, United Kingdom	52°N	0°E	U. Cambridge	*Fish et al.* [1995]
Observatoire de Haute-Provence, OHP, France	44°N	6°E	IASB-BIRA	*Van Roozendael et al.* [1999a]
Huelva, Spain	37°N	7°W	U. Cambridge	*South et al.* [1999]
		Southern Midlatitude		
Lauder, New Zealand	45°S	167°E	NIWA	*Kreher et al.* [1997]
		Antarctic		
Neumayer Station, Antarctica	70°S	8°W	U. Heidelberg	*Frieß et al.* [2001]
Arrival Heights, Antarctica	78°S	167°E	NIWA	*Kreher et al.* [1997]

the different stations. In addition, we included winter and spring 2000 to allow a comparison between the relatively warm stratospheric conditions during the Arctic winters 1997/1998 and 1998/1999 and the cold stratospheric conditions during winter 1999/2000.

4. Model

[21] The model used in this study is the SLIMCAT global 3D chemical transport model (CTM), described in detail by *Chipperfield* [1999]. The model is forced by temperature and horizontal wind fields from UKMO analyses [*Swinbank and O'Neill*, 1994]. It was initialized in October 1991 from a 2D (latitude-height) model and then integrated at $5^\circ \times 7.5^\circ$ horizontal resolution. The model as used in this study has 12 isentropic levels, ranging from 335 to 2700 K, corresponding to an altitude range of approximately 10 to 55 km. Vertical transport across isentropic levels is calculated from interactively computed diabatic heating rates. At the lower boundary mixing ratios from 2D model results are prescribed to account for trace gas fluxes into the model domain from below. Liquid aerosol is calculated from the H_2SO_4 loading, specified month-by-month from detailed two-dimensional (latitude-height) time-dependent calculations [*Bekki and Pyle*, 1994] and advected as a passive tracer by the CTM.

4.1. Chemistry

[22] The model calculations shown here used photochemical reaction rate constants and photolysis cross-sections from the JPL 1997 reaction rate recommendations [*DeMore et al.*, 1997] with a few exceptions: Reaction rate constants for $NO_2 + OH \rightarrow HNO_3$ and $HNO_3 + OH \rightarrow NO_3 + H_2O$ were taken from *Brown et al.* [1999a] and *Brown et al.* [1999b], respectively. These rates have a significant impact on the NO_x/NO_y ratio and thus on the BrO concentrations. We find that the use of these updated reaction rates decreases the BrO concentrations by approximately 10% in the midlatitude lower stratosphere, compared to JPL 1997 reaction rates. The decrease in BrO is smaller than the increase in $BrONO_2$ (approximately 20%), since part of the increase in $BrONO_2$ is compensated by a decrease in HOBr. Another exception from JPL 1997 is that we use the HOBr photolysis cross-sections from *Ingham et al.* [1998], which clearly shows a third absorption band centered at 457 nm, resulting in a faster HOBr photolysis compared to JPL 1997 recommendations. All changes from JPL 1997 kinetics described so far are now also included in the recent JPL 2000 reaction rate recommendations [*Sander et al.*, 2000]. In addition, the branching ratio of the $BrONO_2$ photolysis has recently been measured by *Harwood et al.* [1998]. Their result shows a quantum yield of close to unity for the production of NO_3 in the relevant wavelength range. This is in clear contrast to the JPL 1997 recommendations. In the present study we thus assume that the production of $Br + NO_3$ is the only channel.

[23] The model calculations assume a total bromine loading of 20 ppt, which is in agreement with observations of organic bromine compounds of 18 ppt for 1994 and 20 ppt for 1996 by *Wamsley et al.* [1998] and *Schauffler et al.* [1999], respectively, and an inferred total bromine loading from balloon borne BrO measurements of 20 ppt for 1996 and 21.5 ppt for 1998/1999 by *Harder et al.* [2000] and *Pfeilsticker et al.* [2000], respectively. The only bromine source gas in the model is methyl bromide, CH_3Br, which is scaled to produce a realistic total organic bromine loading. This approach leads to a reasonable approximation of the total inorganic bromine (Br_y) profile, since (a) the rate of release of bromine is similar for most of the different organic source gases [*Wamsley et al.*, 1998, Table 4] and (b) CH_3Br is by far the most important bromine source gas anyway, accounting for more than 50% of the organic bromine loading. A more detailed estimation shows, that the use of CH_3Br as the only bromine source gas will underestimate the inorganic bromine loading in the lowermost stratosphere by less than about 1 ppt (or about 25%), based on the empirical correlation of the different bromine source gases with $CFCl_3$ (CFC-11) from *Wamsley et al.* [1998]. *Pundt et al.* [1999b] found good agreement between vertical profiles of Br_y derived empirically from in-situ measurements of CFC-11 and modeled Br_y profiles from the SLIMCAT CTM for Arctic and midlatitude conditions. More fundamental is probably the neglection in the model of any short-lived organic and inorganic bromine sources.

[24] The global output from the 3D CTM is saved only every second day at 12UT. The diurnal cycle of BrO at the stations is then calculated by a 1D column model (stacked box model) with identical chemistry as in the 3D CTM, initialized with the 3D model.

4.2. Calculation of Slant Columns

[25] To calculate BrO slant column densities from the modeled BrO, we have coupled a radiative transfer model to the chemistry model. The model takes into account single scattering by the so-called intensity weighting approach, as described by *Solomon et al.* [1987]. The model uses full spherical geometry and explicitly takes into account the variation of BrO with SZA along the slant path. Comparisons with two other radiative transfer models showed good agreement (F. Hendrick, unpublished manuscript) [see also *Hendrick et al.*, 1999]. Figure 3 shows the intensity-weighted air mass factor, that is the effective path length for a given SZA averaged over all possible scattering heights according to their contribution to the total intensity received at the ground. The BrO slant column density is similarly obtained by averaging the integrals of the BrO number density along the slant paths for all possible scattering heights, weighted by the total intensity received. The calculations were performed for a wavelength of 352 nm—corresponding to the center of the BrO fit window of the measurements—with the Rayleigh scattering cross-section taken from *Bates* [1984]. Note that the air mass factor approaches unity in the troposphere for large SZA. This is because at large SZA most of the scattering takes place in the stratosphere and the underlying tropospheric levels are traversed vertically. This means that any BrO amount below about 13 km effectively decreases the BrO $90-80^\circ$ differential slant columns, as can be seen from Figure 3. A more detailed analysis shows that under typical midlatitude conditions the largest contribution to the $90^\circ-80^\circ$ DSCD comes from a layer $\sim$10 km thick centered at about 22 km altitude. At high latitudes under conditions of enhanced chlorine activation the largest contribution comes from slightly lower altitudes, centered at about 18 km altitude.

[26] The calculations include only Rayleigh scattering and do not take into account the effect of refraction. In

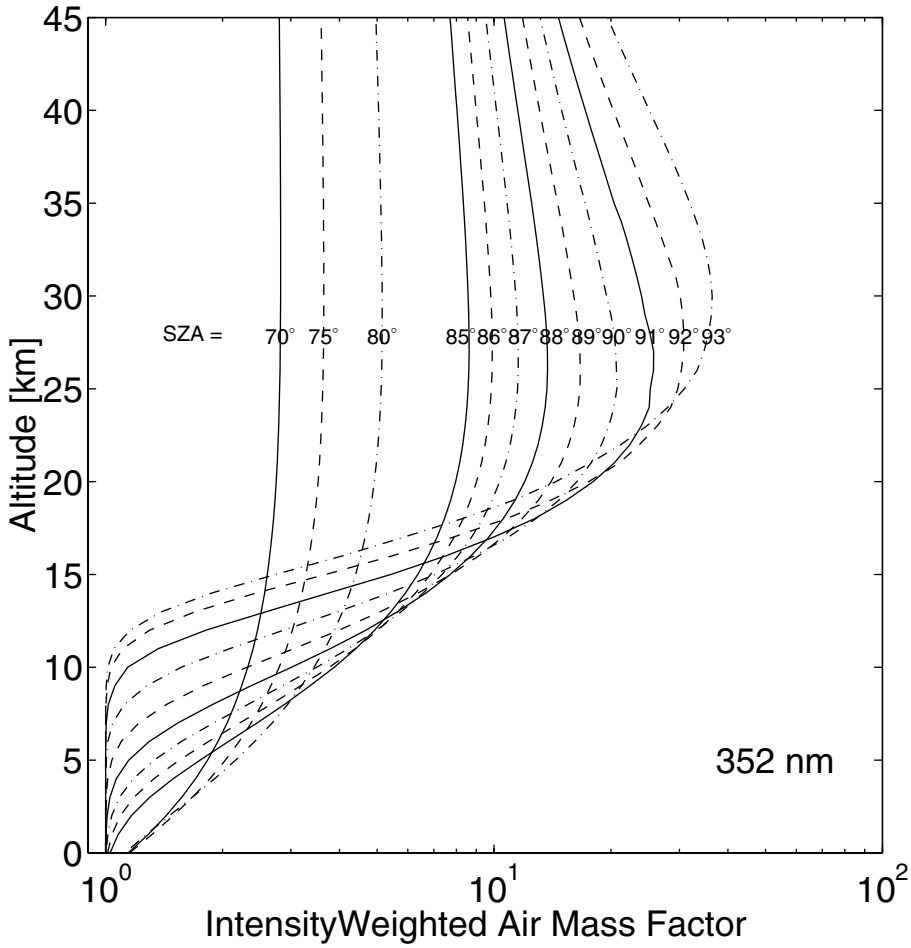

Figure 3. Intensity weighted air mass factors (see text) as a function of altitude for different solar zenith angles (SZA).

section 6.2 we investigate the effect of aerosol scattering on the calculated BrO slant column densities.

[27] An example of calculated BrO slant columns for 1 March 1999 for Bremen is shown in Figure 4. The treatment of the variation of BrO along the slant path has a very large impact on the slant column densities at large SZA, as BrO changes very rapidly around 90° SZA. This is shown in Figure 4 by comparing the calculated slant columns with the variation of BrO along the slant path taken into account (labeled "2D") and a calculation where BrO is constant along the slant path (labeled "1D"). It is essentially this variation of BrO along the slant path which makes a full multiple scattering calculation of BrO slant column densities difficult. In section 6.1 we show some comparisons of calculated BrO slant columns using this single scattering model with a novel multiple scattering calculation. However, since the multiple scattering calculations are very time consuming, we use the single scattering model for the comparison of measured and modeled BrO differential slant columns.

5. Comparison of Measured and Modeled Slant Columns

[28] Figure 5 shows the measured BrO 90–80° differential slant columns together with the model calculation for the different stations. The model reproduces the observations generally very well. The mean differences between measured and modeled BrO DSCD, calculated on a point-by-point basis, are shown in Table 2. For most of the stations measured DSCD are higher than modeled DSCD by about 10%. The scatter of the difference is about 20% for most of the stations. The differences, as well as the scatter, are generally about the same for sunrise (AM) and sunset (PM) observations. The fact that the mean discrepancies between measurements and model are similar for most of the stations, in particular for stations that are close to each other e.g., Kiruna and Andøya, demonstrates the good internal consistency of the observational network.

[29] However, two stations clearly stand out: For Ny-Ålesund (79°N) and Neumayer (70°S) the measurements are much lower than the model with a large scatter in the differences. As both stations are frequently located at the edge of the sea ice, it is likely that at least part of the discrepancy and scatter results from enhanced tropospheric boundary layer BrO events. Such events, which are observed both over the Arctic and Antarctic in spring [e.g., *Kreher et al.*, 1997; *Richter et al.*, 1998; *Wagner and Platt*, 1998; *Wagner et al.*, 2001], are likely related to processes when the sea ice breaks up in spring. *Kreher et al.* [1997] showed that these events lead to a decrease of the 90–80° BrO DSCD, basically due to the different air mass factors for tropospheric and stratospheric absorbers (see

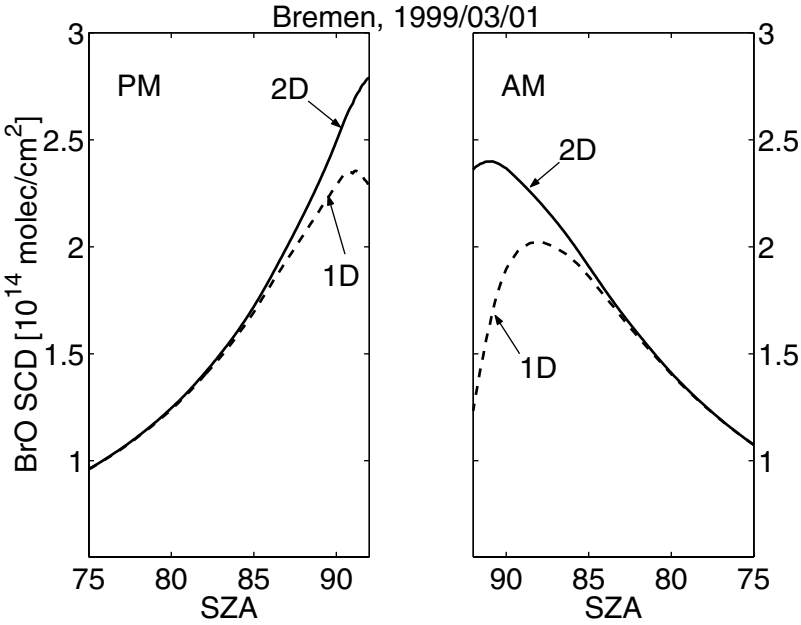

Figure 4. Calculated BrO slant column densities for the example case for Bremen, 1 March 1999 shown in Figure 1. The line marked "2D" shows the result from the calculation including the variation of BrO with solar zenith angle along the slant path. This is compared to a calculation with constant BrO along the slant path (marked "1D").

Figure 3). For Arrival Heights, however, the differences between measurements and model are more in line with the other (midlatitude) stations. This is consistent with the fact, that events of enhanced tropospheric BrO are not often observed at this station.

[30] At Arrival Heights the difference between observed and modeled BrO DSCD is significantly larger during spring than during the rest of the year. During spring, the model overestimates the observations (for both, AM and PM) by about 20%. A similar discrepancy of about 20% can also be seen, for example, at Kiruna and Andøya in early March 2000 and at Harestua under the influence of polar vortex air masses. It is thus likely related to situations of enhanced chlorine activation, where BrCl becomes the main bromine reservoir. The temperature dependence of the BrO absorption cross-section is most likely to be of the opposite sense, with the cross-section likely being larger by about 12% at 195 K compared to 223 K. As this is not taken into account in the BrO retrievals in this study, it is likely that the difference under cold polar conditions is even larger.

[31] The seasonal and latitudinal variations of the observed BrO DSCD are generally well reproduced by the model. The seasonal and latitudinal variations are basically due to the combined effect of variations of the Br_y column due to transport and variations of the bromine partitioning due to chemistry. The Br_y column shows a seasonal variation similar to total ozone, with a maximum in late winter and spring and a minimum in late fall. The BrO/Br_y ratio on the other hand shows a seasonal cycle with a maximum in winter of about 70% and a minimum in summer of about 50% at midlatitudes, as it is driven mainly by the seasonal cycle of NO_2 in the lower stratosphere. While the day-to-day variability in the BrO column at a given location is largely a result of changes in the Br_y column, the seasonal cycle of BrO is dominated by changes in bromine partitioning.

[32] For a number of cases there are events of enhanced BrO DSCD observed at midlatitudes, most clearly seen at Harestua and Bremen. These events are associated with the advection of polar vortex air masses and are, in many cases, also reproduced by the model.

[33] The model also reproduces the diurnal cycle generally very well, with PM BrO DSCD generally larger than AM DSCD. This diurnal cycle is most clearly seen at the midlatitude sites of OHP and Lauder (44°N and 45°S, respectively), with a maximum in winter and a minimum in summer. At higher latitudes the AM/PM variation is much smaller and also well reproduced by the model. At polar latitudes, during events of large chlorine activation in spring, the model shows a reversed AM/PM ratio, with BrO DSCD higher at AM than PM, in agreement with the observations [see also *Tørnkvist et al.*, 2002].

[34] To allow a better comparison of the diurnal variation, Figure 6 shows the difference of the PM-AM BrO differential slant columns for OHP and Lauder. The diurnal cycle is most clearly seen at these stations, thus providing a good test for the model's chemistry. The error bars in Figure 6 represent monthly averages and their standard deviation. In the case of the measurements the errors thus represent the precision of the measurements plus the atmospheric variability, while in the case of the model they represent only the atmospheric variability. For both stations the agreement between the observed and modeled diurnal variation is very good. The model agrees well with the observations within their standard deviation. Both the absolute amount, as well as the seasonal variation of the AM/PM variation are well reproduced. The AM/PM variation in the model is not influenced by any dynamical or radiative transfer effects,

but only by the diurnal cycle of the chemistry. This comparison thus provides a critical test for the model's stratospheric bromine chemistry. Note that the modeled AM/PM variation changed between 1998 and 1999/2000, being in better agreement with the observations at OHP during the latter years. It is caused by a decrease in NO_y in the model during this period, possibly as a result of changes in transport, linked to changes in the analyzed winds used to force the model.

[35] Although the measurements reported here cover a wide range of latitudes over both hemispheres, measurements of BrO in the tropics are notably missing. They would be needed to achieve a truly "global" picture of the stratospheric bromine chemistry. In Figure 7 we show the modeled BrO DSCD for a tropical site. The calculation has been performed for Kaashidhoo, Maldives (5°N, 73°E), where some of us (Richter and coworkers) performed BrO zenith sky measurements during February and March of 1999. Due to technical problems experienced during the campaign, BrO slant columns are still under evaluation. It is planned to continue UV–visible zenith sky measurements at Kaashidhoo in the near future. In addition, another group (Johnston and coworkers) started BrO zenith sky measurements at Hawaii (20°N) in December 1999.

6. Sensitivity Studies

[36] To investigate the impact of different processes on the calculation of the modeled BrO DSCD, a number of sensitivity calculations have been performed. In this section we discuss the impact of multiple scattering, aerosol scattering and a possible tropospheric BrO background on the modeled BrO DSCD. In addition we show the impact of uncertainties in the rate constants for the most important reactions.

6.1. Multiple Scattering

[37] To test the impact of the single scattering approximation on the calculated BrO slant column densities, we did comparisons with a full multiple scattering model which included the variation of BrO along the slant path [*Müller et al.*, 2002; *Rozanov et al.*, 2001]. Figure 8 shows the BrO slant column densities for single- and multiple scattering calculations. The single scattering approximation leads to an underestimation of the *absolute* BrO slant column density of about 2×10^{13} molecules/cm^2, about 10–15%. However, the impact on the *differential* slant column densities is much smaller. In fact, we found that the single scattering approximation can both underestimate or overestimate the BrO DSCD, depending on the BrO profile. In any case, the impact of the single scattering approximation on the differential slant column densities seems to be small. However, it may not be justified to ignore the effect of multiple scattering if one compares absolute slant column densities.

6.2. Aerosol Scattering

[38] Stratospheric aerosol can have an impact on the air mass factor [e.g., *Sarkissian et al.*, 1995], influencing the measured BrO slant columns. To test the sensitivity of the calculated BrO slant columns due to aerosol scattering, we performed calculations with a standard aerosol extinction profile, representative for stratospheric background conditions (Figure 9). This assumed extinction profile is generally consistent with observations by the Polar Ozone and Aerosol Measurement III (POAM III) satellite instrument at 353.4 nm (Karl Hoppel, personal communication, 2000). The calculations assumed a Henyey-Greenstein phase function [e.g., *Liou*, 1992], using an asymmetry parameter of 0.7. Figure 10 shows the calculated impact of the assumed aerosol extinction profile on the BrO slant columns for a given day. For the case shown here, aerosol scattering leads to a reduction of the BrO slant column density of about 5% at 90° SZA. The calculations shown here also include a tropospheric aerosol extinction profile. However, it was found that tropospheric aerosols have only a small impact on the BrO slant column. We found that the relative impact of stratospheric aerosol scattering on the BrO DSCD for the same aerosol extinction profile is largest during winter and smallest during summer, which is essentially due to the different shape of the BrO profile. In any case we found that the inclusion of aerosol scattering for a stratospheric background aerosol profile leads to a reduction in the BrO DSCD of not more than about 10%. However, polar stratospheric clouds may have a substantial impact on the differential slant columns.

6.3. Tropospheric BrO Background

[39] To test the impact of a possible tropospheric BrO background on the calculated DSCD, a sensitivity calculation was performed with an assumed additional constant BrO mixing ratio of 1 ppt between the ground and the lowest stratospheric model level. This assumed tropospheric BrO background is similar to the inferred tropospheric BrO values of *Frieß et al.* [1999], *Pundt et al.* [1999a], *Van Roozendael et al.* [1999b], and the recently observed tropospheric BrO profile by *Fitzenberger et al.* [2000]. The result of this calculation is shown in Figure 11. The additional tropospheric BrO contribution leads to an increase in the absolute slant column densities of 1.7 to 2.9 $\times$ 10^{13} molecules/cm^2, with the smaller increase at larger SZA. Note that no diurnal variation of this assumed tropospheric BrO background has been considered. A constant tropospheric BrO contribution (or one which decreases with increasing SZA) will thus lead to a small decrease of the BrO slant column densities for 90–80°, as the absolute slant column contribution from the assumed tropospheric BrO background is higher for the reference at 80° than for 90°.

[40] Table 3 summarizes the results of the sensitivity calculations. The calculations in Table 3 have been performed for the midlatitude site of Bremen. Calculations for OHP for different seasons (for comparison with Figure 6) lead to basically the same results.

[41] As a result of these sensitivity studies, we see that differential slant columns are generally less affected than absolute slant columns. In particular multiple scattering and

Figure 5. (opposite) Comparison of observed and modeled BrO differential slant column densities. Shown are differential slant columns between solar zenith angles of 90° and 80°. In some cases, when 80° were not reached at high latitudes, the local noon values were used as reference instead (shaded periods). For technical reasons DSCD for Bremen are given between 89° and 80°.

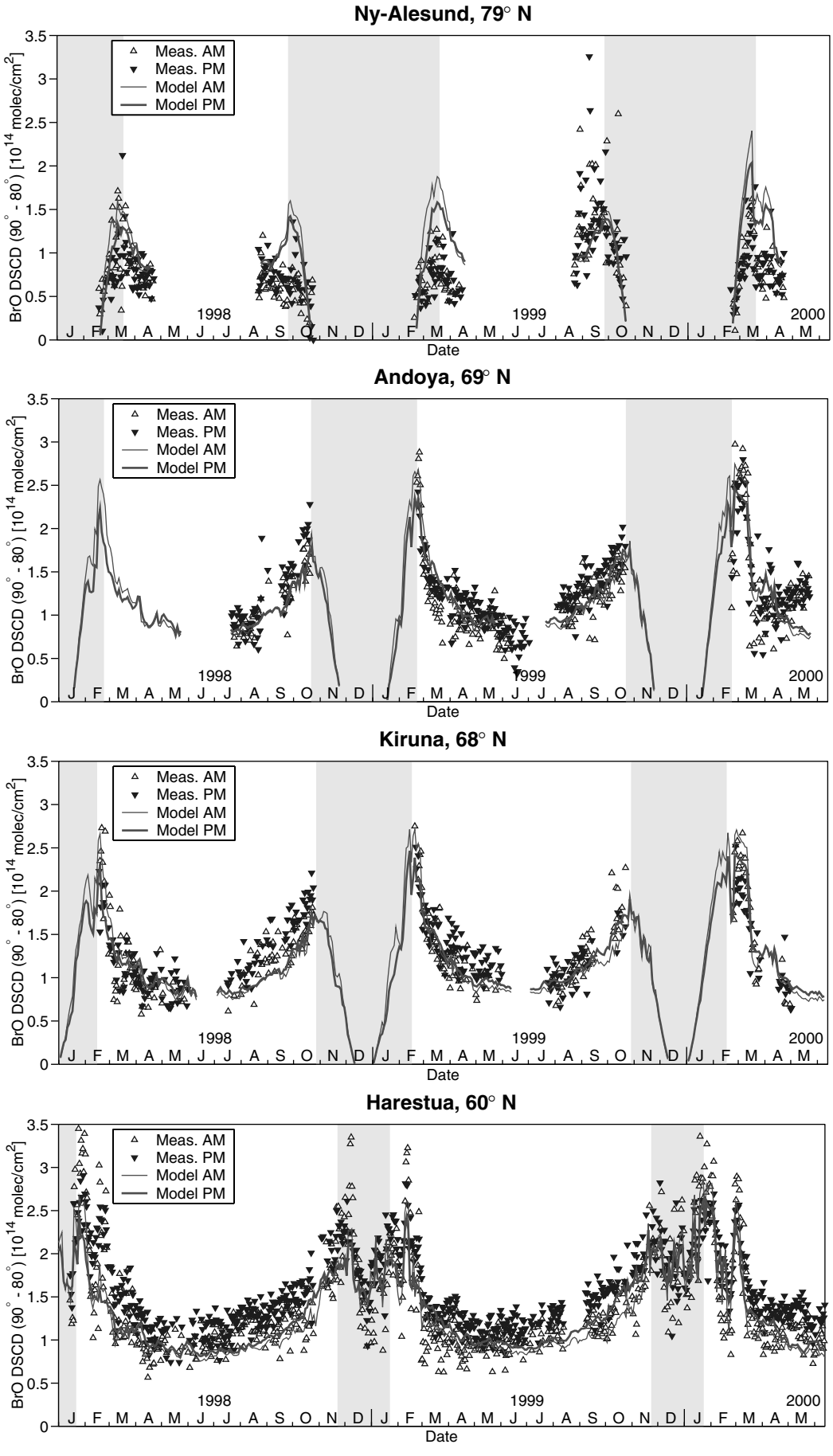
Ny-Alesund, 79° N
Andoya, 69° N
Kiruna, 68° N
Harestua, 60° N
Meas. AM
Meas. PM
Model AM
Model PM
BrO DSCD (90° - 80°) [10^14 molec/cm^2]
1998
1999
2000
J F M A M J J A S O N D J F M A M J J A S O N D J F M A M
Date

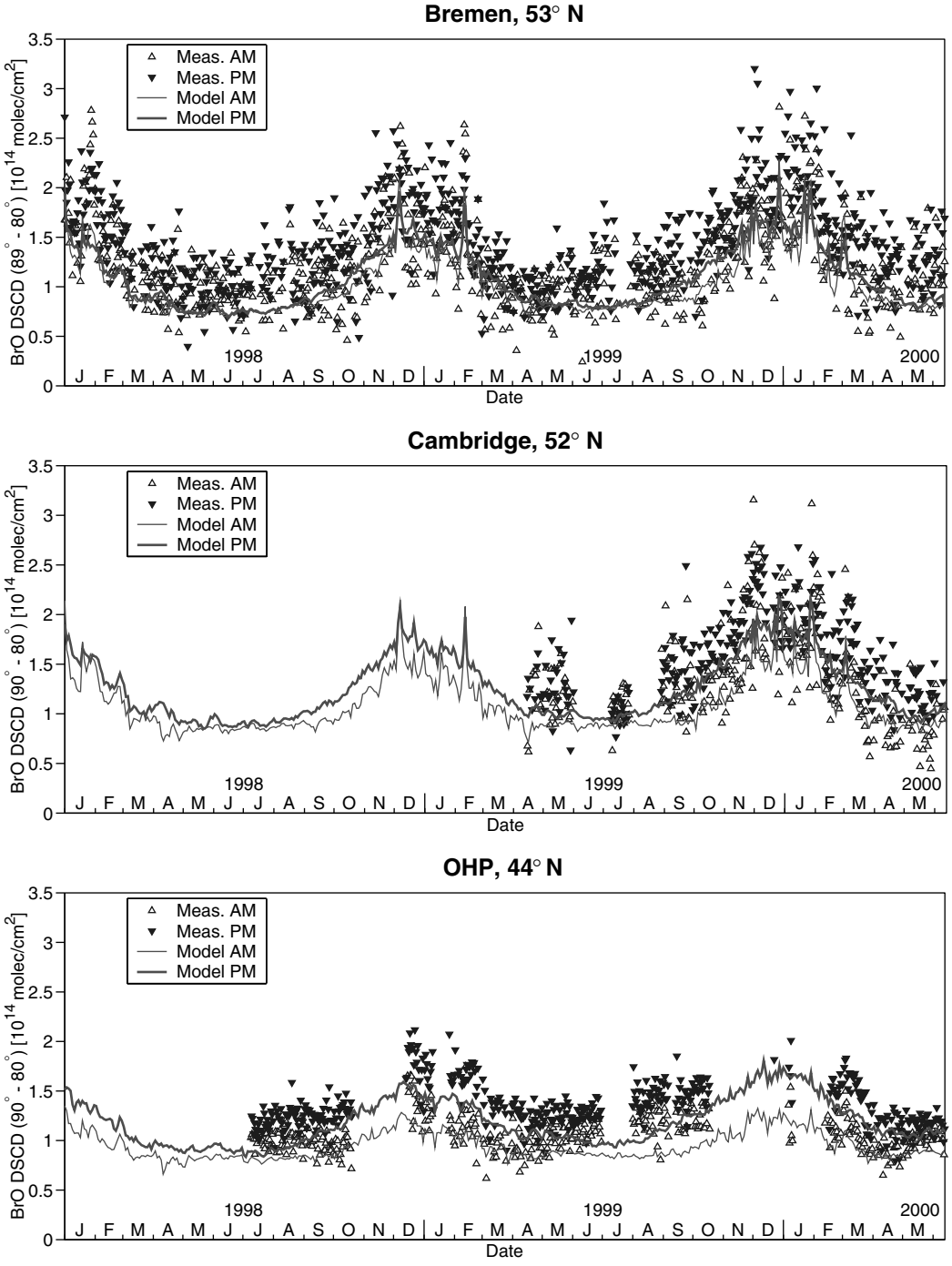

Figure 5. (continued)

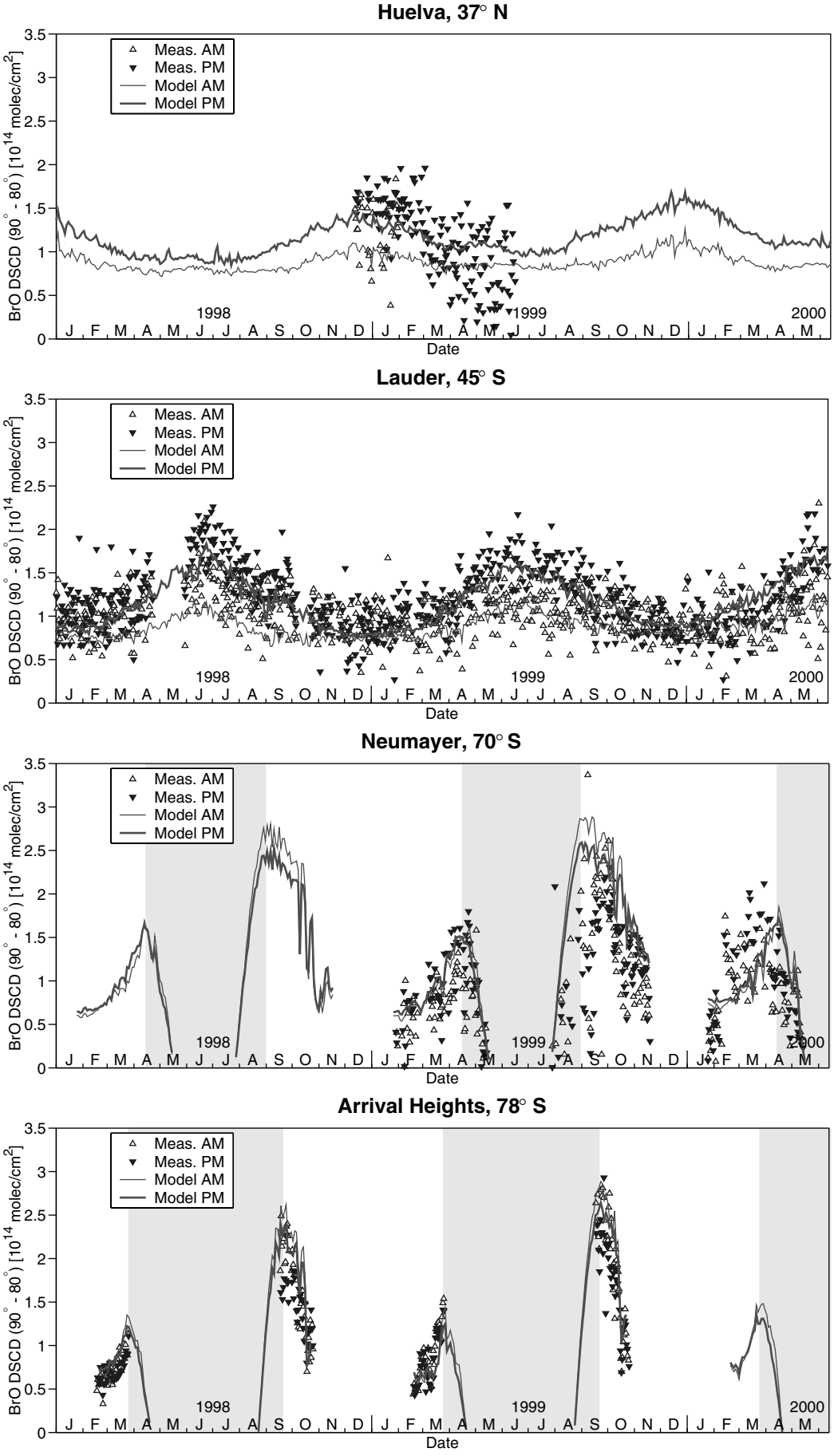

Figure 5. (continued)

Table 2. Mean Difference Between Observed and Modeled BrO DSCD at Different Stations

	Mean Difference (Measured − Modeled), in 10^{13} molecules/cm^2	
	AM	PM
Ny-Ålesund	−3.3 ± 4.6	−2.2 ± 4.2
Andøya	−0.1 ± 2.9	0.9 ± 2.4
Kiruna	0.4 ± 2.4	0.6 ± 2.4
Harestua	1.0 ± 2.7	2.3 ± 2.1
Bremen	1.9 ± 2.7	3.2 ± 3.0
Cambridge	2.2 ± 3.3	2.4 ± 2.5
OHP	1.7 ± 1.4	2.2 ± 1.6
Huelva[a]	2.8 ± 3.0	2.2 ± 2.2
Lauder	1.7 ± 2.3	0.7 ± 2.4
Neumayer	−3.8 ± 5.1	−2.9 ± 5.3
	Arrival Heights[b]	
Spring	−3.6 ± 2.6	−4.2 ± 2.6
Rest of year	−0.1 ± 2.1	−0.2 ± 2.1

The uncertainties given are the standard deviations of the differences (1σ).

[a] For Huelva, only December 1998 and January 1999 were considered when both AM and PM observations were available.

[b] For Arrival Heights, "spring" (defined here as September 17 to October 17) and the rest of the year were considered separately. The differences for the whole period are (−1.5 ± 2.8) × 10^{13} molecules/cm^2 for AM and (−1.8 ± 3.0) × 10^{13} molecules/cm^2 for PM.

a tropospheric BrO contribution can have a significant impact on the absolute slant columns but appear to be only second order effects for the differential slant columns. The situation is a somewhat different for aerosol scattering, however, although we found that the impact of stratospheric background aerosol is likely to be small. It is interesting to note that basically all of the effects considered here lead to a decrease of the 90−80° BrO DSCD, compared to our standard calculations used in the comparisons in the previous section.

6.4. Uncertainties of Reaction Rates

[42] The BrO concentrations are, to a large extent, controlled by the NO_2 concentration through reaction (1). Reducing the reaction rate constant to the JPL 2000 lower limit increases the BrO DSCD at sunrise by about 5% and the BrO DSCD at sunset by about 17% for typical mid-latitude conditions. Consequently, this increases the difference of the PM-AM BrO DSCD by more than 50%. (Note that the recommendation for the rate constant of reaction (1) did not change between JPL 1997 and JPL 2000, but the estimated uncertainty was decreased.)

[43] The new JPL 2000 reaction rate recommendations [*Sander et al.*, 2000] give a faster rate constant for the reaction BrO + ClO → BrCl + O_2, resulting in an increase in BrCl and a decrease in BrO for situations of activated chlorine. However, the difference between the JPL 1997 and the JPL 2000 reaction rate constants is still well within the estimated uncertainty of the reaction rate constant [*Sander et al.*, 2000]. Increasing the rate constant to the JPL 2000 upper limit decreases the calculated BrO DSCD by about 15% for situations where BrCl is the major bromine reservoir.

[44] Table 4 summarizes the calculated impact of the uncertainties of reaction rate constants on the BrO DSCD for the most important reactions. These are the formation and the (photolytic) loss reactions for the reservoir species $BrONO_2$, HOBr and, under situations of high chlorine activation, BrCl. For the gas phase reactions (i.e., BrO + NO_2, BrO + HO_2, and BrO + ClO) the estimated uncertainties given by the JPL 2000 recommendations have been used. The photolytic loss reactions have been changed rather arbitrarily to match the uncertainty of the corresponding gas phase production rates for comparison. They do not necessarily reflect the estimated uncertainties for these reactions. As can be seen, changing the gas phase production rates or changing the photolytic loss rates leads to a different impact on the BrO DSCD, since the bromine partitioning is not in photochemical steady state at sunrise and sunset.

[45] As a rough estimate for the combined uncertainty of the γ value for reaction (4) and of the modeled background aerosol surface area, we have performed a sensitivity calculation where the bromine nitrate hydrolysis has been reduced by 50%.

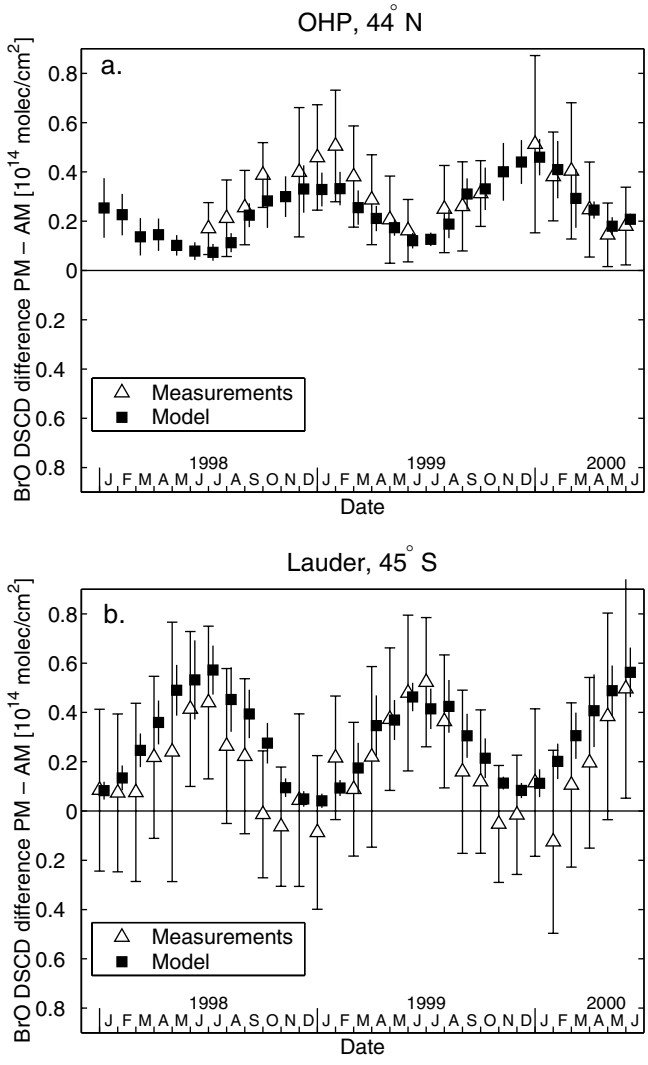

Figure 6. Comparison of the measured and modeled difference between the evening and morning BrO DSCD for Observatoire de Haute-Provence (OHP, 44°N) and Lauder (45°S). The error bars represent monthly averages and their standard deviation (1σ).

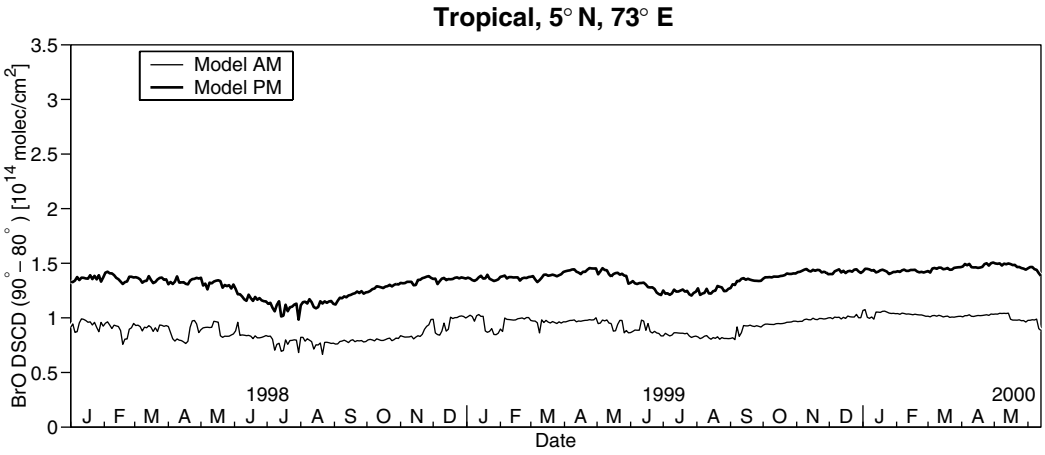

Figure 7. Modeled BrO DSCD for a tropical site (Kaashidhoo, Maldives, 5°N).

[46] Recently *Soller et al.* [2001] found that the reaction of $BrONO_2$ with $O(^3P)$ could be an important loss for bromine nitrate, increasing daytime BrO concentrations. The impact of this reaction on BrO is relatively small in the lower stratosphere, due to the low concentrations of $O(^3P)$, but increases rapidly above about 20 km altitude. We have performed a number of sensitivity calculations were we assume that the products of the reaction $BrONO_2$ + $O(^3P)$ are BrO and NO_3. Including this reaction in the model increases BrO DSCD for typical midlatitude conditions by about 2×10^{13} molecules/cm^2, with larger increases at sunrise than at sunset. Table 4 shows the result for Bremen during March, which is typical for midlatitude situations, with an increase of 21% at sunrise and 13% at sunset. This will lead to a decrease of the PM-AM difference by -0.5×10^{13} molecules/cm^2, corresponding to a decrease of 17%. At high latitudes during periods of enhanced chlorine activation, however, this reactions has only a minor impact on the BrO DSCD (Table 4).

7. Discussion

[47] As shown in section 5, the model calculation reproduces the observed BrO differential slant columns generally very well. The seasonal and latitudinal variations, as well as the diurnal variations are well captured by the model. For most of the measurement sites observed BrO DSCD are on average 10% higher than the model which assumes a total bromine loading of 20 ppt. This discrepancy could largely be reduced by including the reaction $BrONO_2 + O(^3P) \rightarrow BrO + NO_3$ [*Soller et al.*, 2001]. Taking into account the estimated accuracy of the measurements of about 20% as well as the uncertainties in the model (estimated by the sensitivity studies), the observed BrO DSCD are consistent

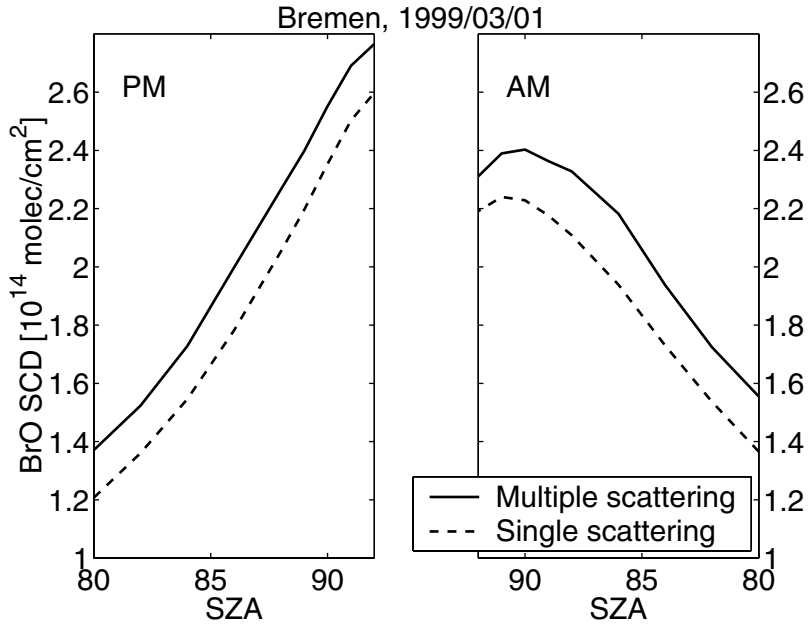

Figure 8. The impact of multiple scattering on the calculated BrO slant column.

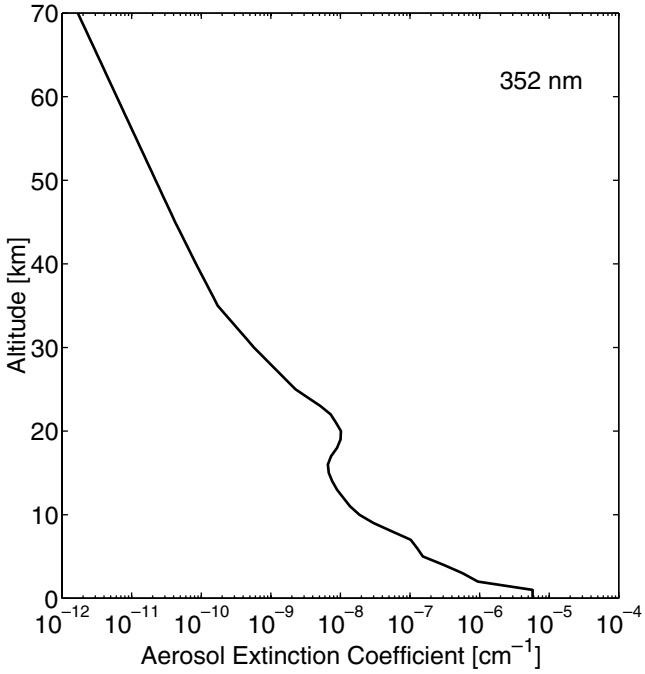

Figure 9. The aerosol extinction profile assumed for the calculation of the impact of aerosol scattering on BrO slant columns.

with a stratospheric bromine loading of about 20 ± 4 ppt. This agrees well with the estimated inorganic bromine loading of 21.5 ± 3.0 ppt, as derived for air of 5.6 years mean age for winter 1998/1999 by *Pfeilsticker et al.* [2000].

[48] The good agreement between the observed and modeled AM/PM variation provides strong evidence that the model correctly reproduces the BrO-related bromine chemistry. The sensitivity studies show that uncertainties in the production rate of $BrONO_2$—either due to uncertainties in the rate constant or due to uncertainties of the NO_2 concentration—will have a large impact on the PM-AM difference of the BrO DSCD. Any changes in the modeled NO_2 concentration alone would thus lead to a discrepancy between observed and modeled PM-AM difference. The situation is different, however, if one takes into account the coupling between individual effects. One of the largest uncertainties for the modeled NO_2 concentrations is the aerosol loading in the model. In fact, there is evidence that for the period considered here the model overestimates the aerosol surface area and thus underestimates the NO_x/NO_y ratio in the lower stratosphere. Reducing the aerosol loading will increase the NO_x/NO_y ratio and will thus decrease BrO by increasing $BrONO_2$. However, the NO_x increase will lead to a HO_x decrease and—even more important here—the decrease of the aerosol loading will reduce the heterogeneous conversion of $BrONO_2$ into HOBr. As a result of these combined effects we find that reducing the aerosol loading in the model reduces the BrO DSCD, but leaves the PM-AM difference largely unchanged.

[49] Including the reaction $BrONO_2 + O(^3P)$ [*Soller et al.*, 2001] decreases the PM-AM difference at midlatitudes by about 0.5 to 1.0 × 10^{13} molecules/cm^2. This will lead to a better agreement with the Lauder measurements and a slightly worse agreement with the OHP measurements. The main features of the PM-AM differences, however, are not affected by this reaction.

[50] Neglecting the heterogeneous conversion of $BrONO_2$ to HOBr reduces AM BrO DSCD by about 2 × 10^{13} molecules/cm^2 for typical midlatitude situations, while the PM DSCD are practically unchanged (see also Table 4). The inclusion of the heterogeneous conversion of $BrONO_2$ to HOBr in the model thus clearly results in a better agreement of the modeled BrO AM/PM ratio with obser-

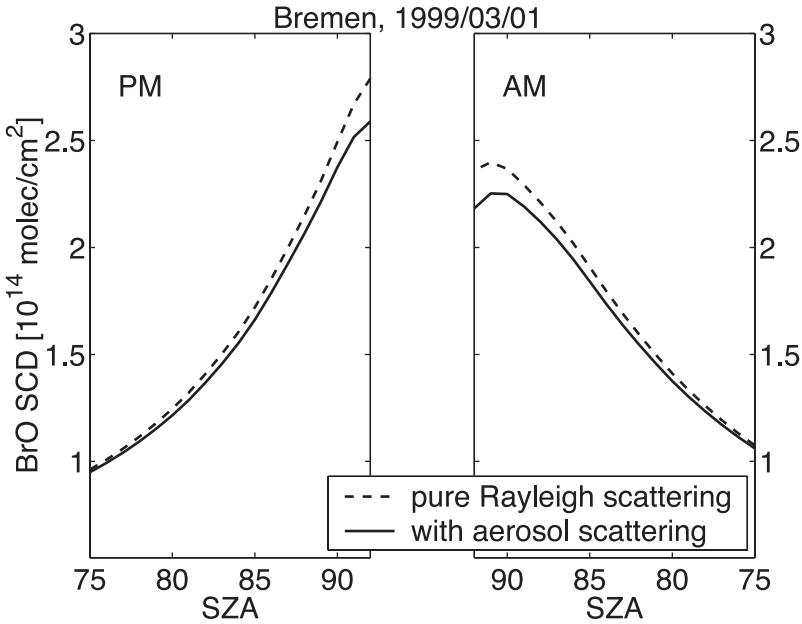

Figure 10. The impact of aerosol scattering on the calculated BrO slant column, based on the assumed aerosol profile shown in Figure 9.

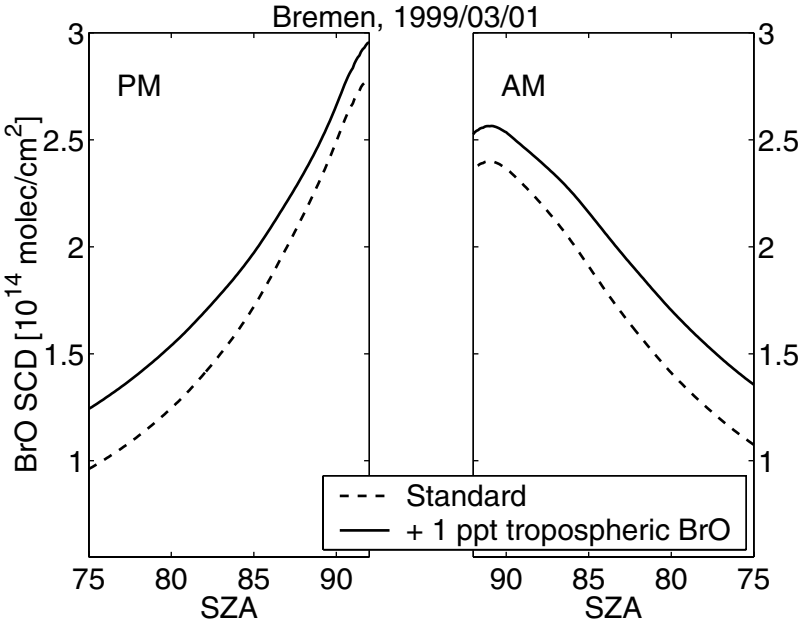

Figure 11. The impact of an assumed tropospheric BrO background on the calculated BrO slant column. The calculations assumed an additional uniform BrO contribution of 1 ppt between the ground and the lowest model level at 330 K.

vations. So although the BrO observations presented here do not prove that HOBr is the major bromine reservoir before sunrise, the good agreement between model and observations for the AM/PM ratio provides strong evidence that HOBr is indeed the major bromine reservoir before sunrise. In addition the rapid increase of HO_x at sunrise, observed during the SPADE campaign [*Salawitch et al.*, 1994] is consistent with the heterogeneous conversion of $BrONO_2$ to HOBr [see also *Lary et al.*, 1996]. It thus seems very unlikely that OBrO is a significant nighttime bromine reservoir, as suggested by *Renard et al.* [1998].

[51] The discrepancy between observed and modeled BrO DSCD at high latitude spring for situations of high chlorine activation can be explained most easily by the given uncertainty of the reaction BrO + ClO → BrCl + O_2 or the photolysis of BrCl. Increasing the rate constant for the reaction BrO +ClO → BrCl + O_2 to the upper limit of the JPL 2000 recommendation brings the model in good agreement with the observations during periods of high chlorine activation. For all other situations, and especially high latitude fall, the BrO DSCD remain unaffected by changing this rate constant. As the production of BrCl is the rate limiting step for one channel of the BrO/ClO ozone loss cycle, increasing the rate constant would have an impact on the calculated ozone loss, both at high and midlatitudes. This would be even more important if also the other

Table 3. Impact of Different Processes on the Calculated BrO 90–80° Differential Slant Column Densities[a]

	Change of BrO DSCD, %		
	AM	PM	PM–AM
"Multiple scattering"	−2	+3	+18
"Aerosol"	−9	−7	−2
"tropospheric BrO"	−13	−10	0

"Multiple scattering" is the change between a calculation with multiple scattering and a calculation with single scattering. "Aerosol" is the change between a calculation with additional aerosol scattering and a calculation with Rayleigh scattering only. "Tropospheric BrO" is the change for a calculation with an additional 1 ppt BrO in the troposphere.

[a] Calculations have been performed for Bremen, 1 March 1999.

Table 4. Impact of Reaction Rate Uncertainties on the Calculated BrO 90–80° Differential Slant Column Densities[a]

Reaction	Change of Rate Constant, %	Change of BrO DSCD, %		
		AM	PM	PM–AM
Midlatitude				
BrO + NO_2 + M → $BrONO_2$ + M	−25[b]	+5	+17	+54
$BrONO_2$ + hν → Br + NO_3	+25[c]	+7	+9	+13
BrO + HO_2 → HOBr + O_2	−50[b]	+4	+2	−5
HOBr + hν → Br + OH	+100[c]	+23	+2	−70
$BrONO_2$ + H_2O(aq) → HOBr + HNO_3	−50[d]	−8	−0.5	+26
$BrONO_2$ + $O(^3P)$ → products	included[f]	+21	+13	−17
Polar				
BrO + ClO → BrCl + O_2	+115[e]	−12	−18	+61
BrCl + hν → Br + Cl	−50[c]	−12	−15	+25
$BrONO_2$ + $O(^3P)$ → products	included[f]	+3	+3	+2

[a] Calculations have been performed for Bremen, 1 March 1999 (midlatitude case, in which very similar results are obtained for different scenarios), and Harestua, 29 January 2000 (polar case).

[b] The change in rate constant refers to a stratospheric temperature of 210 K in the midlatitude case and 193 K in the polar case. They correspond to the estimated uncertainty of the rate constants given by the JPL 2000 recommendations [*Sander et al.*, 2000].

[c] Photolysis rates have been scaled to match the change in the corresponding gas phase reactions for comparison. They do not necessarily reflect estimated uncertainties for these reactions.

[d] The 50% reduction corresponds roughly to the estimated uncertainty in the modeled background aerosol surface area.

[e] The 115% increase corresponds to the difference between the upper limit of the JPL 2000 recommendations and the value of the JPL 1997 recommendations, used for the calculations in Figure 5. The estimated uncertainty for the reaction rate is about ±65% at 193K [*Sander et al.*, 2000].

[f] Reaction rate according to *Soller et al.* [2001]. Here, we assume that the products are BrO + NO_3.

channels of the BrO + ClO reaction were to be increased, as might be suggested by the fact that laboratory measurements showed a fairly constant branching ratio of about 8% for the BrCl producing channel over a wide range of temperatures [*Atkinson et al.*, 2000, and references therein].

[52] However, there may also be other reasons for the discrepancy between measured and modeled BrO DSCD during late winter and spring at high latitudes, such as events of enhanced tropospheric BrO. Such events can clearly be identified for individual days in the BrO measurements at all polar sites (Ny-Ålesund, Neumayer, and Arrival Heights). Therefore, we may speculate that, in addition, less clearly identifiable events of enhanced tropospheric BrO may lead to a general decrease of the observed BrO DSCD at polar sites during spring.

[53] Recently, *Avallone and Toohey* [2001] suggested that the adduct BrOOCl may form a significant bromine reservoir under cold conditions with high chlorine activation. While this could possibly explain our observed BrO discrepancy qualitatively, a quantitative analysis has to await further studies of the reaction kinetics of the BrOOCl adduct.

8. Conclusions

[54] We have presented ground-based UV–visible measurements of BrO slant column densities from a near-global network. These measurements allow us to draw a picture of the global distribution of stratospheric BrO, especially its seasonal and latitudinal variations. Comparison with calculated BrO slant columns from the SLIMCAT three-dimensional chemical transport model generally show a very good agreement. Moreover, the observational data set itself shows a remarkable internal consistency. In fact, the comparison with the model can help to assess the internal consistency of the BrO time series at one station and the consistency between the BrO measurements at different stations. This study shows that the analysis of the ground-based UV–visible BrO measurements has reached a level where the overall accuracy is to a large extent limited by uncertainties in the BrO absorption cross-section.

[55] The model reproduces the seasonal and latitudinal variations of the BrO DSCD well, indicating that our understanding of the basic features controlling stratospheric BrO is correct. A discrepancy between observed and modeled BrO DSCD of about 10% on average could largely be resolved by including the reaction $BrONO_2 + O(^3P)$ [*Soller et al.*, 2001]. Taking this into account, the observations are consistent with a current stratospheric bromine loading of about 20 ± 4 ppt, in excellent agreement with previous estimates.

[56] In particular the comparison between observed and modeled AM/PM variation of BrO is a critical test for our understanding of stratospheric bromine chemistry. The good agreement provides strong evidence that the model correctly reproduces stratospheric bromine chemistry.

[57] For high latitude spring under situations of chlorine activation, the model overestimates the BrO differential slant column densities. We showed that this discrepancy is within the estimated uncertainty of the rate constant for the reaction $BrO + ClO \rightarrow BrCl + O_2$. Increasing the rate constant to the JPL 2000 upper limit brings the model in good agreement with the observations. As this would have implications for the calculated ozone loss, it deserves further attention. However, other processes, such as possible tropospheric BrO contributions could in principle also lead to a reduction of the BrO DSCD at high latitudes in spring, and cannot be ruled out at this stage.

[58] The good agreement between the model and the observations gives us confidence that we have correctly identified the relevant mechanisms controlling the global distribution of stratospheric BrO and we can use the model to estimate the impact of bromine on stratospheric ozone depletion.

[59] **Acknowledgments.** Parts of this work were funded by the UK Natural Environment Research Council's UTLS program and by the European Commission's Environment Research Programmes via ENV4-CT97-0521 (BrO Project). Work at BIRA has been funded through the ESAC project from the Belgian SSTC, contract no. CG/DD/01A and the "Fonds National de la Recherche Scientifique (FNRS)." Work at the IUP/IFE University of Bremen has been supported in part by the Land of Bremen, the German Ministry for Research and Education, and the German Space Agency. Meteorological data were provided by the United Kingdom Met Office via the British Atmospheric Data Centre.

References

Aliwell, S. R., R. L. Jones, and D. J. Fish, Mid-latitude observations of the seasonal variation of BrO, 1, Zenith-sky measurements, *Geophys. Res. Lett.*, *24*, 1195–1198, 1997.

Aliwell, S. R., et al., Analysis for BrO in zenith-sky spectra: An intercomparison exercise for analysis improvement, *J. Geophys. Res.*, *107*, 10.1029/2001JD000329, 2002.

Arpag, K. H., P. V. Johnston, H. L. Miller, R. W. Sander, and S. Solomon, Observations of stratospheric BrO column over Colorado, 40°N, *J. Geophys. Res.*, *99*, 8175–8181, 1994.

Atkinson, R., D. L. Baulch, R. A. Cox, R. F. Hampson Jr., J. A. Kerr, M. J. Rossi, and J. Troe, Evaluated kinetic and photochemical data for atmospheric chemistry, Supplement VIII, Halogen species, IUPAC subcomittee on gas kinetic data evaluation for atmospheric chemistry, *J. Phys. Chem. Ref. Data*, *29*, 167–266, 2000.

Avallone, L. M., and D. W. Toohey, Tests of halogen photochemistry using in situ measurements of ClO and BrO in the lower stratosphere, *J. Geophys. Res.*, *106*, 10,411–10,421, 2001.

Avallone, L. M., D. W. Toohey, S. M. Schauffler, W. H. Pollock, L. E. Heidt, E. L. Atlas, and K. R. Chan, In situ measurements of BrO during AASE II, *Geophys. Res. Lett.*, *22*, 831–834, 1995.

Bates, D. R., Rayleigh scattering by air, *Planet. Space Sci.*, *32*, 785–790, 1984.

Bekki, S., and J. A. Pyle, A two-dimensional modeling study of the volcanic eruption of Mount Pinatubo, *J. Geophys. Res.*, *99*, 18,861–18,869, 1994.

Brown, S., R. Talukdar, and A. Ravishankara, Rate constants for the reaction $OH + NO_2 + M \rightarrow HNO_3 + M$ under atmospheric conditions, *Chem. Phys. Lett.*, *299*, 277–284, 1999a.

Brown, S., R. Talukdar, and A. Ravishankara, Reconsideration of the rate constant for the reaction of hydroxyl radicals with nitric acid, *J. Phys. Chem. A*, *103*, 3031–3037, 1999b.

Brune, W. H., D. W. Toohey, J. G. Anderson, W. L. Starr, J. F. Vedder, and E. F. Danielsen, In situ northern mid-latitude observations of ClO, O_3, and BrO in the wintertime lower stratosphere, *Science*, *242*, 558–562, 1988.

Brune, W. H., J. G. Anderson, and K. R. Chan, In situ observations of BrO over Antarctica: ER-2 aircraft results from 54°S to 72°S latitude, *J. Geophys. Res.*, *94*, 16,639–16,647, 1989.

Carroll, M. A., R. W. Sanders, S. Solomon, and A. L. Schmeltekopf, Visible and near-ultraviolet spectroscopy at McMurdo station, Antarctica, 6, Observations of BrO, *J. Geophys. Res.*, *94*, 16,633–16,638, 1989.

Chipperfield, M., Multiannual simulations with a three-dimensional chemical transport model, *J. Geophys. Res.*, *104*, 1781–1805, 1999.

Chipperfield, M. P., and J. A. Pyle, Model sensitivity studies of Arctic ozone depletion, *J. Geophys. Res.*, *103*, 28,389–28,403, 1998.

Chipperfield, M. P., D. E. Shallcross, and D. J. Lary, A model study of the potential role of the reaction BrO + OH in the production of stratospheric HBr, *Geophys. Res. Lett.*, *24*, 3025–3028, 1997.

Chipperfield, M. P., T. Glassup, I. Pundt, and O. V. Rattigan, Model calculations of stratospheric OBrO indicating very small abundances, *Geophys. Res. Lett.*, *25*, 3575–3578, 1998.

Daniel, J. S., S. Solomon, R. W. Portmann, and R. R. Garcia, Stratospheric ozone destruction: The importance of bromine relative to chlorine, *J. Geophys. Res.*, *104*, 23,871–23,880, 1999.

DeMore, W. B., S. P. Sander, D. M. Golden, R. F. Hampson, M. J. Kurylo, C. J. Howard, A. R. Ravishankara, C. E. Kolb, and M. J. Molina, Chemical Kinetics and Photochemical Data for Use in Stratospheric Modeling, *JPL Publ. 97-4*, NASA Jet Propul. Lab., 1997.

Dvortsov, V. L., M. A. Geller, S. Solomon, S. M. Schauffler, E. L. Atlas, and D. R. Blake, Rethinking reactive halogen budgets in the midlatitude lower stratosphere, *Geophys. Res. Lett.*, *26*, 1699–1702, 1999.

Eisinger, M., A. Richter, A. Ladstätter-Weißenmayer, and J. P. Burrows, DOAS zenith sky observations, 1, BrO measurements over Bremen (53°N) 1993–1994, *J. Atmos. Chem.*, *26*, 93–108, 1997.

Erle, F., A. Grendel, D. Perner, U. Platt, and K. Pfeilsticker, Evidence of heterogeneous bromine chemistry on cold stratospheric sulphate aerosols, *Geophys. Res. Lett.*, *25*, 4329–4332, 1998.

Erle, F., U. Platt, and K. Pfeilsticker, Measurement of OBrO upper limits in the nighttime stratosphere, *Geophys. Res. Lett.*, *27*, 2217–2220, 2000.

Fish, D. J., R. L. Jones, and E. K. Strong, Midlatitude observations of the diurnal variation of stratospheric BrO, *J. Geophys. Res.*, *100*, 18,863–18,871, 1995.

Fish, D. J., S. R. Aliwell, and R. L. Jones, Mid-latitude observations of the seasonal variation of BrO, 2, Interpretation and modelling study, *Geophys. Res. Lett.*, *24*, 1199–1202, 1997.

Fitzenberger, R., H. Bösch, C. Camy-Peyret, M. P. Chipperfield, H. Harder, U. Platt, B.-M. Sinnhuber, T. Wagner, and K. Pfeilsticker, First profile measurements of tropospheric BrO, *Geophys. Res. Lett.*, *27*, 2921–2924, 2000.

Fraser, P. J., D. E. Oram, C. E. Reeves, S. A. Penkett, and A. McCulloch, Southern hemispheric halon trends (1989–1998) and global halon emissions, *J. Geophys. Res.*, *104*, 15,985–15,999, 1999.

Frieß, U., M. Chipperfield, H. Harder, C. Otten, U. Platt, J. Pyle, T. Wagner, and K. Pfeilsticker, Intercomparison of measured and modeled BrO slant column amounts for the Arctic winter and spring 1994–1995, *Geophys. Res. Lett.*, *26*, 1861–1864, 1999.

Frieß, U., T. Wagner, and U. Platt, Measurement and analysis of tropospheric BrO-events in the Antarctic marine boundary layer, in *Proceedings of the EGS XXVI General Assembly, Nice, France*, p. 1017, 2001.

Hanson, D. R., and A. R. Ravishankara, Heterogeneous chemistry of bromine species in sulfuric acid under stratospheric conditions, *Geophys. Res. Lett.*, *22*, 385–388, 1995.

Hanson, D. R., A. R. Ravishankara, and E. R. Lovejoy, Reaction of $BrONO_2$ with H_2O on submicron sulfuric acid aerosol and the implications for the lower stratosphere, *J. Geophys. Res.*, *101*, 9063–9069, 1996.

Harder, H., et al., Stratospheric BrO profiles measured at different latitudes and seasons: Atmospheric observations, *Geophys. Res. Lett.*, *25*, 3843–3846, 1998.

Harder, H., H. Bösch, C. Camy-Peyret, M. P. Chipperfield, R. Fitzenberger, S. Payan, D. Perner, U. Platt, B.-M. Sinnhuber, and K. Pfeilsticker, Comparison of measured and modeled stratospheric BrO: Implications for the total amount of stratospheric bromine, *Geophys. Res. Lett.*, *27*, 3695–3698, 2000.

Harwood, M. H., J. B. Burkholder, and A. R. Ravishankara, Photodissociation of $BrONO_2$ and N_2O_5: Quantum yields for NO_3 production at 248, 308, and 352.5 nm, *J. Phys. Chem.*, *102*, 1309–1317, 1998.

Hendrick, F., et al., Simulation of BrO diurnal variation and BrO slant columns: Intercomparison exercise between three model packages, in *Proceedings of the Fifth European Symposium on Stratospheric Ozone*, Eur. Comm. Air Pollut. Res. Rep. 73, pp. 256–259, 1999.

Ingham, T., D. Bauer, J. Landgraf, and J. N. Crowley, Ultraviolet–visible absorption cross sections of gaseous HOBr, *J. Phys. Chem. A*, *102*, 3293–3298, 1998.

Johnson, D. G., W. A. Traub, K. V. Chance, and K. W. Jucks, Detection of HBr and upper limit for HOBr: Bromine partitioning in the stratosphere, *Geophys. Res. Lett.*, *22*, 1373–1376, 1995.

Ko, M. K. W., N.-D. Sze, C. J. Scott, and D. K. Weisenstein, On the relation between stratospheric chlorine/bromine loading and short-lived tropospheric source gases, *J. Geophys. Res.*, *102*, 25,507–25,517, 1997.

Kreher, K., P. V. Johnston, S. W. Wood, B. Nardi, and U. Platt, Ground-based measurements of tropospheric and stratospheric BrO at Arrival Heights, Antarctica, *Geophys. Res. Lett.*, *24*, 3021–3024, 1997.

Lary, D. J., Gas phase atmospheric bromine photochemistry, *J. Geophys. Res.*, *101*, 1505–1516, 1996.

Lary, D. J., M. P. Chipperfield, R. Toumi, and T. Lenton, Heterogeneous atmospheric bromine chemistry, *J. Geophys. Res.*, *101*, 1489–1504, 1996.

Liou, K. N., *Radiation and Cloud Processes in the Atmosphere*, 487 pp., Oxford Univ. Press, New York, 1992.

McKinney, K. A., J. M. Pierson, and D. W. Toohey, A wintertime in situ profile of BrO between 17 and 27 km in the Arctic vortex, *Geophys. Res. Lett.*, *24*, 853–856, 1997.

Müller, R. W., H. Bovensmann, J. W. Kaiser, A. Richter, A. Rozanov, F. Wittrock, and J. P. Burrows, Consistent interpretation of ground based and GOME BrO slant column data, *Adv. Space Res.*, *29*, 1655–1660, 2002.

Otten, C., F. Ferlemann, U. Platt, T. Wagner, and K. Pfeilsticker, Ground-based DOAS UV/visible measurements at Kiruna (Sweden) during SESAME winters 1993/94 and 1994/95, *J. Atmos. Chem.*, *30*, 141–162, 1998.

Pfeilsticker, K., W. T. Sturges, H. Bösch, C. Camy-Peyret, M. P. Chipperfield, A. Engel, R. Fitzenberger, M. Müller, S. Payan, and B.-M. Sinnhuber, Lower stratospheric organic and inorganic bromine budget for the Arctic winter 1998/99, *Geophys. Res. Lett.*, *27*, 3305–3308, 2000.

Platt, U., Differential optical absorption spectroscopy (DOAS), in *Air Monitoring by Spectroscopic Techniques*, Chem. Anal. Ser., vol. 127, edited by M. W. Sigrist, pp. 27–84, John Wiley, New York, 1994.

Pundt, I., et al., Simultaneous UV–vis measurements of BrO from balloon, satellite and ground: Implications for tropospheric BrO, in *Proceedings of the Fifth European Symposium on Stratospheric Ozone*, Eur. Comm. Air Pollut. Res. Rep. 73, pp. 316–319, 1999a.

Pundt, I., J. P. Pommereau, F. Goutail, M. P. Chipperfield, F. Danis, N. R. P. Harris, and J. A. Pyle, Vertical distribution of BrO and Bry at high, mid-, and low latitudes, in *Proceedings of the Fifth European Symposium on Stratospheric Ozone*, Eur. Comm. Air Pollut. Res. Rep. 73, pp. 312–315, 1999b.

Renard, J. B., M. Pirre, C. Robert, and D. Huguenin, The possible detection of OBrO in the stratosphere, *J. Geophys. Res.*, *103*, 25,383–25,395, 1998.

Richter, A., F. Wittrock, M. Eisinger, and J. P. Burrows, GOME observations of tropospheric BrO in northern hemispheric spring and summer 1997, *Geophys. Res. Lett.*, *25*, 2683–2686, 1998.

Richter, A., M. Eisinger, A. Ladstätter-Weißenmayer, and J. P. Burrows, DOAS zenith sky observations, 2, Seasonal variation of BrO over Bremen (53°) 1994–1995, *J. Atmos. Chem.*, *32*, 83–99, 1999.

Rozanov, A., V. Rozanov, and J. P. Burrows, A numerical radiative transfer model for a spherical planetary atmosphere: Combined differential–integral approach involving the Picard iterative approximation, *J. Quant. Spectrosc. Radiat. Transfer*, *69*, 491–512, 2001.

Salawitch, R. J., et al., The diurnal variation of hydrogen, nitrogen, and chlorine radicals: Implications for the heterogeneous production of HNO_2, *Geophys. Res. Lett.*, *21*, 2551–2554, 1994.

Sander, S. P., et al., Chemical Kinetics and Photochemical Data for Use in Stratospheric Modeling, *JPL Publ. 00-3*, NASA Jet Propul. Lab., 2000.

Sarkissian, A., H. K. Roscoe, and D. J. Fish, Ozone measurements by zenith-sky spectrometers: An evaluation of errors in air-mass factors calculated by radiative transfer models, *J. Quant. Spectrosc. Radiat. Transfer*, *54*, 471–480, 1995.

Schauffler, S. M., E. L. Atlas, D. R. Blake, F. Flocke, R. A. Lueb, J. M. Lee-Taylor, V. Stroud, and W. Travnicek, Distributions of brominated organic compounds in the troposphere and lower stratosphere, *J. Geophys. Res.*, *104*, 21,513–21,535, 1999.

Slusser, J. R., D. J. Fish, E. K. Strong, R. L. Jones, H. K. Roscoe, and A. Sarkissian, Five years of NO_2 vertical column measurements at Faraday (65°S): Evidence for the hydrolysis of $BrONO_2$ on Pinatubo aerosols, *J. Geophys. Res.*, *102*, 12,987–12,993, 1997.

Soller, R., J. M. Nicovich, and P. H. Wine, Temperature-dependent rate coefficients for the reactions of $Br(^2P_{3/2})$, $Cl(^2P_{3/2})$, and $O(^3PJ)$ with $BrONO_2$, *J. Phys. Chem. A*, *105*, 1416–1422, 2001.

Solomon, S., A. L. Schmeltekopf, and R. W. Sanders, On the interpretation of zenith sky absorption-measurements, *J. Geophys. Res.*, *92*, 8311–8319, 1987.

South, A. M., N. Mohamed-Tahrin, R. A. Freshwater, and R. L. Jones, Ground-based observations of BrO over Huelva, Spain (37°N), in *Proceedings of the Fifth European Symposium on Stratospheric Ozone*, Eur. Comm. Air Pollut. Res. Rep. 73, pp. 356–359, 1999.

Sturges, W. T., D. E. Oram, L. J. Carpenter, S. A. Penkett, and A. Engel, Bromoform as a source of stratospheric bromine, *Geophys. Res. Lett.*, *27*, 2081–2084, 2000.

Sturges, W. T., H. P. McIntyre, S. A. Penkett, J. Chappellaz, M. J.-Barnola, R. Mulvaney, E. Atlas, and V. Stroud, Methyl bromide, other brominated methanes, and methyl iodide in polar firn air, *J. Geophys. Res.*, *106*, 1595–1606, 2001.

Swinbank, R., and A. O'Neill, A stratosphere–troposphere data assimilation system, *Mon. Weather Rev.*, *122*, 686–702, 1994.

Toohey, D. W., J. G. Anderson, W. H. Brune, and K. R. Chan, In situ measurements of BrO in the Arctic stratosphere, *Geophys. Res. Lett.*, *17*, 513–516, 1990.

Tørnkvist, K. K., D. W. Arlander, and B.-M. Sinnhuber, Ground-based UV measurements of BrO and OClO over Ny-Ålesund during Winter

1996 and 1997 and Andøya (1998/99), *J. Atmos. Chem.*, *43*, 75–106, 2002.

Van Roozendael, M., C. Fayt, F. Hendrick, C. Hermans, J.-C. Lambert, D. Forteyn, B.-M. Sinnhuber, and M. P. Chipperfield, Seasonal and diurnal variations of BrO column abundances above Harestua (60°N) and Haute-Provence (44°N) during THESEO, in *Proceedings of the Fifth European Symposium on Stratospheric Ozone*, Eur. Comm. Air Pollut. Res. Rep. 73, pp. 332–335, 1999a.

Van Roozendael, M., C. Fayt, J.-C. Lambert, I. Pundt, T. Wagner, A. Richter, and K. Chance, Development of a bromine oxide product from GOME, in *Proceedings of the European Symposium on Atmospheric Measurements from Space (ESAMS 99)*, 18–22 January, ESTEC, Noordwijk, Netherlands, WPP-161, pp. 543–547, Eur. Space Agency, Noordwijk, Netherlands, 1999b.

Wagner, T., and U. Platt, Satellite mapping of enhanced BrO concentrations in the troposphere, *Nature*, *395*, 486–490, 1998.

Wagner, T., C. Leue, M. Wenig, K. Pfeilsticker, and U. Platt, Spatial and temporal distribution of enhanced boundary layer BrO concentrations measured by the GOME instrument aboard ERS-2, *J. Geophys. Res.*, *106*, 24,225–24,236, 2001.

Wamsley, P. R., et al., Distribution of halon-1211 in the upper troposphere and lower stratosphere and the 1994 total bromine budget, *J. Geophys. Res.*, *103*, 1513–1526, 1998.

Wennberg, P. O., et al., Removal of stratospheric O_3 by radicals: In situ measurements of OH, HO_2, NO, NO_2, ClO, and BrO, *Science*, *266*, 398–404, 1994.

World Meteorological Organization (WMO), Scientific Assessment of Ozone Depletion: 1998, Global Ozone Research and Monitoring Project, Rep. No. 44, 1999.

D. W. Arlander and K. K. Tørnkvist, Norwegian Institute for Air Research, Kjeller, Norway.

H. Bovensmann, J. P. Burrows, R. Müller, A. Richter, B.-M. Sinnhuber, and F. Wittrock, Institute of Environmental Physics, University of Bremen, Germany. (bms@iup.physik.uni-bremen.de)

M. P. Chipperfield, School of the Environment, University of Leeds, Leeds, LS2 9JT, UK.

C.-F. Enell, Swedish Institute of Space Physics, Kiruna, Sweden.

U. Frieß, K. Pfeilsticker, U. Platt, and T. Wagner, Institute of Environmental Physics, University of Heidelberg, Germany.

F. Hendrick and M. Van Roozendael, Belgian Institute for Space Aeronomy, Brussels, Belgium.

P. V. Johnston and K. Kreher, National Institute of Water and Atmospheric Research, Lauder, New Zealand.

R. L. Jones, N. Mohamed-Tahrin, and A. M. South, Center for Atmospheric Science, University of Cambridge, UK.

J.-P. Pommereau and I. Pundt, Service d'Aéronomie, Verrières-le-Buisson, France.

Optical studies of polar stratospheric clouds and related phenomena — Errata

Carl-Fredrik Enell

Chapter 2

Page 4, section 2.1.2, "[Hesstvedt, 1962...]" Brackets misplaced. Should read "Hesstvedt [1962],/.../, and references in these".

Page 6, 2nd paragraph, Absolute vorticity: "rotation /.../ is conserved": should read "angular momentum /.../ is conserved".

Chapter 3

Page 12, 3rd paragraph: "The solution /../ according to Gustav Mie": Gustav Mie, *Beiträge zur Optik trüber Medien, speziell kolloidaler Metallösungen*, Annalen der Physik, Vierte Folge, Band 25, No.3, pp.377–445, 1908.

Chapter 5

Page 26, first paragraph: "the j:th trace species": Should read "the j:th trace species"; see the note on typography below.

Summary of included papers

Page 42, first paragraph: Last sentence should read "Cloud screening of tangent rays is suggested as one possible cause for this underestimation of PSC presence."

Errata of published first-author papers

Paper I

In table 3, p.1461, the word "parallel" signifies that the depolarisation of the light is weak. "Composition" refers to the most probable composition of the corresponding PSC types Ia, Ib and II.
Section 4, p.1461: "NAT profile": Should read "HNO_3 profile".

Paper II

Page 451, section 2, last paragraph: "Thus...", should read: "Thus, mesoscale processes have recently attracted much interest (see e.g. Carslaw and Amanatidis, 1999)...".
Page 454, footnote: the code "%7E" is equivalent to a tilde ("∼") sign; both can be used in URLs.
Page 457, references: Abbreviations of the names of some journals are used.

AGP	Annales Geophysicae
GP	Geofysiske Publikasjoner
GRL	Geophysical Research Letters
JGR	Journal of Geophysical Research

Meerktter, R.: should read Meerkötter, R.

Paper III

Table 1, p. 4: To conform with Figure 5, H_o should be replaced with H and H_{to} with H_{T}.

Note on typography

It is common practice to typeset symbols for physical quantities and indices in *italic* whereas abbreviations, acronyms, chemical formulae and subscripts should be set in roman style; e.g. T_{NAT}, j :th,Cl, H_2O. This standard is not followed consistently in the papers.

Swedish Institute of Space Physics
2002

IRF Scientific Report 278
ISBN 91-7305-307-4
ISSN 0284-1703